POLITECNICO DI MILANO
DEPARTMENT OF MECHANICAL ENGINEERING
DOCTORAL PROGRAM IN MECHANICAL ENGINEERING

INVESTIGATION OF MICRO SCALE BEHAVIOUR WITH CRYSTAL PLASTICITY: A STUDY OF HAYNES 230

Doctoral Dissertation of:
Pietro Giovanni Luccarelli

Supervisor:
Prof. Stefano Foletti

Tutor:
Prof. Carlo Mapelli

The Chair of the Doctoral Program:
Prof. Bianca Maria Colosimo

AY 2013-2016 – cycle XXIX

Abstract

In this Ph.D. thesis, the micro-structural behaviour of a Nickel-based alloy is discussed. The work aims to provide a description of the stress-strain field along grains and grain boundaries with finite element crystal plasticity simulations using an open source software, Warp3D. The results are then compared with those obtained with digital image correlation to evaluate the prediction of the numerical solutions. After a brief introduction to the work, a general overview of the literature on the two main topics of the thesis, analyses of micro-mechanical behaviour and crack closure measurements, is provided. Focusing on work that aims to describe the overall behaviour of the material and the local answer at the grain scale by means of crystal plasticity codes. Following, a study of the tensile mechanical behaviour is discussed. Both single crystals at room temperature and a polycrystalline structure at high temperature are taken into account. In this section the crystal plasticity model parameters are identified on single crystal tests and are then applied to the polycrystalline case. The following step of the work focused on room temperature cyclic behaviour aiming to describe a ratcheting test. The work then moved to the topic of fracture mechanics. The first step of this study is related to numerical simulations of fatigue crack growth in single crystal specimens, then the analyses moved on the emulation of crack's effects inside polycrystalline media. The discussion of those sections concerns the irreversibility generated during the propagation of the crack: the results are compared with experiments in terms of crack opening level and extension of the plastic zone at the crack tip.

Nomenclature

A, m - Paris law's coefficients

$\boldsymbol{C}$ - Elastic stiffness matrix

$\boldsymbol{C_0}$ - Elastic stiffness matrix in the reference frame

D_0, T_0 - Empirical parameters for temperature dependent shear modulus

$\boldsymbol{D}$ - Symmetric component of the velocity gradient

$\bar{\boldsymbol{D}}^{\boldsymbol{p}}$ - Plastic component of $\boldsymbol{D}$ in the intermediate configuration

E - Young's modulus

$\boldsymbol{F}$ - Deformation gradient

$\boldsymbol{F^e}$ - Elastic component of the deformation gradient

$\boldsymbol{F^p}$ - Plastic component of the deformation gradient

H_W - Work generated by the applied stress

I - Unit matrix

$K^{(s)}$ - Constant that characterize the material rate sensitivity on the s-th slip system

$\boldsymbol{L}$ - Velocity gradient

$\boldsymbol{L_p}$ - Plastic component of the velocity gradient

L_{notch} - Notch length

N - Number of cycles

$\boldsymbol{Q_G}$ - Rotation matrix for the grain

$\boldsymbol{R^e}$ - Elastic rotation

R_{notch} - Notch radius

S_i - Scale factor for the i-th component of the Mechanical Threshold Stress model

T - Temperature

U - Stress range reduction factor

$\boldsymbol{V^e}$ - Elastic stretching

$\boldsymbol{W}$ - Skew component of the velocity gradient

$\boldsymbol{\bar{W}^p}$ - Plastic component of $\boldsymbol{W}$ in the intermediate configuration

Y - Geometric factor

a - Crack length

b - Magnitude of the Burgers vector

$\boldsymbol{b}^s$ - Direction of the s-th slip system

$\boldsymbol{x_p}$ - Coordinates of a point in the intermediate configuration

$\boldsymbol{X}$ - Coordinates of a point in the reference configuration

$\boldsymbol{x}$ - Coordinates of a point in the current configuration

$g_{0,i}$ - normalized activation energy for the i-th component of the Mechanical Threshold Stress model

$i = 1 : m_i$ - Number of thermal components for the Mechanical Threshold Stress Model

k - Boltzman constant

k_0 - Parameter that accounts of hardening deriving from geometrical necessary dislocations

k_1 - Parameter that accounts for dislocation generation

k_2 - Parameter that accounts for material recovering during plastic straining

m_{SF} - Schmid factor of the grain

n - Exponent of the slip rate, characterize the material rate sensitivity

$\boldsymbol{n}^s$ - Normal of the s-th slip system

n_{slip} - Number of slip systems

p, q - Statistical constants that characterize the shape of the energy obstacle profile

p_i, q_i - Statistical constants that characterize the shape of the energy obstacle profile for the i-th component of the Mechanical Threshold Stress model

$q_{G_{ij}}$ - ij component of Q_G

r - Radial distance from the tip

r_p - Plastic zone radius

$r^{(s)}$ - Threshold that accounts for isotropic hardening

s - s-th slip system

w - Specimen width

$\boldsymbol{t}$ - Unrotated Cauchy stress

$\dot{\boldsymbol{t}}$ - Unrotated Cauchy stress rate

$\Delta\sigma$ - Stress range

$\Delta\sigma_{\text{eff}}$ - Effective stress range

$\Delta\epsilon_{\text{yy}}$ - Axial strain difference

ΔG_0 - Gibbs free energy of activation range

ΔK - Stress intensity factor range

ΔK_{eff} - Effective stress intensity factor range

$\Delta K_{\text{I,eff}}$ - Mode I effective stress intensity factor range

Γ - Sum of the magnitude of the slips

Γ_c - Sum of the magnitude of the slips at yielding

α - Nye tensor

$\chi^{(s)}$ - Back-stress on the s-th slip plane that accounts for kinematic hardening

∂y - Small displacement

η - Dislocation interaction constant

γ - Shear

$\dot{\gamma}_0$ - Reference slip rate

$\dot{\gamma}^s$ - Slip rate along the s-th slip system

$\dot{\epsilon}_0$ - Reference strain rate

$\dot{\epsilon}_p$ - Plastic strain rate

ϵ_p - Accumulated plastic strain

ϵ_{yy} - Vertical strain

$\lambda^{(s)}$ - Linear dislocation density along s-th slip plane

μ - Shear modulus

μ_0 - Reference value of the shear modulus

ν - Poisson's ratio

ρ_f - Dislocation density

ρ - Necessary dislocation density

$\boldsymbol{\sigma}$ - Cauchy stress

$\dot{\boldsymbol{\sigma}}$ - Cauchy stress rate

$\mathring{\boldsymbol{\sigma}}$ - Green-Naghdi objective stress rate

σ_{remote} - Remote applied stress

σ_{max} - Maximum applied stress

σ_{min} - Minimum applied stress

σ_{op} - Crack opening stress

$\bar{\tau}$ - Slip system strength component that accounts for work hardening

$\tilde{\tau}$ - Slip system strength

$\tilde{\tau}^*$ - Generic slip system strength

$\tilde{\tau}_i$ - Slip system strength for the i-th component in Mechanical Threshold Stress model

$\hat{\tau}^*$ - Generic threshold stress value of the slip system

$\hat{\tau}_i$ - Saturation strength for the i-th component of the Mechanical Threshold Stress model

τ_a - Athermal component of the slip system strength

$\tau^{(s)}$ - Resolved shear stress on the s-th slip plane

$\hat{\tau}_v$ - Mechanical Threshold Stress model's saturation strength for work hardening

$\hat{\tau}_y$ - Mechanical Threshold Stress model's saturation strength for yield stress

$\tau_\lambda^{(s)}$ - Saturation strength of the s-th slip system related to geometrical necessary dislocations

τ_{remote} - Shear stress related to the remote applied stress

ϑ_0 - Initial slope of the work hardening

$\boldsymbol{\xi}$ - Elastic strain

$\dot{\boldsymbol{\xi}}$ - Elastic strain rate

Contents

List of Figures

List of Tables

CHAPTER 1

Introduction

This first chapter aims to give an introduction on the motivation that led to this thesis work, before describing it in the following chapters. Then an overview of the literature models for the main topics of this thesis is included: crystal plasticity finite element simulation and crack closure simulation.

1.1 Thesis Motivation

Nickel based super-alloys are currently used in gas turbine and aero engines thanks to their excellent mechanical and chemical properties at elevated temperatures [1–3]. Components like turbine blades, which are usually made out of single crystals, require high fatigue and creep properties since they undergo extreme mechanical loads and high temperatures over long time, this makes Ni-based alloy the main considerable option for those kind of applications. Same goes for polycrystalline media that thanks to their excellent resistance to high temperature and corrosion are preferable for components that work in harsh environments, like combustion chamber of gas turbine. The description of this materials micro-structural behaviour through finite element models, which account for crystal plasticity, may help in their design and application.

The micro-structure of materials strongly influences phenomena like strain concentration, local damage, crack propagation et al. Fig. 1.1 shows an example of an electron

backscatter diffraction (EBSD) image taken from a Haynes 230 sample. On the micro scale this Ni-based alloy, as other structural metals, consists of an aggregation of crystalline grains. Each of those has a different orientation of the atomic lattice, which means each grain gives a different answer under mechanical and thermal loads. In Fig. 1.1 each color indicates a different grain with a different lattice orientation. The interfaces separating the grains are the grain boundaries.

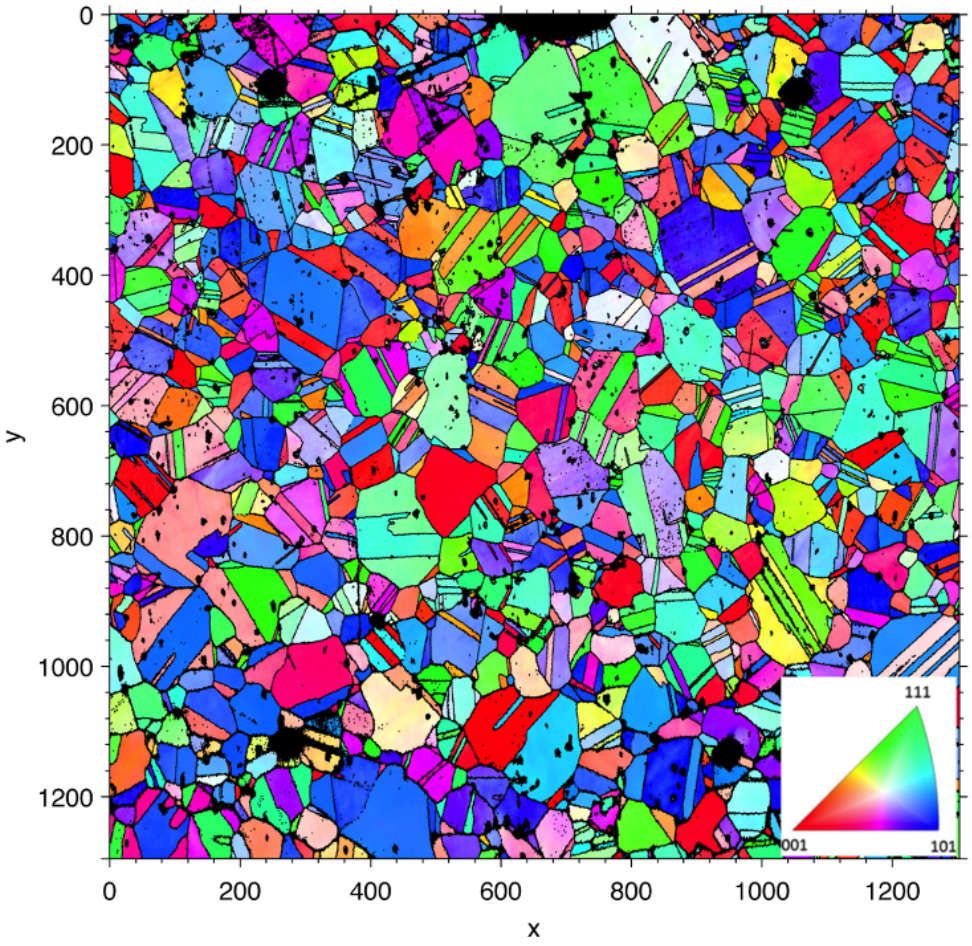

Figure 1.1: *Example of an EBSD conducted on a Haynes 230 specimen.*

Literature shows many works on crystal plasticity simulations [4] in both single crystal and polycrystalline media, but they usually rely on experiments only for macroscopic answer; the local anisotropic behaviour is not directly compared with the one obtained from the experiment itself. This real local behaviour can be evaluated by the digital image correlation technique [5] which is been widely applied in the past years with good results and improving resolution to study strain localization and crack propagation [6, 7]. The link between local experiment observation and the crystal plasticity finite element results is still an open field which can be used to corroborate models and

acquire information about the micro scale that an experiment alone cannot reach.

This thesis aim to apply the crystal plasticity code embedded in Warp3D [8] (an open source software) to reproduce and study further the micro-structural behaviour of a Ni-based super-alloy, Haynes 230. Experiments and their results will be discussed as a start for the model development and as a comparison for the simulation results on the micro scale. A physically-based theory of crystal plasticity simulate the material answer, to an applied load, on the grains scale. Detailed crystal plasticity simulations on single crystal and polycrystalline specimens, considering various type of tests (tensile, ratcheting and crack propagation), will be discussed. The numerical results will be compared with the experimental data on macro-scale and micro-scale. These comparisons between the local prediction of the model and the DIC results will be used as a reference to validate Warp3D crystal plasticity model.

The result of this research is the evaluation of the prediction capabilities of the crystal plasticity code adopted: whether it simulates cyclic loadings or crack propagation. Since the outcome of the simulation leads to a good description of the experiments, the application of this model may reveal itself useful for both crack nucleation prediction and crack propagation. In the first case may predicts where the crack would nucleate, due to stress and strains intensifications. In the second case, with an existing crack, determine which are the driving forces that make it propagates.

1.2 Haynes 230

The thesis will focus on the analysis, for both experiments and simulations, of a nickel-based super-alloy, Haynes 230 [9]. It is a solution strengthened alloy, which exhibits high resistance to corrosion, oxidation and creep: those characteristics makes it a good choice for application in aerospace and energy industries (gas turbines and combustion chamber). Its high temperature properties are granted by the addition of chromium, tungsten and molybdenum; Table 1.1 shows Haynes 230 chemical composition.

Table 1.1: *Chemical composition (%wt) of Haynes 230.*

Al	B	C	Co	Cr	Cu	Fe	La	Mn
0.35	0.005	0.1	0.16	22.14	0.04	1.14	0.015	0.5
Mo	Ni	P	S	Si	Ti	W	Zr	
1.25	59.5	0.005	0.002	0.49	0.01	14.25	0.01	

Many studies focused their attention on Haynes 230 in both its single crystal and polycrystalline forms, and its characterization is still a work in progress. High oxidation resistance at high temperature was demonstrated in [10–14], while fatigue crack

growth at room and high temperature concerned the studies of [15], registering a crack growth resistance decreasing with the temperature. Finally the mechanical behaviour was studied at room and various high temperature in [16–18].

Micro-structurally Haynes 230 is an FCC material in its lattice and consists of a collection of grains. Each grain can be considered as a metal crystal, a structure of atoms organized in a regular and repeated pattern, the lattice. The properties of each grain depends on its orientation, which can be defined as the lattice relative rotation with respect to a reference coordinates system. The representation of the rotation can be done considering the Euler angles: Considering the Bunge convention [19], a sequence of three angles $(\phi_1\,,\,\Theta\,,\,\phi_2)$ defines the rotation along X_3, then about X_1 and finally around the rotated X_3 (see Fig. 1.2). Fig. 1.1 is the result of an Electron Backscatter

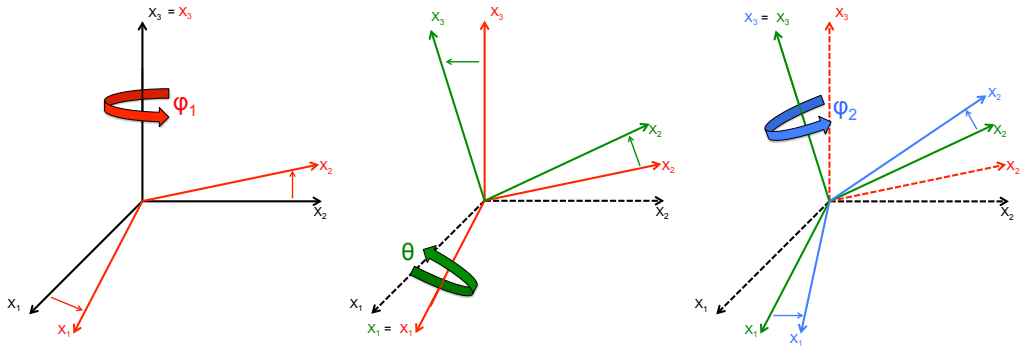

Figure 1.2: *Euler angles sequence for Bunge convention.*

Diffraction analysis [20] conducted on a Haynes 230 specimen. Each grain generally has a different orientation and its properties are affected by that, implying that at the grain scale the material exhibits inhomogeneous properties. The grain boundaries can be treated as different material interfaces where strong stress and strain gradients can generate as a result of the mismatching orientation. The local inhomogeneity derives from the single crystal anisotropy itself (the grains separately can be treated as single crystals), which can be decomposed in an elastic anisotropy (cubic anisotropy for FCC materials) and a plastic one. The nature of plastic deformation at grain scale is related to the motion/slip of dislocations (defects in the atomic lattice) along a certain number of lattice's allowed slip systems. The slip system is defined by the combination of a lattice plane and a direction on that plane. The slip system geometry directly depends on the category of atomic lattice: FCC metals have 12 slip systems (Table 1.2), each one is a combination of a close-packed plane and a close-packed direction, see Fig. 1.3 [21, 22].

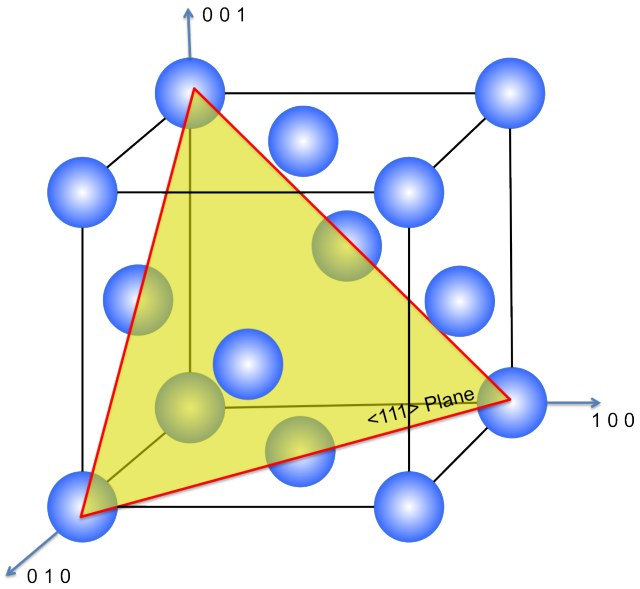

Figure 1.3: *FCC lattice scheme, evidence on (111) slip plane.*

Table 1.2: *Possible slip systems in a FCC lattice.*

Slip System	Slip Plane	Slip Direction	Slip System	Slip Plane	Slip Direction
1	(1 1 1)	[$\bar{1}$ 0 1]	7	($\bar{1}$ 1 1)	[1 0 1]
2	(1 1 1)	[$\bar{1}$ 1 0]	8	($\bar{1}$ 1 1)	[1 1 0]
3	(1 1 1)	[0 $\bar{1}$ 1]	9	($\bar{1}$ 1 1)	[0 $\bar{1}$ 1]
4	($\bar{1}$ $\bar{1}$ 1)	[0 1 1]	10	(1 $\bar{1}$ 1)	[0 1 1]
5	($\bar{1}$ $\bar{1}$ 1)	[$\bar{1}$ 1 0]	11	(1 $\bar{1}$ 1)	[1 1 0]
6	($\bar{1}$ $\bar{1}$ 1)	[1 0 1]	12	(1 $\bar{1}$ 1)	[$\bar{1}$ 0 1]

1.3 Crystal Plasticity Modeling - Literature Review

With the increasing capabilities of processors computational efficiency, numerical simulations which are able to realistically describe the micro-structure behaviour have been strongly developed [8, 23, 24]. The idea is to establish a multi-scale model which goes from a complex components to its atomic levels, going through steps where crystal plasticity has a main role (Fig. 1.4). This means that Crystal Plasticity Finite Element (CPFE) methods have evolved to create a link between the corroborated theoretical studies on micro-structural mechanics and the continuum field of deformation theories. The evolution of CPFE method from the first simulation by Pierce, Asaro and Needleman in 1982 [25], where they characterized the local answer of a single crystal considering only two slip systems, brought to the possibility to account for FCC models (12 slip systems) [26], BCC models (up to 48 slip systems) [27] and HCP models

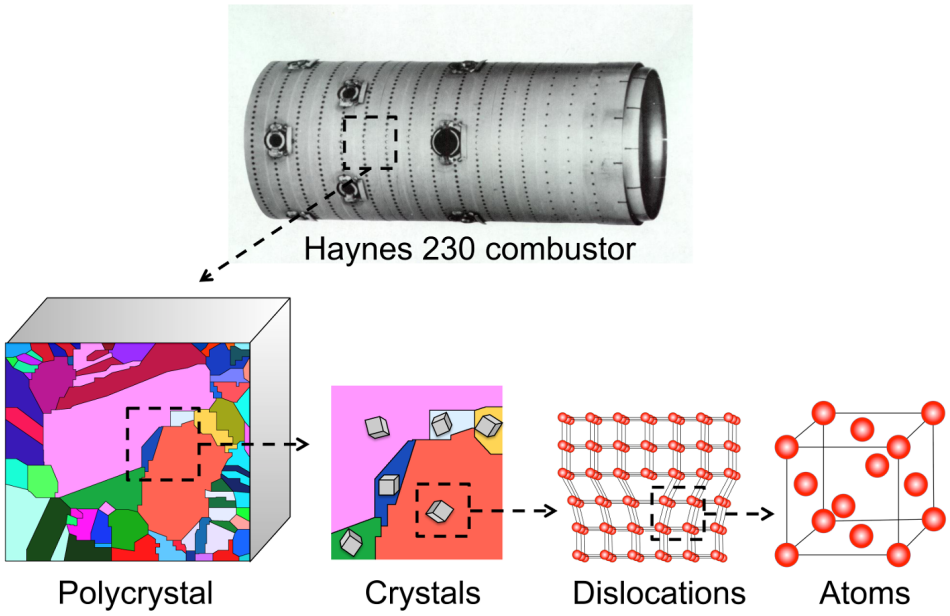

Figure 1.4: *Logical flow from a component [9] to atoms going throughout the various length scale in material analysis.*

(12 slip systems) [28, 29]. Most of the works in this field relies on the hypothesis that dislocation motion is the main vector for plastic deformation in metals, later on other mechanisms were introduced as competing phenomena for CP plastic deformation, for example: martensite formation [30] and mechanical twinning [31].

Finally CPFE simulation can be applied on both microscopic and macroscopic scale. Example of small scale applications (see Fig. 1.5) are related to: grain mechanics (considering grain boundaries effects) [4, 32] and its effect on the macroscopic scale [33, 34]; damage prediction [35]; life prediction [36]; simulation of micro mechanical experiments [37]. In the specific, Fig. 1.5, shows the results of: Musienko et Al. [4], where strain accumulates along grains and grain boundaries in a tensile test of a random generated polycrystalline reference volume; Zhang et Al. [36], where the local behaviour of the material is studied for low cycle fatigue varying the number of grains inside a polycrystalline reference volume element. Many products nowadays, especially in micro-electro mechanical systems, has dimensions so reduced that are of the same order of the grain scale and so CP formulation can help in their study and design.

This tools may be of appreciable aid when they are used to achieve some knowledge in the following fields:

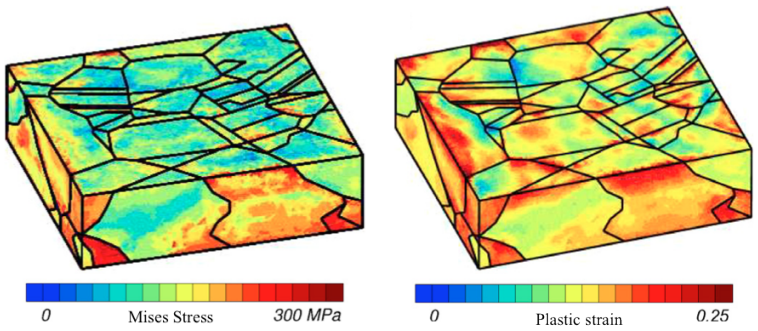

(a)

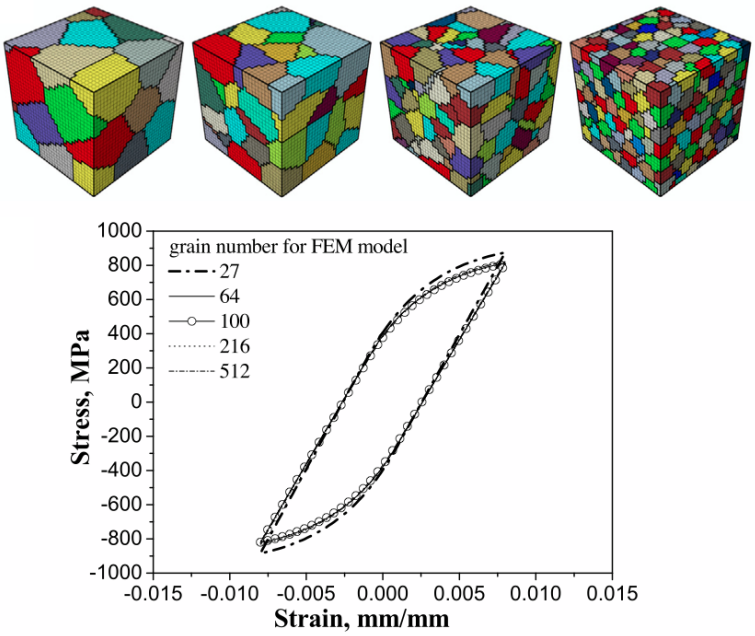

(b)

Figure 1.5: *a) Stress and plastic strain accumulation in a polycrystalline structure after a tensile test [4]; b) Cyclic stress strain answer of different polycrystalline RVE containing different numbers and size of grains [36].*

- Micro-mechanics behaviour, for example the study of the localization of deformation due to incompatibilities between neighbours grains;
- Industrial components, for example those components that have a size comparable with those of the heterogeneities;
- Prediction of the properties of heterogeneous materials, this kind of estimations usually relies on the definition of some kind of reference volume element;
- Simulation of local damage process, on the local scale the damage is lead by the

maximum stress-strain concentration which can be found in certain critical point within the heterogeneous micro-structure.

The model used in CPFE relies for the kinematics of the lattice on the multiplicative decomposition of the deformation gradient originally proposed by Lee [38] and summarized like in Fig. 1.6:

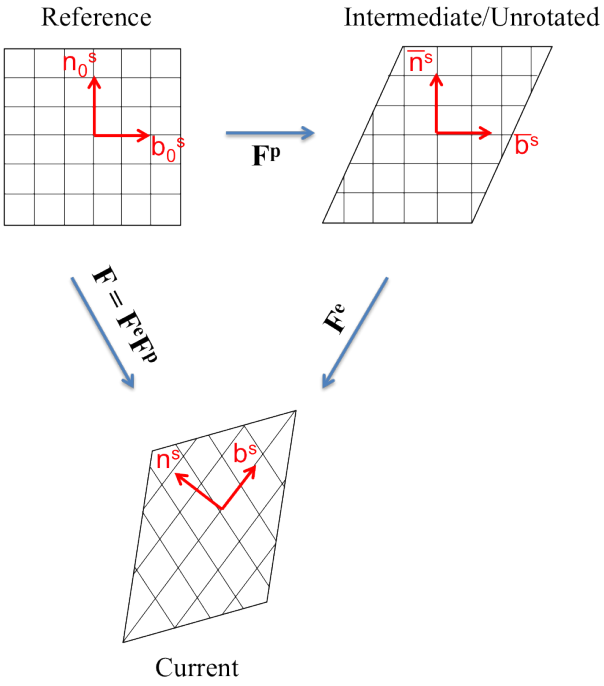

Figure 1.6: *Multiplicative decomposition for the deformation gradient used in CP modeling.*

$$\boldsymbol{F} = \boldsymbol{F^e}\,\boldsymbol{F^p} \tag{1.1}$$

with $\boldsymbol{F}$ representing the deformation gradient which can be decomposed in its elastic ($\boldsymbol{F^e}$) and plastic ($\boldsymbol{F^p}$) components. The plastic deformation evolves as [25]:

$$\dot{\boldsymbol{F}}^{\boldsymbol{p}} = \bar{\boldsymbol{L}}^{\boldsymbol{p}}\,\boldsymbol{F^p} \tag{1.2}$$

$\bar{\boldsymbol{L}}^{\boldsymbol{p}}$ is the plastic velocity gradient and, under the hypothesis that the leading deformation process is the dislocation slip, can be formulated as:

$$\bar{\boldsymbol{L}}^{\boldsymbol{p}} = \sum_{s=1}^{n_{slip}} \dot{\gamma}^{(s)} \left(\boldsymbol{b}^{(s)} \otimes \boldsymbol{n}^{(s)}\right) \tag{1.3}$$

where $\boldsymbol{b}^{(s)}$ and $n^{(s)}$ are, respectively, the unit vector for slip direction and normal to the slip plane of the s-th slip system; $\dot{\gamma}^{(s)}$ is the shear rate on the same system (n_{slip} is the number of active slip systems). A more extensive description of the kinematics will be discussed in section 2.1.

The description of the shear rate $\dot{\gamma}^{(s)}$ as a function of the external stresses relies on the definition of constitutive equations. In fact the kinematics describe the geometrical feature of anisotropy of crystal mechanics, the constitutive law aims to capture the physics of material behaviour.

The constitutive models can be summarized in two macro categories: the phenomenological constitutive models and the physically based one.

Phenomenological constitutive models

Are mostly based on the critical resolved shear stress $\tau^{(s)}$, and the $\dot{\gamma}^{(s)}$ flow rule can be written as [24]:

$$\dot{\gamma}^{(s)} = \left\langle \frac{\left|\tau^{(s)} - \chi^{(s)}\right| - r^{(s)}}{K^{(s)}} \right\rangle^{n} \text{sign}\left(\tau^{(s)} - \chi^{(s)}\right) \tag{1.4}$$

$K^{(s)}$ and n are related to the rate sensitivity of the shear rate. In Eq. (1.4) two hardening variables appear for the s-th slip plane: $r^{(s)}$ for the isotropic hardening and $\chi^{(s)}$ which is an back-stress associated with the kinematic hardening. Kinematic hardening at the level of grains indirectly describes the possible formation of dislocation structures, especially under cyclic loading. A drawback of this model is that the material state is primarily described by the critical resolved shear stress, without considering the lattice defect population [39].

Physically based constitutive models

Rely on internal variables for the flow rule definition and work under the hypothesis that for plasticity the most important variable is the dislocation density, as dislocation are carrier of plastic deformation [40]. The results in terms of overall answer do no differ significantly from those obtained with phenomenological models [23].

This dislocation density based constitutive modeling [41] to reproduce viscoplastic behaviour of crystalline material relies on Kocks and Mecking work [42], and it has been proven capable to give a reliable description of the materials mechanical response. The shear rate can be defined as:

$$\dot{\gamma}^{(s)} = \frac{\dot{\gamma}^{0}}{\tilde{\tau}^{*}} \left| \frac{\tau^{(s)}}{\tilde{\tau}^{*}} \right|^{n-1} \tau^{(s)} \tag{1.5}$$

where $\dot{\gamma}^{0}$ is a reference shear rate; $\tau^{(s)}$ is the resolved shear stress; n is the exponent of the shear rate which accounts for rate sensitivity; $\tilde{\tau}^{*}$ is a generic slip system strength. The definition of $\tilde{\tau}^{*}$ relies on the introduction of a suitable equation of the kinematics

response, adopted by Kocks, incorporates an Arrhenius type formulation of the following type [43] to describe the plastic strain rate:

$$\dot{\epsilon}_p \;=\; \dot{\epsilon}_0 \,\exp\left[-\frac{\Delta G_0}{kbT}\left(1-\left(\frac{\tilde{\tau}^*}{\hat{\tau}^*}\right)^p\right)^q\right] \tag{1.6}$$

where ΔG_0 is the value for the Gibbs free energy of activation; p and q are fitting parameters; k is the Boltzman constant; b is the magnitude of the Burgers vector; T is the temperature; $\dot{\epsilon}_0$ is a reference strain rate; $\hat{\tau}^*$ is a general threshold strength. As plastic deformation proceed, a separate equation, which incorporates eq. (1.6), is needed to describe the evolution of $\tilde{\tau}$:

$$\tilde{\tau}^* \;=\; \mathrm{f}\left(\dot{\epsilon}_p, T\right) \tag{1.7}$$

In section 2.2 will be discussed the adopted model for this thesis simulations, based on Kocks works.

1.4 Crack Closure Overview

In high cycle fatigue, when plastic strains affects only a small region of material, ahead of the crack tip, crack growth rate ($\mathrm{d}a/\mathrm{d}N$) is related to the stress intensity factor range ΔK through Paris equation [44]:

$$\frac{\mathrm{d}a}{\mathrm{d}N} \;=\; A\left(\Delta K\right)^m \tag{1.8}$$

Experimental campaigns [45], showed a primary influence of the load ratio on the material constants (A and m): higher load ratios bring to higher crack growth rates. In 1970, Elber [46] observed that the crack stays closed for part of the loading cycle, even if the applied stress is tensile. Since this can not be explained with elasticity theory it implies that this is a phenomena related to the plastic strains acting at the crack tip. During crack propagation a plastic zone emanates from crack tip, and along crack flanks a plastic wake is generated (Fig. 1.7): this zone, characterized by residual compressive stresses, is the one responsible for crack closure, implying that the crack opens when the tensile stress overcomes this residual stress state. Then, Elber, considering only the ΔK part which overcome the crack-closure effects, was able to remove the load ratio dependency. This led to the definition of a parameter able to capture the crack growth rates, the effective stress intensity factor range (ΔK_{eff}), which considers that crack closure has a main role in crack propagation. Also other phenomena [47], roughness and oxidation within them, have influences on crack closure, and play significant role in near-threshold region or specific load condition.

In literature various numerical approach that aims to capture crack closure can be found, whether they consider homogeneous media or crystals.

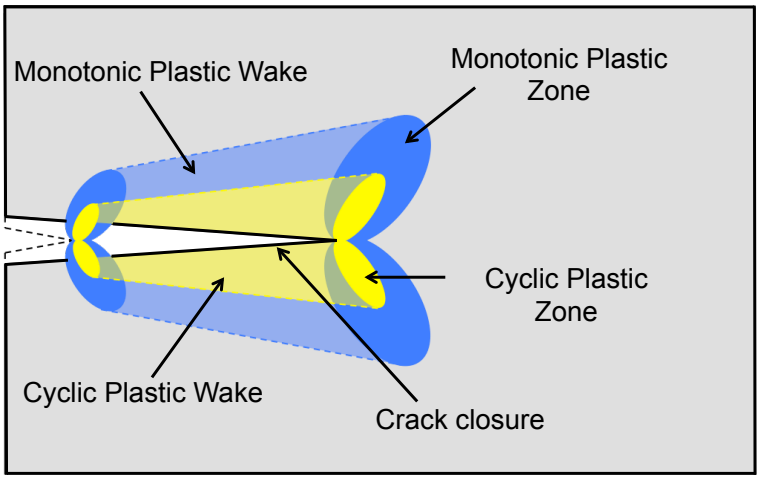

Figure 1.7: *Plastic wake definition for both cyclic and monotonic crack advancements.*

FE analysis on crack closure requires a mesh with an initial crack, then the model is remotely loaded in traction. Most models consider constant amplitude loading, the load is cycled between the minimum and the maximum applied stresses. During this cyclic loading the crack is advanced with some computational features leading to the formation of the plastic wake behind the crack tip.

Starting from this background many authors analysed this kind of models first with 2D and then with 3D simulations. Since the model has to capture the plastic zones near the crack tip, a mesh refinement scheme was studied in [48–50]: McClung el al. [51,52] performed this kind of study on a M(T) geometry finding out that the mesh dimensions should take into account the extension of the forward plastic zone in the crack planes:

$$\frac{\Delta a}{r_p} \leq 0.05 \tag{1.9}$$

where Δa is the crack advancement, usually corresponding to the mesh dimension, and r_p is the plastic radius ahead of crack tip.

Once the mesh dimension has been defined the study of the crack growth has to consider that the crack opening load typically increases with the crack growth until a stabilized value [53]: the crack has to advance completely through the initial plastic zone to reach stabilization. The crack advancement requires a changing in the boundary condition, here the main issue to pay attention is the problem of interpenetration of crack flanks at the minimum load, this has to be prevented. It can be achieved by changing the stiffness of spring elements attached to the crack surface [54], by removing or imposing crack surface nodal constrains [50] or by contact elements [55].

Then a scheme for the crack advancement has to be considered: the common approach is to release, according to the chosen features, the crack tip node advancing the

crack of a length equal to the element size. The main issue discussed in literature for this step is how and when to perform this release: at maximum load [51, 56], at minimum load [51,54], every cycle [56] or every second cycle [53]. Some of those approach may lead to convergence problems, especially with release at maximum load.

For 2D models a distinction between plane stress and plane strain has to be done since they strongly influence the plastic deformation around the crack tip. Many studies [51, 57, 58] stated that the opening level in plane strain is lower then in plane stress.

Following this last point, 3D geometry has to consider that the crack opening value vary along the crack front (ideally the external surface is in a plane stress condition and the mid plane is in a plane strain one), bringing to different growing rates along the front under cyclic loading, thus to a non-uniform crack front. For simplicity this shape evolution is neglected and the crack front is extended uniformly during FE analysis. Following the initial work of Chermahini [62], Dodds et al. [59, 63, 64] performed finite element analyses on various specimen geometry and loading ratio, showing the influence of crack opening along the entire crack front (Fig. 1.8-a).

Finally it should be noted that when the crack is small compared to the grain size, plastic deformation is no longer isotropic and homogeneous, then constitutive crystal plasticity formulation are needed. In literature, different crystal plasticity codes have been proposed, with the aim to describe crack nucleation in polycrystalline aggregates [65]. The formulation of crystal plasticity is due to the work of Taylor, Rice, Hill, Asaro and Needleman [66–69]: starting from experimental observation, in these models, inelastic strain is computed as a function of slip occurring in particular crystallographic planes. An initial application of crystal plasticity to the study of plastic zone in single crystal was presented in [70], following the study presented in [71] and [72] for single crystal C(T) specimen under single load ramp gave the first comparison with experiments. A study of fatigue crack closure with CP formulation on polycrystalline aggregates was conducted by Gall et al. [48, 73], then also Potirniche in [60] studied short crack propagation through a grain boundary in Aluminium (Fig. 1.8-b). Recently, a different approach based on cohesive elements has been proposed for the study of a Ni-based super-alloy single crystal [74] and re-meshing technique has been applied in a short fatigue crack propagation under mixed mode loadings [61] (Fig. 1.8-c).

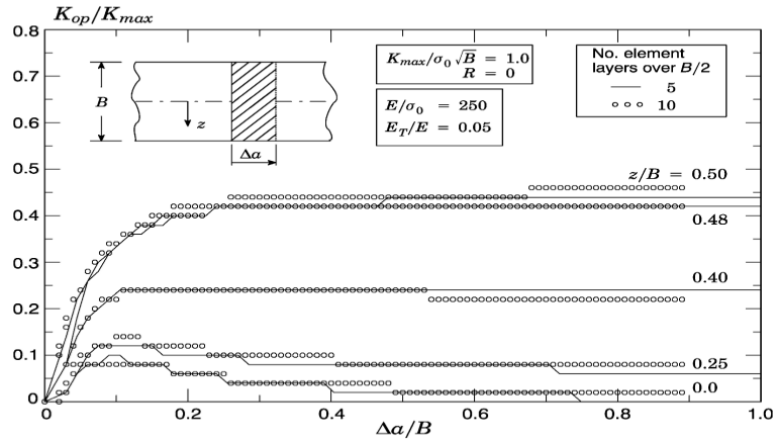

(a)

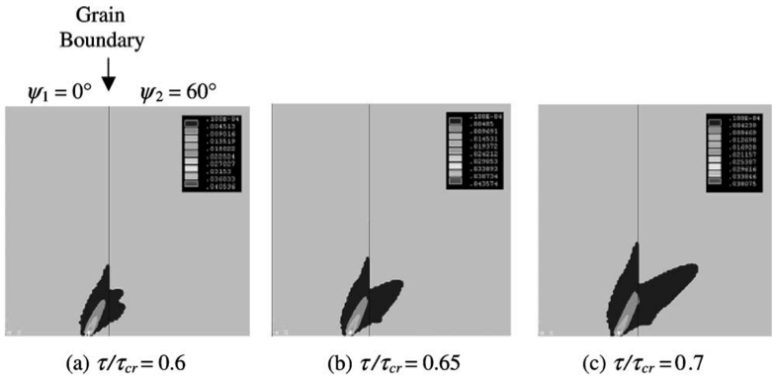

(b)

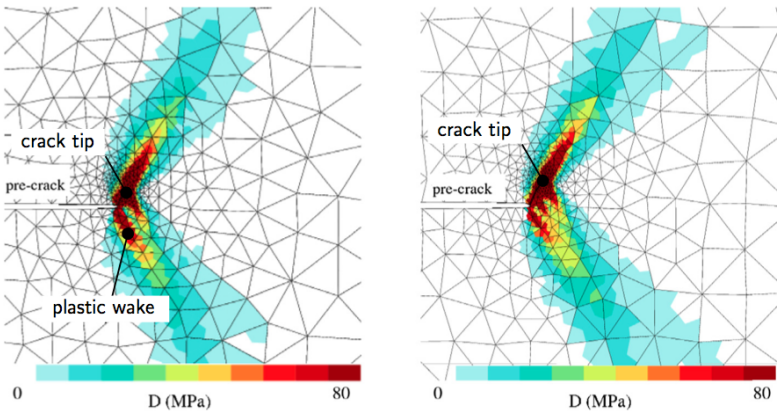

(c)

Figure 1.8: *a) Variation of the opening level throughout the thickness during crack propagation [59]; b) Grain boundary effect on the crack tip plastic zone as a function of the applied load with respect to the resolved shear stress [60]; c) Mixed mode crack propagation in a single crystal and plastic wake generation [61].*

1.5 Structure Of The Thesis

Following this introductory chapter the thesis is divided as:

Chapter 2: *Crystal Plasticity Code*: a description of the model implemented in the adopted software is provided: the kinematics of crystals and the definition of the slip systems hardening rule are discussed.

Chapter 3: *Tensile Mechanical Behaviour*: the tensile behaviour is studied at first on single crystal specimens at room temperature in order to evaluate the crystal plasticity model parameters. Then the study shifts on the simulation of a polycrystalline high temperature tensile test, focusing on various modeling techniques, like the introduction of carbides in the crystals matrix, and making a comparison with an experiment conducted with digital image correlation, which identifies the real strain localization along the grains.

Chapter 4: *Simulation of a Ratcheting Test*: the cyclic behaviour of the material at room temperature is studied considering a ratcheting test. The simulations aims to capture strain localizations accumulating cycle after cycle and that have been observed experimentally by digital image correlation.

Chapter 5: *Fatigue Crack Growth in Single Crystals*: fatigue crack growth is investigated in single crystals simulating crack advancement by means of node release technique. The simulations aim to capture the extension of the strain field and the crack opening levels, both measured experimentally by digital image correlation.

Chapter 6: *Fatigue Crack Growth in Polycrystalline Media*: fatigue crack growth is investigated on polycrystalline specimens. At first a test with a non-propagating crack is analyzed to compare simulation predictions in extension of the plastic zone with experimental results. Then random generated crystal structures are considered to simulate crack propagation. Their results aim to give a good estimation of the opening levels observed with the experiments.

CHAPTER 2

Crystal Plasticity Code

On grain scale, plasticity evolves as dislocation slip along a finite number of slip systems, a number that depends on the crystalline structure of the material. Models that represent this micro scale plastic deformation are techniques like discrete dislocation and atomistic simulations, and continuum theory like crystal plasticity. Finite element can incorporate CP as it is a continuum theory of plastic deformation with an anisotropic flow rule. This definition classifies CP as a meso-scale theory of deformation which represents the deformation on the micro-scale as an average of the effective dislocation motion [68]: this imposes a limitation on the phenomena that the model can reproduce, it won't be able to describe the total dislocation field, the dislocation pile ups and the persistent slip bands.

In this Chapter a background on the kinematics of crystal deformation and the adopted slip system work hardening model will be discussed. The crystal plasticity finite element model adopted for this Thesis simulations refers to the one implemented in Warp3D finite element software [8].

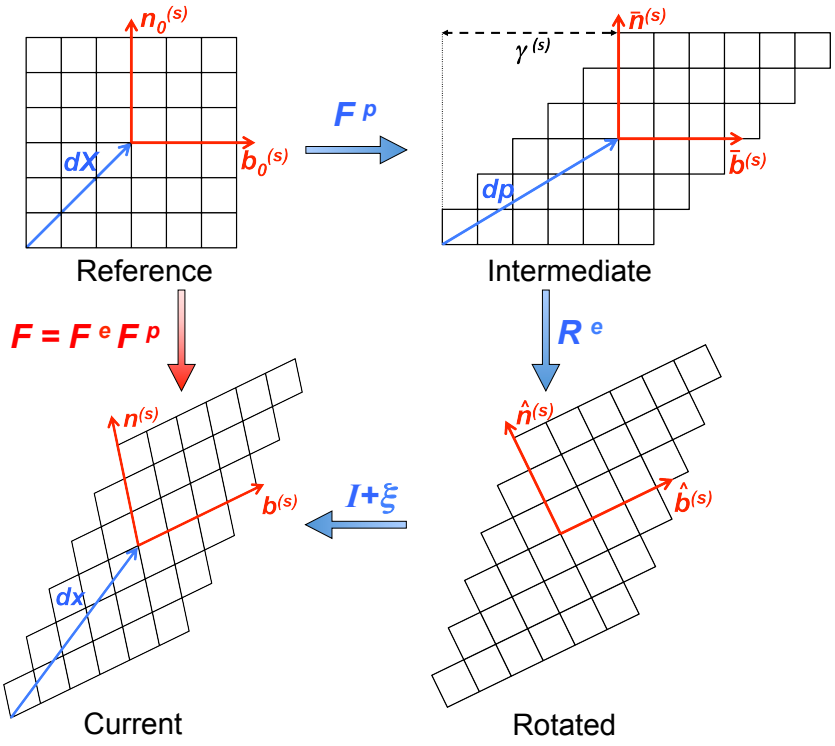

Figure 2.1: *Kinematic decomposition of the deformation gradient following the standard sequence of configurations [21]. Vectors b and n follows the notation of each configuration.*

2.1 Crystal Kinematics Of Deformation

The kinematics of a crystal are a combination of dislocation slip, lattice rotation and elastic stretch [21]. Fig. 2.1 illustrates the multiplicative decomposition [38] of the deformation gradient. Starting from the reference configuration, where no loads are applied and the crystal orientations are those measured (by EBSD for example), the application of a load leads to a deformation of the lattice to the current configuration. This deformation con be expanded considering two intermediate steps, plastic deformation and elastic deformation: during plastic deformation, which involves dislocation motion, the lattice axes do not rotate; during elastic deformation both lattice rotation and elastic distortion occur. The deformation gradient can be written as:

$$\mathrm{d}\boldsymbol{x} = \boldsymbol{F}\mathrm{d}\boldsymbol{X} \tag{2.1}$$

$$\boldsymbol{F} = \boldsymbol{F}^{\boldsymbol{e}}\boldsymbol{F}^{\boldsymbol{p}} \tag{2.2}$$

where $\boldsymbol{x}$ and $\boldsymbol{X}$ defines the points, respectively, in current and in reference coordinate systems; $\boldsymbol{F}$ is the deformation gradient which can be decomposed in its elastic $(\boldsymbol{F^e})$

and its plastic ($\boldsymbol{F^p}$) components. Eq. (2.1) can be rewritten as:

$$\boldsymbol{F} = \frac{\mathrm{d}\boldsymbol{x}}{\mathrm{d}\boldsymbol{X}} = \frac{\mathrm{d}\boldsymbol{x_p}}{\mathrm{d}\boldsymbol{X}}\frac{\mathrm{d}\boldsymbol{x}}{\mathrm{d}\boldsymbol{x_p}} \tag{2.3}$$

where $\boldsymbol{x_p}$ defines the points in the intermediate coordinate system. From eq. (2.3) follows the definition of $\boldsymbol{F^p} = \mathrm{d}\boldsymbol{x_p}/\mathrm{d}\boldsymbol{X}$ and $\boldsymbol{F^e} = \mathrm{d}\boldsymbol{x}/\mathrm{d}\boldsymbol{x_p}$: the total deformation follows a defined sequence having first the plastic deformation and then the elastic one. The elastic part account for lattice rotation and stretching, the plastic for permanent deformation. Considering the plastic gradient for one slip system in the intermediate reference system, it is possible to evaluate the formulation for $\boldsymbol{F^p}$ on the s-th slip system when a shear $\gamma^{(s)}$ is applied:

$$\boldsymbol{u^{p^{(s)}}} = \gamma^{(s)}\left(\bar{\boldsymbol{n}}^{(\boldsymbol{s})}\boldsymbol{X}\right)\bar{\boldsymbol{b}}^{(\boldsymbol{s})} = \gamma^{(s)}\bar{\boldsymbol{b}}^{(\boldsymbol{s})} \otimes \bar{\boldsymbol{n}}^{(\boldsymbol{s})}\boldsymbol{X} \tag{2.4}$$

$$\boldsymbol{F^p} = \boldsymbol{I} + \frac{\partial \boldsymbol{u}}{\partial \boldsymbol{X}} \qquad \boldsymbol{F^{p^{(s)}}} = \boldsymbol{I} + \bar{\boldsymbol{b}}^{(\boldsymbol{s})} \otimes \bar{\boldsymbol{n}}^{(\boldsymbol{s})}\gamma^{(s)} \tag{2.5}$$

where $\boldsymbol{u^{p(s)}}$ is the plastic displacement on the s-th slip system; $\bar{\boldsymbol{b}}^{(\boldsymbol{s})}$ and $\bar{\boldsymbol{n}}^{(\boldsymbol{s})}$ are, respectively, the unit vector in the slip direction and the unit normal vector in the slip plane of the s-th system (see Fig. 2.2) and in the intermediate configuration. Going

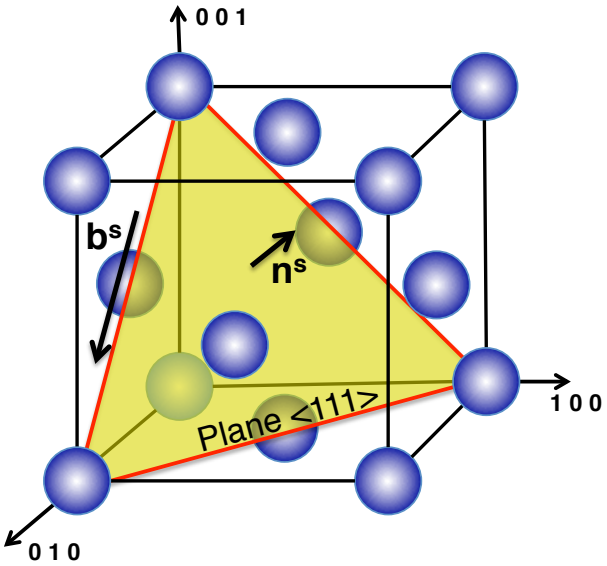

Figure 2.2: *Lattice structure of an FCC material, with focus on <111> slip plane and its slip* $\boldsymbol{b}^{(s)}$ *and normal* $\boldsymbol{n}^{(s)}$ *directions.*

back to eq. (2.2) and considering $\boldsymbol{F^e} = \boldsymbol{V^e}\boldsymbol{R^e}$, the elastic deformation gradient is here decomposed in its components of stretching ($\boldsymbol{V^e}$) and rotation ($\boldsymbol{R^e}$), it is possible to write:

$$\boldsymbol{F} = \boldsymbol{F^e}\,\boldsymbol{F^p} = \boldsymbol{V^e}\,\boldsymbol{R^e}\,\boldsymbol{F^p} = (\boldsymbol{I} + \boldsymbol{\xi})\,\boldsymbol{R^e}\,\boldsymbol{F^p} \tag{2.6}$$

In eq. (2.6) the stretching is written as $(\boldsymbol{I} + \boldsymbol{\xi})$, where $\boldsymbol{I}$ is the unit matrix and $\boldsymbol{\xi}$ is a small elastic strain; under high plastic strain condition, elastic strain can be considered small so that $||\boldsymbol{\xi}|| \ll 1$. Considering eq. (2.6), it is possible to define the velocity gradient $\boldsymbol{L}$ in the current configuration (see Fig. 2.1) as:

$$\boldsymbol{L} = \dot{\boldsymbol{F}}\,\boldsymbol{F}^{-1} = \dot{\boldsymbol{F}}^{\boldsymbol{e}}\,\boldsymbol{F}^{\boldsymbol{e}^{-1}} + \boldsymbol{F}^{\boldsymbol{e}}\,\dot{\boldsymbol{F}}^{\boldsymbol{p}}\,\boldsymbol{F}^{\boldsymbol{p}^{-1}}\,\boldsymbol{F}^{\boldsymbol{e}^{-1}} = \dot{\boldsymbol{F}}^{\boldsymbol{e}}\,\boldsymbol{F}^{\boldsymbol{e}^{-1}} + \boldsymbol{F}^{\boldsymbol{e}}\,\bar{\boldsymbol{L}}^{\boldsymbol{p}}\,\boldsymbol{F}^{\boldsymbol{e}^{-1}} \tag{2.7}$$

$\bar{\boldsymbol{L}}^{\boldsymbol{p}} = \dot{\boldsymbol{F}}^{\boldsymbol{p}}\,\boldsymbol{F}^{\boldsymbol{p}^{-1}}$ is defined as a constitutive tensor, which represents the plastic velocity gradient with respect to the intermediate configuration. Eq. (2.7), considering Eq. (2.6) and neglecting the quadratic terms in $\boldsymbol{\xi}$ and $\dot{\boldsymbol{\xi}}$, may be rearranged as:

$$\boldsymbol{L} = \dot{\boldsymbol{R}}^{\boldsymbol{e}}\boldsymbol{R}^{\boldsymbol{e}^T} + \dot{\boldsymbol{\xi}} + \dot{\boldsymbol{R}}^{\boldsymbol{e}}\boldsymbol{R}^{\boldsymbol{e}^T}\boldsymbol{\xi} - \boldsymbol{\xi}\dot{\boldsymbol{R}}^{\boldsymbol{e}}\boldsymbol{R}^{\boldsymbol{e}^T} + \boldsymbol{R}^{\boldsymbol{e}}\bar{\boldsymbol{L}}^{\boldsymbol{p}}\boldsymbol{R}^{\boldsymbol{e}^T} + \boldsymbol{\xi}\boldsymbol{R}^{\boldsymbol{e}}\bar{\boldsymbol{L}}^{\boldsymbol{p}}\boldsymbol{R}^{\boldsymbol{e}^T} - \boldsymbol{R}^{\boldsymbol{e}}\bar{\boldsymbol{L}}^{\boldsymbol{p}}\boldsymbol{R}^{\boldsymbol{e}^T}\boldsymbol{\xi} \tag{2.8}$$

Expressing $\boldsymbol{L} = \boldsymbol{D} + \boldsymbol{W}$ [23] as the sum of the skew $\boldsymbol{W} = 1/2\left(\boldsymbol{L} - \boldsymbol{L}^T\right)$ and the symmetric $\boldsymbol{D} = 1/2\left(\boldsymbol{L} + \boldsymbol{L}^T\right)$ components, the following relations can be derived:

$$\boldsymbol{D} = \dot{\boldsymbol{\xi}} + \boldsymbol{\xi}\dot{\boldsymbol{R}}^{\boldsymbol{e}}\boldsymbol{R}^{\boldsymbol{e}^T} - \dot{\boldsymbol{R}}^{\boldsymbol{e}}\boldsymbol{R}^{\boldsymbol{e}^T}\boldsymbol{\xi} + \boldsymbol{R}^{\boldsymbol{e}}\bar{\boldsymbol{D}}^{\boldsymbol{p}}\boldsymbol{R}^{\boldsymbol{e}^T} + \boldsymbol{\xi}\boldsymbol{R}^{\boldsymbol{e}}\bar{\boldsymbol{W}}^{\boldsymbol{p}}\boldsymbol{R}^{\boldsymbol{e}^T} - \boldsymbol{R}^{\boldsymbol{e}}\bar{\boldsymbol{W}}^{\boldsymbol{p}}\boldsymbol{R}^{\boldsymbol{e}^T}\boldsymbol{\xi} \tag{2.9}$$

$$\boldsymbol{W} = \dot{\boldsymbol{R}}^{\boldsymbol{e}}\boldsymbol{R}^{\boldsymbol{e}^T} + \boldsymbol{R}^{\boldsymbol{e}}\bar{\boldsymbol{W}}^{\boldsymbol{p}}\boldsymbol{R}^{\boldsymbol{e}^T} + \boldsymbol{\xi}\boldsymbol{R}^{\boldsymbol{e}}\bar{\boldsymbol{D}}^{\boldsymbol{p}}\boldsymbol{R}^{\boldsymbol{e}^T} - \boldsymbol{R}^{\boldsymbol{e}}\bar{\boldsymbol{D}}^{\boldsymbol{p}}\boldsymbol{R}^{\boldsymbol{e}^T}\boldsymbol{\xi} \tag{2.10}$$

$\bar{\boldsymbol{D}}^{\boldsymbol{p}}$ and $\bar{\boldsymbol{W}}^{\boldsymbol{p}}$ can be obtained from the plastic velocity gradient. Considering a single crystal and assuming that all the plastic straining is correlated to the slip on slip planes, $\bar{\boldsymbol{L}}^{\boldsymbol{p}}$ can be expressed as an additive decomposition of plastic shear deformation in a lattice frame [75], modifying eq. (2.5) (using $\dot{\boldsymbol{n}}^{(s)} = \dot{\boldsymbol{b}}^{(s)} = 0$ and $\boldsymbol{n}^{(s)} \cdot \boldsymbol{b}^{(s)} = 0$):

$$\bar{\boldsymbol{L}}^{\boldsymbol{p}} = \sum_{s=1}^{n_{slip}} \dot{\gamma}^{(s)}\left(\bar{\boldsymbol{b}}^{(s)} \otimes \bar{\boldsymbol{n}}^{(s)}\right) \tag{2.11}$$

In eq. (2.11) $\bar{\boldsymbol{b}}^{(s)}$ and $\bar{\boldsymbol{n}}^{(s)}$ are related to the intermediate configuration and $\dot{\gamma}^{(s)}$ is the slip rate along each slip system. $\bar{\boldsymbol{L}}^{\boldsymbol{p}}$ can be decomposed into its skew and symmetric components [25]:

$$\begin{aligned} \bar{\boldsymbol{D}}^{\boldsymbol{p}} &= \sum_{s=1}^{n_{slip}} \dot{\gamma}^{(s)}\left(\bar{\boldsymbol{b}}^{(s)} \otimes \bar{\boldsymbol{n}}^{(s)}\right)_{\text{sym}} \\ \left(\bar{\boldsymbol{b}}^{(s)} \otimes \bar{\boldsymbol{n}}^{(s)}\right)_{\text{sym}} &= \frac{1}{2}\left(\bar{\boldsymbol{b}}^{(s)} \otimes \bar{\boldsymbol{n}}^{(s)} + \bar{\boldsymbol{n}}^{(s)} \otimes \bar{\boldsymbol{b}}^{(s)}\right) \end{aligned} \tag{2.12}$$

$$\begin{aligned} \bar{\boldsymbol{W}}^{\boldsymbol{p}} &= \sum_{s=1}^{n_{slip}} \dot{\gamma}^{(s)}\left(\bar{\boldsymbol{b}}^{(s)} \otimes \bar{\boldsymbol{n}}^{(s)}\right)_{\text{asym}} \\ \left(\bar{\boldsymbol{b}}^{(s)} \otimes \bar{\boldsymbol{n}}^{(s)}\right)_{\text{asym}} &= \frac{1}{2}\left(\bar{\boldsymbol{b}}^{(s)} \otimes \bar{\boldsymbol{n}}^{(s)} - \bar{\boldsymbol{n}}^{(s)} \otimes \bar{\boldsymbol{b}}^{(s)}\right) \end{aligned} \tag{2.13}$$

Considering eq. (2.9), under the hypothesis of small elastic strains, it is possible to introduce the relationship: $\boldsymbol{C}\,\dot{\boldsymbol{\xi}} = \dot{\boldsymbol{\sigma}}$, with $\dot{\boldsymbol{\sigma}}$ as the Cauchy stress rate and $\boldsymbol{C}$ as the

elastic stiffness tensor. For FCC and BCC crystals the elastic anisotropic stiffness matrix can be written with cubic symmetry [76]. The constitutive law for such a material can be characterized by 3 material constants:

$$[\sigma] = \begin{bmatrix} C_{11} & C_{12} & C_{12} & 0 & 0 & 0 \\ C_{12} & C_{11} & C_{12} & 0 & 0 & 0 \\ C_{12} & C_{12} & C_{11} & 0 & 0 & 0 \\ 0 & 0 & 0 & C_{44} & 0 & 0 \\ 0 & 0 & 0 & 0 & C_{44} & 0 \\ 0 & 0 & 0 & 0 & 0 & C_{44} \end{bmatrix} [\epsilon]$$

$$C_{11} = \frac{E\,(1-\nu)}{(1-\nu-2\nu^2)} \qquad C_{12} = \frac{E\nu}{(1-\nu-2\nu^2)} \qquad C_{44} = \mu \tag{2.14}$$

Young's modulus (E), Poisson's ratio (ν) and the shear modulus (μ).

Considering the definition $\boldsymbol{C}\,\dot{\boldsymbol{\xi}} = \dot{\boldsymbol{\sigma}}$, Eq. (2.9) can be modified as:

$$\boldsymbol{C} : \boldsymbol{D} = \dot{\boldsymbol{\sigma}} + \boldsymbol{\sigma}\dot{\boldsymbol{R}}^{\boldsymbol{e}}\boldsymbol{R}^{\boldsymbol{e}^T} - \dot{\boldsymbol{R}}^{\boldsymbol{e}}\boldsymbol{R}^{\boldsymbol{e}^T}\boldsymbol{\sigma} + \boldsymbol{C} : \left(\boldsymbol{R}^{\boldsymbol{e}}\bar{\boldsymbol{D}}^{\boldsymbol{p}}\boldsymbol{R}^{\boldsymbol{e}^T}\right) + \boldsymbol{\sigma}\boldsymbol{R}^{\boldsymbol{e}}\bar{\boldsymbol{W}}^{\boldsymbol{p}}\boldsymbol{R}^{\boldsymbol{e}^T} - \boldsymbol{R}^{\boldsymbol{e}}\bar{\boldsymbol{W}}^{\boldsymbol{p}}\boldsymbol{R}^{\boldsymbol{e}^T}\boldsymbol{\sigma} \tag{2.15}$$

and from eq. (2.15) can be derived the Green-Naghdi objective stress rate [77]:

$$\mathring{\boldsymbol{\sigma}} = \dot{\boldsymbol{\sigma}} + \boldsymbol{\sigma}\dot{\boldsymbol{R}}^{\boldsymbol{e}}\boldsymbol{R}^{\boldsymbol{e}^T} - \dot{\boldsymbol{R}}^{\boldsymbol{e}}\boldsymbol{R}^{\boldsymbol{e}^T}\boldsymbol{\sigma} = \boldsymbol{C} : \left(\boldsymbol{D} - \boldsymbol{R}^{\boldsymbol{e}}\bar{\boldsymbol{D}}^{\boldsymbol{p}}\boldsymbol{R}^{\boldsymbol{e}^T}\right) - \boldsymbol{\sigma}\boldsymbol{R}^{\boldsymbol{e}}\bar{\boldsymbol{W}}^{\boldsymbol{p}}\boldsymbol{R}^{\boldsymbol{e}^T} + \boldsymbol{R}^{\boldsymbol{e}}\bar{\boldsymbol{W}}^{\boldsymbol{p}}\boldsymbol{R}^{\boldsymbol{e}^T}\boldsymbol{\sigma} \tag{2.16}$$

The CP finite element code implemented in Warp3D integrate the Green-Naghdi strain rate to incorporate finite strains and rotations. In the intermediate coordinate system eq. (2.16) can be written as:

$$\dot{\boldsymbol{t}} = \boldsymbol{C_0}\left(\boldsymbol{D} - \bar{\boldsymbol{D}}^{\boldsymbol{p}}\right) + \boldsymbol{R}^{\boldsymbol{e}}\bar{\boldsymbol{W}}^{\boldsymbol{p}}\boldsymbol{R}^{\boldsymbol{e}^T}\boldsymbol{t} - \boldsymbol{t}\boldsymbol{R}^{\boldsymbol{e}}\bar{\boldsymbol{W}}^{\boldsymbol{p}}\boldsymbol{R}^{\boldsymbol{e}^T} \tag{2.17}$$

it integrates this rate of the unrotated Cauchy stress ($\dot{\boldsymbol{t}} = \boldsymbol{R}^{\boldsymbol{e}^T}\mathring{\boldsymbol{\sigma}}\boldsymbol{R}^{\boldsymbol{e}}$) as a function of $\boldsymbol{D}$, the unrotated rate of deformation. $\boldsymbol{C_0}$ is the anisotropic stiffness matrix for the crystal system in the reference frame.

Finally the slip rate in eq. (2.11)-(2.12)-(2.13) is taken as a power law on a reference strain rate, the resolved shear stress and slip system strength. In the considered model the slip system hardening is isotropic; all slip systems have the same strength. The relation for the slip rate is:

$$\dot{\gamma}^{(s)} = \frac{\dot{\gamma}^0}{\tilde{\tau}}\left|\frac{\tau^{(s)}}{\tilde{\tau}}\right|^{n-1}\tau^{(s)} \tag{2.18}$$

with $\dot{\gamma}^0$ as the reference slip rate, $\tilde{\tau}$ as the slip system strength and $\tau^{(s)}$ as the resolved shear stress on the slip system s. In eq. (2.18) a relationship for the slip system strength

is still missing. A constitutive model to describe it has to be defined. The model used to describe the material hardening is a physically based one; it relies on dislocation density to describe plastic deformations [35].

The adopted model is the mechanical threshold stress [78] and will be illustrated in the following section.

2.2 Mechanical Threshold Stress Model

The Mechanical Threshold Stress (MTS) model is an isotropic scalar model that predicts flow stress as a function of strain rate, temperature and current state. It has been used successfully in the analysis of various materials [79–83]. The adoption of the MTS model for crystal structures that relies on slip systems hardening has its foundation in the macroscopic theory of work hardening presented in [84]: since the dislocation motion is governed by shear stresses, the MTS model will be written in terms of "τ" instead of the usual "σ" (the conversion between the Kirchhoff stress and the Cauchy one is obtained considering the Jacobian: $\boldsymbol{\tau} = \boldsymbol{J\sigma}$ [85]).

As anticipated in section 1.3, this model relies on the study of Mecking and Kocks [39] and is a physically based constitutive model, focusing on dislocation motion as the main reason for plastic deformation. In this context, the work done by the resolved shear stress on some increment of slip corresponds to the energy that the dislocations require to overcome energy barriers, represented by obstacles that opposes their motion. Some example of obstacles can be: grain boundaries, solute atoms, interphases and other dislocations. Associated with their motion, dislocation have kinetic energy (which can be related to the strain rate) and thermal energy (which can be related to the material temperature): both those energy may help the dislocation to overcome the opposing obstacles.

The MTS model starts from these thermodynamic consideration and brings to an expression for the flow shear along a slip system. The mechanical threshold strength is defined as the flow shear stress at $0\,K$ and is separated in an athermal component $\hat{\tau}_a$ and thermal components $\tilde{\tau}_i$:

$$\tilde{\tau}\left(T, \dot{\epsilon}_p\right) = \hat{\tau}_a + \sum_{i=1}^{m_i} \tilde{\tau}_i \tag{2.19}$$

$\hat{\tau}_a$ characterizes the rate-independent interaction with thermal barriers (it is a constant); $\tilde{\tau}_i$ are the i-th thermal components of the MTS model which characterize the interaction of dislocations with obstacles where strain rate and thermal activation assist to overcome the obstacles [43] (it is a variable depending on internal constants); $i = 1 : m_i$ identifies the number of thermal components to be used for the model. The flow stress

for all the slip systems of a single crystal is expressed as:

$$\tilde{\tau}\left(T,\dot{\epsilon}_p\right) \;=\; \hat{\tau}_a \;+\; \frac{\mu\left(T\right)}{\mu_0}\sum_{i=1}^{m_i} S_i\left(T,\dot{\epsilon}_p\right)\,\hat{\tau}_i \tag{2.20}$$

where S_i are scale factors for the i-th component, $\hat{\tau}_i$ are constants that defines the saturation strength of the i-th component and μ/μ_0 accounts for the temperature dependent elastic properties of the material:

$$\mu\left(T\right) \;=\; \mu_0 \;-\; \frac{D_0}{\exp\left(\frac{T_0}{T}\right)-1} \tag{2.21}$$

μ_0 is a reference value for the shear modulus and T_0 and D_0 are empirical constants.

Kocks, Argon and Ashby [84] express the scale factor in terms of an energy barrier to be overcome by a combination of energy associated with the applied stress and the free activation energy associated with slip thermodynamics and kinetics. In thermally activated glide, interactions with short obstacles are described using the energy form given in [43], as an Arrhenius type form:

$$\dot{\epsilon}_p \;=\; \dot{\epsilon}_0 \exp\left(\frac{-\Delta G_0}{kT}\right) \tag{2.22}$$

where k is the Boltzman constant; T is the temperature; ΔG_0 is the Gibbs free activation energy; $\dot{\epsilon}_0$ is a reference strain rate assumed independent by the temperature and the stress state [86]; $\dot{\epsilon}_p$ can be evaluated as $\dot{\epsilon}_p \;=\; \sqrt{\frac{2}{3}D:D}$. Eq. (2.22) can be rearranged to obtain an expression for ΔG_0 as:

$$\Delta G_0 \;=\; kT\ln\left(\frac{\dot{\epsilon}_0}{\dot{\epsilon}_p}\right) \tag{2.23}$$

A functional form, suggested in [84], to relate ΔG_0 with τ relies on some assumption about the shape of the energy barriers opposing the dislocation motion. Fig. 2.3-a shows a generic profile of the energy barrier, divided in the total work area, generated by the applied stress ($H_W \;=\; b\tilde{\tau}\delta y$ where $\tilde{\tau}$ is the flow shear and δy is a small displacement), and the total free energy area provided by thermal activation. The description of the shape of the i-th energy profile can be reduced to [84]:

$$\Delta G_{0,i} \;=\; g_{0,i}\mu b^3\left\{1-\left(\frac{\tilde{\tau}_i}{\hat{\tau}_i}\right)^{p_i}\right\}^{q_i} \tag{2.24}$$

where $g_{0,i}$ is the normalized activation energy; p_i and q_i are statistical constants which characterize the shape of the i-th energy obstacle profile (see Fig. 2.3-b); $\hat{\tau}_i$ is a scalar representing the strength of the i-th component of eq. (2.20). Rearranging eq. (2.22) and eq. (2.24) it is possible to obtain:

$$\tilde{\tau}_i \;=\; S_i\left(T,\dot{\epsilon}_p\right)\,\hat{\tau}_i \;=\; \left\{1-\left[\frac{k\,T}{g_{0,i}\,\mu\,b^3}\ln\left(\frac{\dot{\epsilon}_{0,i}}{\dot{\epsilon}_p}\right)\right]^{\frac{1}{q_i}}\right\}^{\frac{1}{p_i}}\hat{\tau}_i \tag{2.25}$$

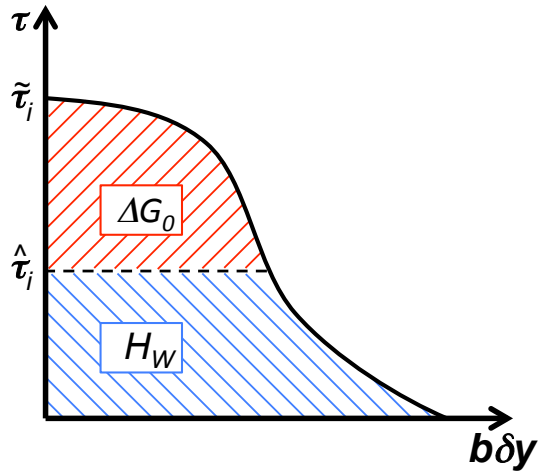

(a)

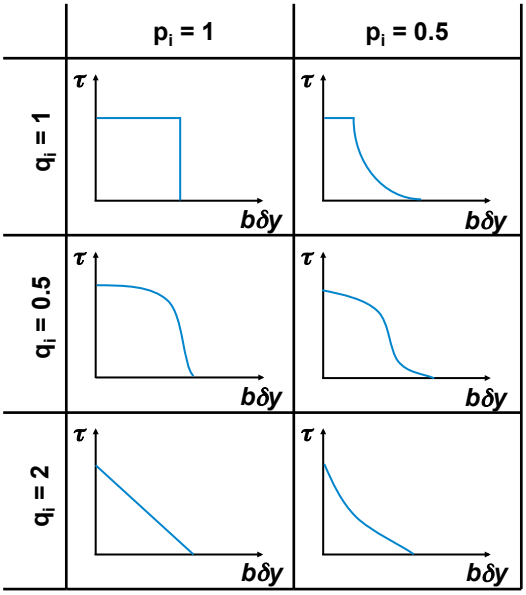

(b)

Figure 2.3: *a) Generic energy profile showing contributions of work and free (thermal activation) energy [84];b) Short range profile [84] described by an equation of the type* $\Delta G_{0,i} \propto (1 - (\tilde{\tau}^*/\hat{\tau}^*)^{p_i})^{q_i}$*, similarly to eq.* (2.24)*.*

this give a final definition for the i-th scale factor S_i:

$$S_i\left(T, \dot{\epsilon}_p\right) = \left\{1 - \left[\frac{k\,T}{g_{0,i}\,\mu\,b^3} \ln\left(\frac{\dot{\epsilon}_{0,i}}{\dot{\epsilon}_p}\right)\right]^{\frac{1}{q_i}}\right\}^{\frac{1}{p_i}} \tag{2.26}$$

To complete the work hardening model of eq. (2.20), two terms of the type shown in eq. (2.25) are considered, $m_i = 2$, one representing all intrinsic barrier to dislocation motion and one all work hardening. This general form reproduces the behaviour shown

in Fig. 2.4, considering the initial strength to dislocation motion (yielding) and the subsequent increasing due to dislocation hardening [78]. The slip system strength that

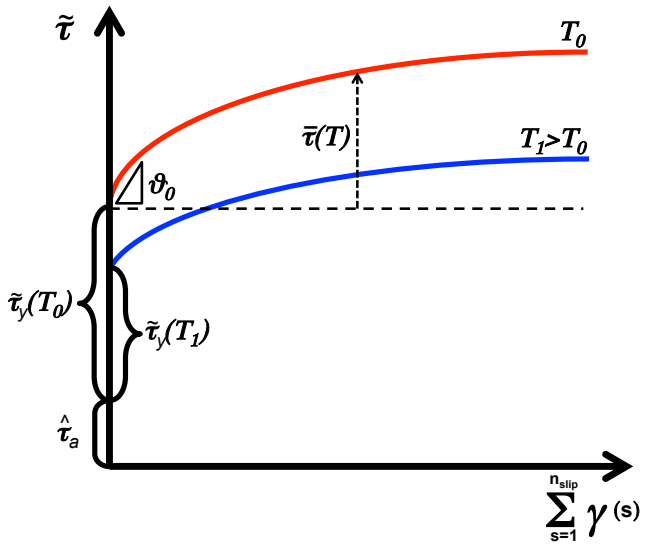

Figure 2.4: *Schematic of the MTS hardening model: graphical definition of the major parameters describing it.*

eq. (2.18) requires (deriving from eq. (2.20)) has the following expression:

$$\tilde{\tau}\left(T,\dot{\epsilon}_p\right) \;=\; \hat{\tau}_a \;+\; \tilde{\tau}_y\left(T,\dot{\epsilon}_p\right)\frac{\mu}{\mu_0} \;+\; \bar{\tau}\left(\tilde{\tau}_v\left(T,\dot{\epsilon}_p\right)\right)\frac{\mu}{\mu_0} \tag{2.27}$$

$\bar{\tau}$ is the term that accounts for work hardening: a process that sees a balance between dislocations generation and *recovery*, a mechanism where stresses are high enough to assist dislocations pass the obstacles. Considering [84, 87] the law for dislocation density over shear strain for the s-th slip system can be expressed as:

$$\frac{\partial \rho_f^{(s)}}{\partial \gamma^{(s)}} \;=\; k_1\sqrt{\rho_f^{(s)}} - k_2\left(T,\dot{\epsilon}_p\right)\rho_f^{(s)} \tag{2.28}$$

k_1 keeps track of dislocation generation and k_2 of the recovery as a thermal activation process. Taking into account the Bailey-Hirsh [88] relation which governs the flow stress in materials:

$$\bar{\tau}^{(s)} \;=\; \mu\eta b\sqrt{\rho_f^{(s)}} \tag{2.29}$$

where μ is the shear modulus, b is the magnitude of the Burgers vector and η a dislocation interaction constant. Considering the evolution of $\bar{\tau}^{(s)}$ with the dislocation slip, eq. (2.29) becomes:

$$\frac{\partial \bar{\tau}^{(s)}}{\partial \gamma^{(s)}} \;=\; \eta\mu b\frac{\partial}{\partial \gamma^{(s)}}\left(\sqrt{\rho_f^{(s)}}\right) \;=\; \frac{\eta\mu b}{2\sqrt{\rho_f^{(s)}}}\frac{\partial \rho_f^{(s)}}{\partial \gamma^{(s)}} \tag{2.30}$$

Combining eq. (2.30) with eq. (2.28) and eq. (2.29), the result is:

$$\frac{\partial \bar{\tau}^{(s)}}{\partial \gamma^{(s)}} \;=\; k_1 \frac{\eta \mu b}{2} - k_2 \frac{\bar{\tau}^{(s)}}{2} \tag{2.31}$$

A definition for k_1 and k_2 makes them function of ϑ_0 (Fig. 2.4), which characterizes the initial slope of the stress-plastic strain curve [8]:

$$k_1 \;=\; \frac{2\vartheta_0}{\eta \mu b} \qquad k_2 \;=\; \frac{2\vartheta_0}{\tilde{\tau}_v} \tag{2.32}$$

$\tilde{\tau}_v$ is defined as the temperature and rate dependent work hardening saturation strength. Substituting eq. (2.32) in eq. (2.33) the following linear Voce law is derived:

$$\frac{\bar{\tau}^{(s)}}{\gamma^{(s)}} \;=\; \vartheta_0 \left(1 - \frac{\bar{\tau}}{\tilde{\tau}_v}\right) \tag{2.33}$$

Eq. (2.33) then can be written as a differential of time over all the slip systems and gets the formulation:

$$\dot{\bar{\tau}} \;=\; \vartheta_0 \left[1 \;-\; \frac{\bar{\tau}}{\tilde{\tau}_v}\right] \sum_{s=1}^{n_{slip}} \dot{\gamma}^{(s)} \tag{2.34}$$

$\sum_{s=1}^{n_{slip}} \dot{\gamma}^{(s)}$ represents the accumulated plastic strain rate. Following those definition, the terms that follows the Arrhenius type formulation (eq. (2.25)) are:

$$\tilde{\tau}_y \;=\; S_y\left(T, \dot{\epsilon}_p\right) \hat{\tau}_y \quad \tilde{\tau}_v \;=\; S_v\left(T, \dot{\epsilon}_p\right) \hat{\tau}_v$$

Eq. (2.34) can be expanded even further accounting for geometrically necessary dislocations [89, 90] and evaluate the Nye tensor (α) [91] and the linear dislocation density along a slip plane ($\lambda^{(s)}$):

$$\boldsymbol{\alpha} \;=\; -\nabla \times \boldsymbol{F}^{e^{-1}} \qquad \lambda^{(s)} \;=\; \sqrt{\left(\boldsymbol{\alpha}\bar{\boldsymbol{n}}^{(s)}\right) : \left(\boldsymbol{\alpha}\bar{\boldsymbol{n}}^{(s)}\right)} \tag{2.35}$$

Defining a term which accounts for this geometric dislocations [89]:

$$\tau_\lambda^{(s)} \;=\; \frac{k_0}{k_1} \eta \, \mu \, \lambda^{(s)} \tag{2.36}$$

where k_0 is a parameter characterizing stage IV of the work hardening [92]. Including this term in eq. (2.34), it can be modified in the following formulation:

$$\dot{\bar{\tau}} \;=\; \sum_{s=1}^{n_{slip}} \vartheta_0 \left[1 \;-\; \frac{\bar{\tau}}{\tilde{\tau}_v} \;+\; \frac{\tau_\lambda^{(s)}}{\bar{\tau}}\right] \dot{\gamma}^{(s)} \tag{2.37}$$

$\tau_\lambda^{(s)}$ influences the work hardening plastic deformation (for low deformation its value is very small, so it practically affects only the final stage of the work hardening which has a nearly constant hardening slope).

2.3 Conclusions

After the analysis of the model, the parameters which have to be identified to simulate the material behaviour are summarized in Table 2.1.

Table 2.1: *Material parameters required to completely define the material in CPFE simulations.*

Property	Description
E	Young's modulus
ν	Poisson's ratio
μ_0	Shear modulus
b	Burgers Vector
k	Boltzman constant
n	exponent of the slip rate
$\hat{\tau_a}$	Athermal slip resistance
$\hat{\tau_y}$	MTS strength for intrinsic barrier (yield)
$g_{0,y}$	Normalized activation energy for intrinsic barriers
q_y	Shape coefficient for intrinsic barriers
p_y	Shape coefficient for intrinsic barriers
$\epsilon_{0,y}$	Strain rate sensitivity for intrinsic barriers
$\hat{\tau_v}$	MTS strength for work hardening
$g_{0,v}$	Normalized activation energy for work hardening
q_v	Shape coefficient for work hardening
p_v	Shape coefficient for work hardening
$\epsilon_{0,v}$	Strain rate sensitivity for work hardening
ϑ_0	Initial hardening slope
k_0	Geometric hardening parameter

CHAPTER 3

Tensile Mechanical Behaviour

This chapter gives an estimation of the crystal plasticity model parameters for Haynes 230. First a brief description of the experimental tests carried out is provided, with reference to the study conducted by Pataky et al. [18] for a high temperature tensile test. Then, starting from room temperature tensile tests conducted on single crystals, the parameters for the CP model were estimated. Finally these parameters were accurately updated to simulate an high temperature tensile test conducted on a polycrystalline specimen [93].

3.1 Experiments

The experimental procedure has its foundation in the DIC technique. It was adopted for measuring global and local displacements for both single crystal and polycrystalline specimen.

Single Crystal Tests

The single crystal specimens were grown using the Bridgman technique [94] and their orientations were verified using EBSD: the three tested specimens were oriented with the [001], [011], [111] directions along the loading direction. Dog-bone tension speci-

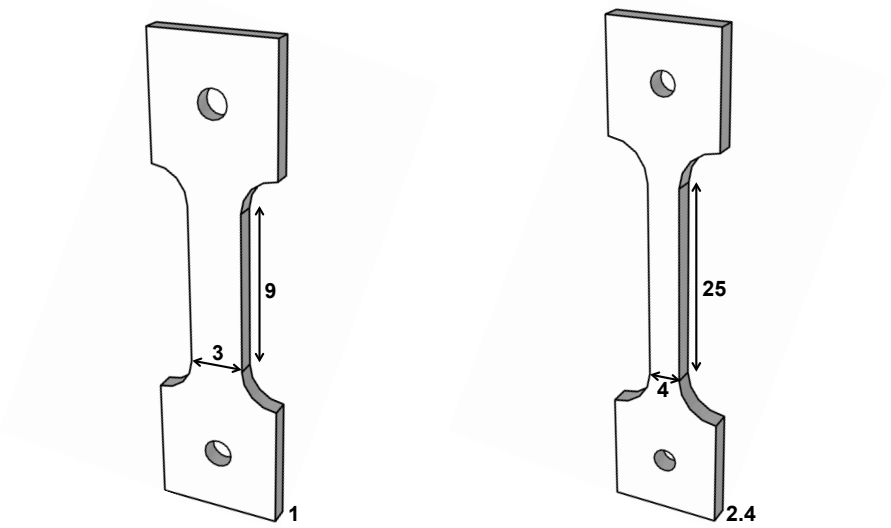

(a) (b)

Figure 3.1: *Schematics of the single crystal specimens (a) and the polycrystalline one (b).*

mens (Fig. 3.1-a), designed for single crystal tests, were electrical discharge machined (EDM) with a parallel length of 9 mm long, a width of 3 mm, and a thickness of approximately 1 mm. The specimens were mechanically polished to a mirror finish, and then the speckle pattern was airbrushed onto each specimen using black paint. Monotonic tension experiments were performed in a servo-hydraulic load frame capturing deformation images *in-situ* at a rate of 15 fps until failure. DIC images were captured with a field of view of 2.9 mm by 2.6 mm with a resolution of 2.2 μm/pixel. A spatial resolution of 178 μm was used for determining the strain field as defined in [95].

The results in terms of σ-ϵ curves for the three oriented specimens are summarized in Fig. 3.2, in comparison with the monotonic curves for a room and an high temperature polycrystalline specimens.

Polycrystalline Tests

The polycrystalline specimen was wide enough to accommodate induction heating coils as the experiment was performed at 700^{o}C. The specimen dimensions were 25 mm parallel length, width of 4 mm and thickness of 2.38 mm (see Fig. 3.1-b). EBSD was performed on an area of 0.5 mm by 2 mm before the experiment. DIC images were captured *ex-situ* with an optical microscope to improve spatial resolution. Due to this, the experiment is an interrupted monotonic tension experiment. Full detail can be found in [18]. The results in terms of σ-ϵ are reported in Fig. 3.3-a, while Fig.s 3.3-b-c-d show the DIC results associated with the unloading condition they belong.

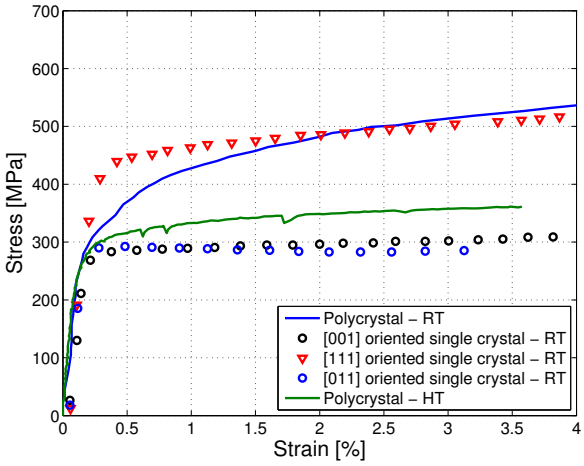

Figure 3.2: *Summary of the tensile tests curve on Haynes 230 specimens, single crystal and polycrystalline experiments.*

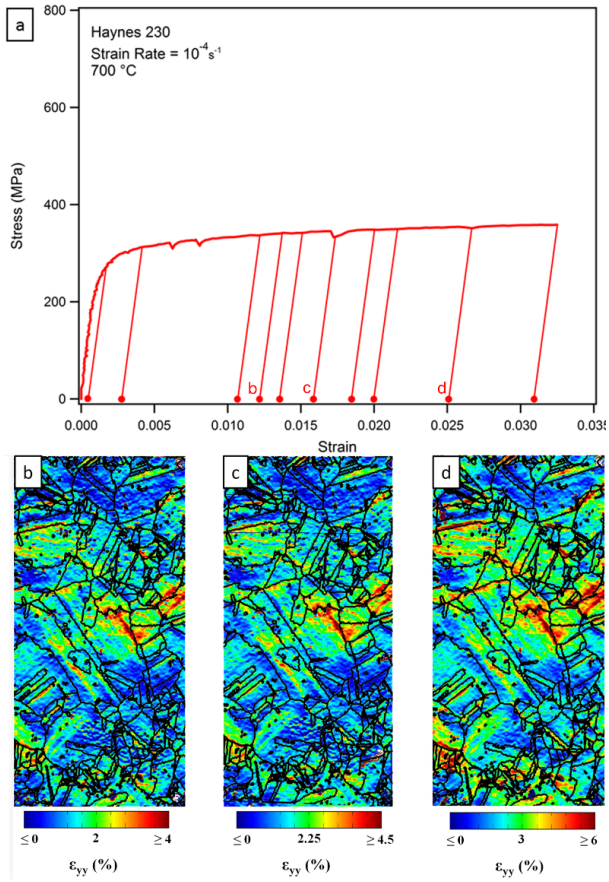

Figure 3.3: *Experimental tensile test at 700°C [18] with focus on the tensile curve (a) and the three unloadings where the DIC was performed: (a) 1.22%, (b) 1.59%, (c) 2.51%.*

3.2 Modeling of Single Crystal Tensile Tests

To perform the FE simulations, it is necessary for the material parameters to be identified; the analysis of single crystal experiments allowed an iterative optimization. After determining the constants it was possible to study and reproduce one of the single crystal tests local behaviour.

3.2.1 Crystal Plasticity Model - Identification of parameters

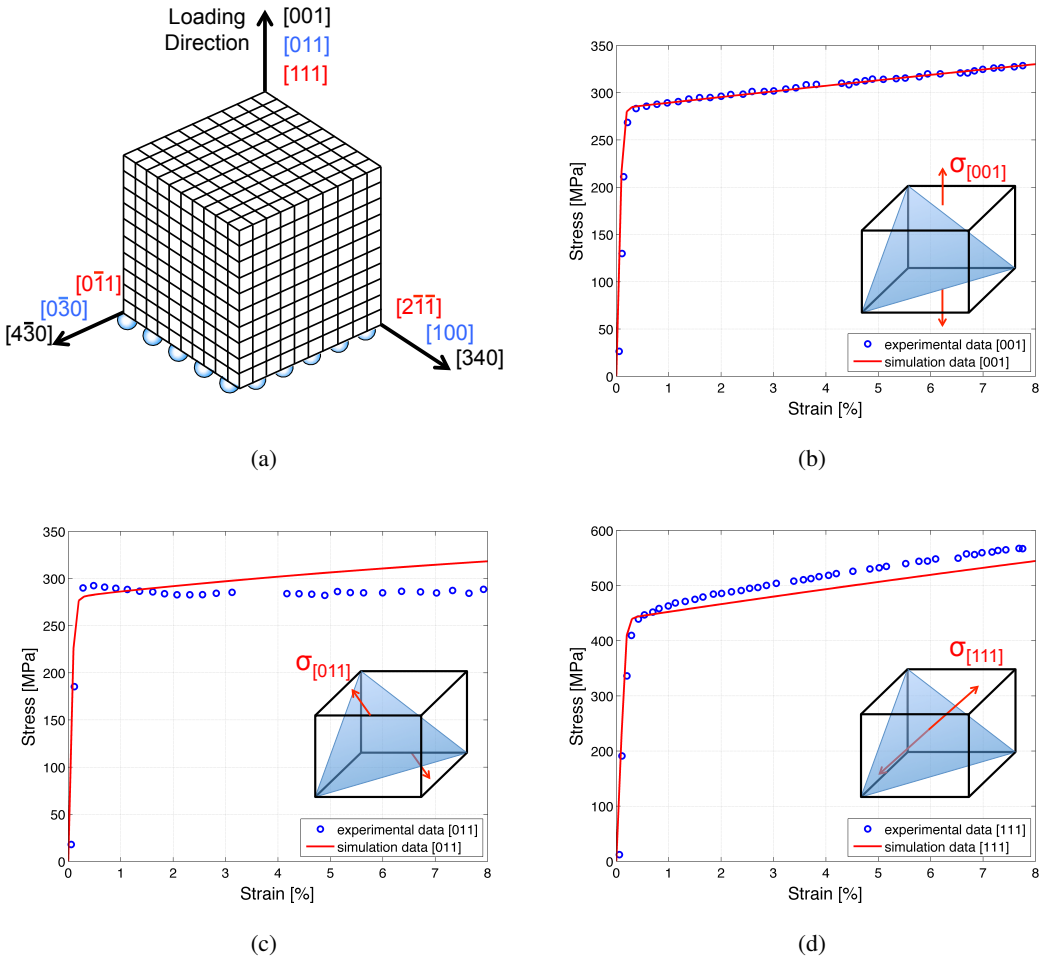

Figure 3.4: *Single Crystal models setup and results: (a) Cubic RVE for single crystal tensile tests analyses with details about the crystal coordinate systems. Comparison between simulations and experiments for specimens with loading direction along: (b) [001]; (c) [011]; (d) [111].*

To simulate the single crystal experimental stress-strain curves, a cubic representative volume was adopted with load orientations along the [001], [011] and [111] directions. The simulations were carried out considering a cubic geometry of 1x1x1 mm and

1000 hexahedral linear elements (see Fig. 3.4). Each element was associated with the Euler angles corresponding to the specimen's orientation. In order to reproduce the displacement controlled tensile test, the load was applied as a displacement along the face perpendicular to the desired crystal direction, while the opposing face was displacement constrained along the load direction. This modeling which considers reference volume elements (RVEs) had the main purpose to evaluate the overall behaviour in terms of tensile curve for the three crystals. The comparison between the stress-strain curves of the three simulations and the experiments, Fig. 3.4(b-c-d), showed a good agreement, especially on the [001] and [111] oriented specimens. Several model parameters were identified following the results of those simulations (Table 3.1); others were taken according to literature [79–81].

Table 3.1: *Material parameters for crystal plasticity simulation of Haynes 230 single crystals.*

Property	Description	Fitting/Literature	Value
E	Young's modulus	Fitted	218 GPa
ν	Poisson's ratio	Fitted	0.33
μ_0	Shear modulus	Fitted	89.5 GPa
b	Burgers Vector	Literature [80]	$3.5\,E-7$ mm
$\hat{\tau_a}$	Athermal slip resistance	Literature [8]	0 MPa
$\hat{\tau_y}$	MTS strength for intrinsic barrier (yield)	Fitted	130 MPa
$g_{0,y}$	Normalized activation energy for intrinsic barriers	Literature [80]	0.37
q_y	Shape coefficient for intrinsic barriers	Literature [78]	1.5
p_y	Shape coefficient for intrinsic barriers	Literature [78]	1.5
$\epsilon_{0,y}$	Strain rate sensitivity for intrinsic barriers	Literature [79]	$1\,E9$ s^{-1}
$\hat{\tau_v}$	MTS strength for work hardening	Fitted	80 MPa
$g_{0,v}$	Normalized activation energy for work hardening	Literature [80]	1.6
q_v	Shape coefficient for work hardening	Literature [78]	0.667
p_v	Shape coefficient for work hardening	Literature [78]	1.2
$\epsilon_{0,v}$	Strain rate sensitivity for work hardening	Literature [79]	$1\,E7$ s^{-1}
ϑ_0	Initial hardening slope	Fitted	110 MPa
k_0	Geometric hardening parameter	Fitted	1

3.2.2 Strain Localization Analysis In [011] Oriented Specimen

In [011] oriented specimen high strain localization bands were detected by DIC. Hence, a second model was developed with the sole purpose to reproduce the local behaviour captured in the [011] test: accumulation along 39^o inclined bands, Fig. 3.5. A single crystal plate was modeled, as shown in Fig. 3.5-a: the geometry consists of a plate (3x3x1 mm), corresponding to the central section of the dog-bone specimen. It was

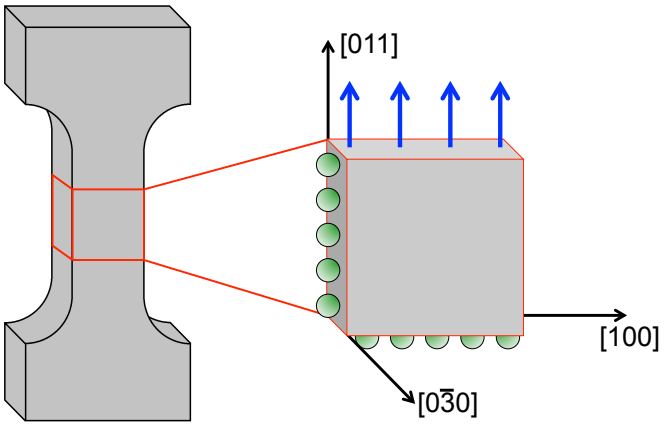

(a)

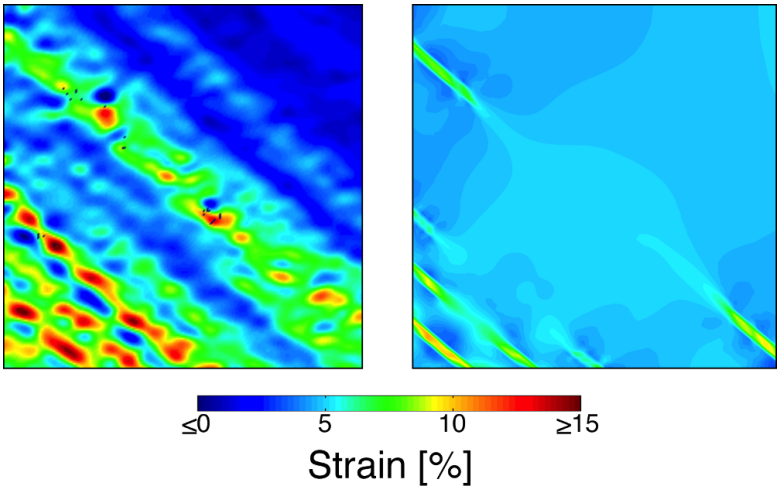

(b)

Figure 3.5: *[011] single crystal oriented specimen: (a) simulation geometry scheme; (b) results in terms of strain localization, (b) left is the experiment and right is the simulation.*

modeled using an average element size of 40 μm. The load was applied as a displacement along the face (3x1 mm) parallel to the [011] direction, the opposing face was displacement constrained. The two localizations were compared, Fig. 3.5-b, considering the experimental overall strain where the DIC was performed, 4.9%. The model showed strain accumulation along 40.1^o direction, which is comparable with the 39^o of the experiment.

Further analyses were done with the aim to evaluate which is the effect of choosing different reference volume elements, selected from the plate, especially on the predicted tensile curve. Considering Fig. 3.6-a, which explains where different starting points for increasing RVEs were picked (the RVEs grows from a 1 element to full plate, with

volumes that goes from 7e-4 mm^3 to the full volume of the plate), it is possible to evaluate the stress-strain monotonic curve for all of the chosen volumes. The results of this analysis are shown in Fig. 3.6 where Fig. 3.6-b shows all the RVEs results. Fig. 3.6-c compare the experimental result with the upper and lower bounds obtained from the RVEs. Concluding, even considering different reference volumes elements the experimental curve is still not completely matched.

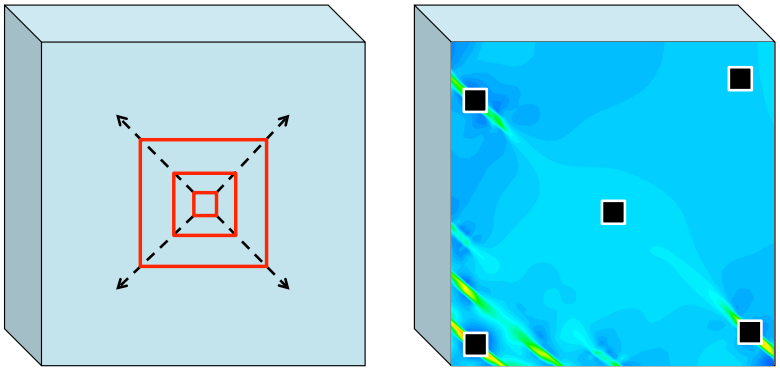

(a)

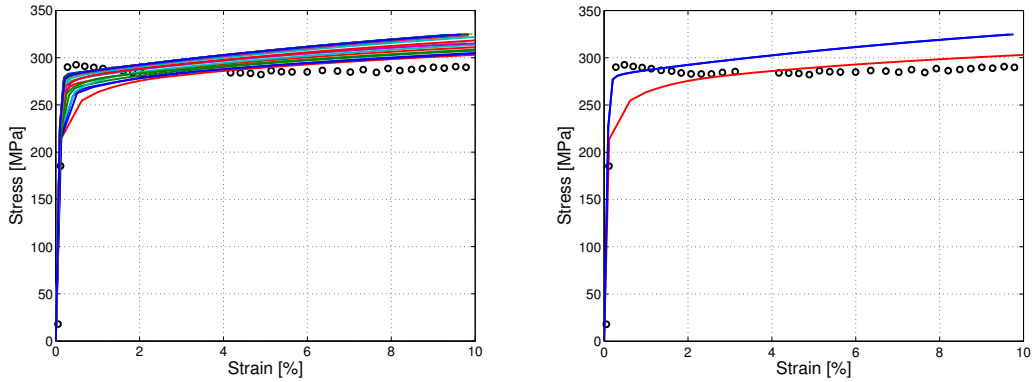

(b) (c)

Figure 3.6: *Analysis of [011] simulation tensile curve varying the RVE on the modeled plate: (a) RVEs and location of the starting points on the map of Fig. 3.5; (b) experimental results in comparison with the curve from all the RVEs; (c) experimental results in comparison with the upper and lower bounds coming from the RVEs .*

3.3 High Temperature Simulation

Having identified the parameters of the crystal plasticity model by analyzing the single crystal results, it was possible to analyze a polycrystalline specimen. The simulation emulated a specimen that undergoes a tensile test at 700^{o}C and with the strain field measured via high resolution *ex-situ* DIC [18]. To account for the test at high temperature some parameters were tuned according to the experimental stress-strain curve, the modified parameters are recorded in Tab. 3.2.

Table 3.2: *Material parameters for crystal plasticity simulation of Haynes 230 polycrystalline high temperature specimen.*

Property	Description	Fitting/Literature	Value
E	Young's modulus	Fitted	201 GPa
μ_0	Shear modulus	Fitted	84 GPa
$\hat{\tau_y}$	MTS strength for intrinsic barrier (yield)	Fitted	128 MPa
$\hat{\tau_v}$	MTS strength for work hardening	Fitted	40 MPa
ϑ_0	Initial hardening slope	Fitted	225 MPa

3.3.1 Model Definition

The geometry of the finite element model was defined by the DIC area of interest. Starting from the EBSD of the full area where the DIC was performed, Fig. 3.7, three smaller areas were extracted as shown in the picture. The choice of those three area was made according to the experimental strain localizations of Fig. 3.3.

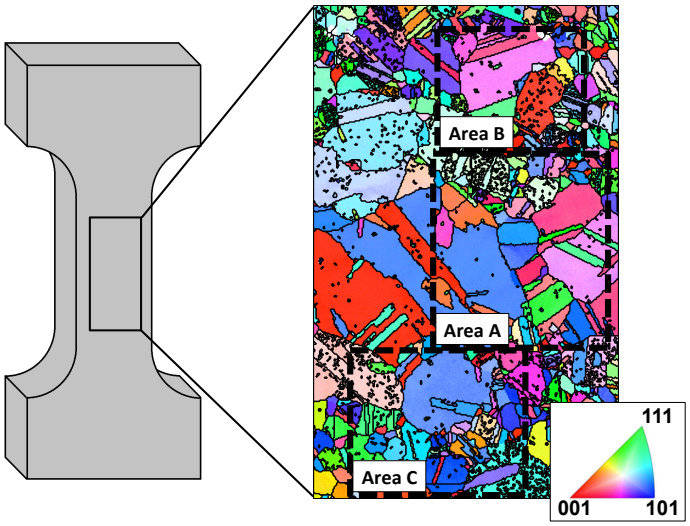

Figure 3.7: *EBSD of the whole specimen and definition of the sub-areas A, B and C.*

Then these three areas were modeled starting from the EBSD data, which provided both grains geometry and the Euler angles belonging to each grain. The extracted areas of Fig. 3.8 are compared with their FE models. The three areas dimensions are respectively, 354 μm by 291 μm (Area A), 204 μm by 229 μm (Area B) and 277 μm by 234 μm (Area C).

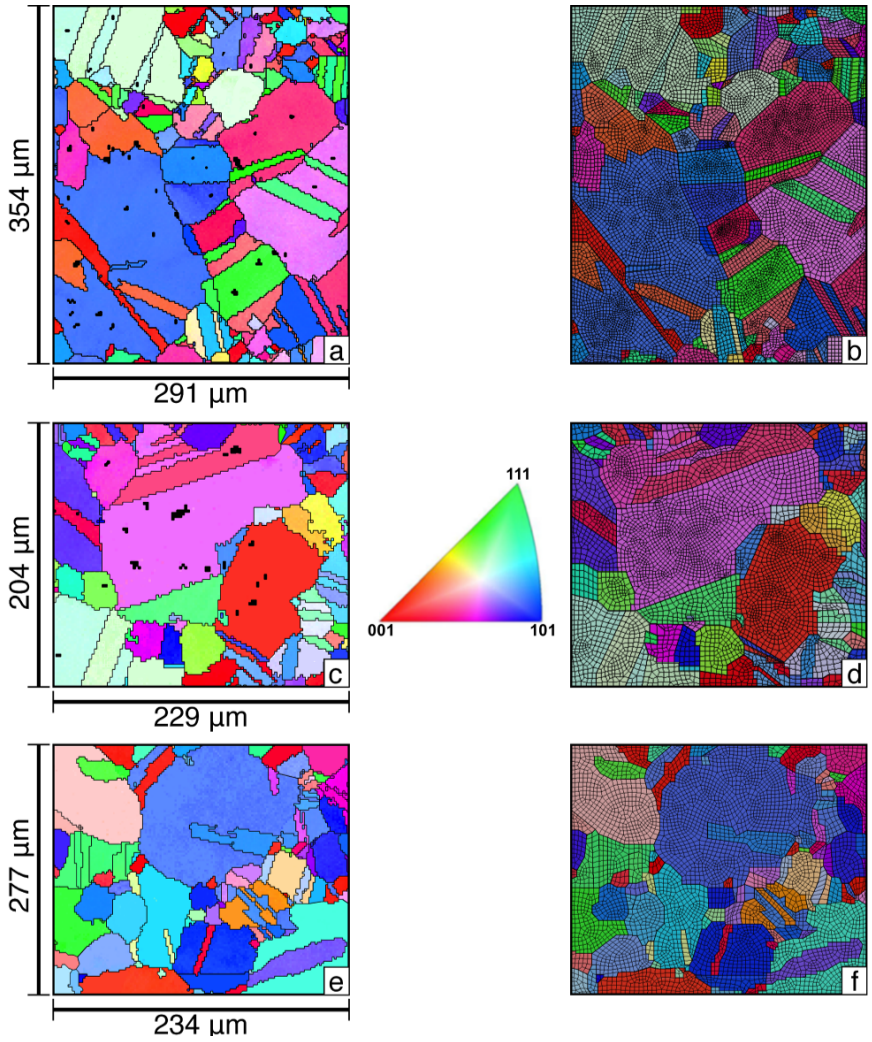

Figure 3.8: *Comparison between the sub-models EBSD and the geometry created for the FE analyses, with emphasis on their dimensions and the mesh adopted for each of them: (a) and (b) refers to area A; (c) and (d) to area B; (e) and (f) to area C.*

Each model was created with linear hexahedral elements with an average size of 3.5 μm; the three areas count respectively, 134 grains and 46000 elements (Area A), 78 grains and 24000 elements (Area B) and 108 grains and 26500 elements (Area C). The adoption of 3.5 μm elements derived from a mesh convergence evaluation: below this dimension no differences in results were detected. The models were 5 elements

thick (20 μm), thus each one can be considered in plane stress. Finally Fig. 3.9 shows a schematic of the loading and constraints (the schematization in the picture is referred to Area C, but it is the same for A and B as well): to simulate the tensile experiment, a displacement was applied to the nodes of the upper face (see the models of Fig. 3.9), while a double symmetry was applied as in the picture. The double symmetry was chosen after trying different constraint conditions, this grants a stability of the solution and there are no out of plane displacement (no shear or rotation of the whole model); it was preferred to a triple symmetry (constraining also in z direction) since the simulations brought to the same results on the free surface and in addition maintained the plane stress hypothesis of the model.

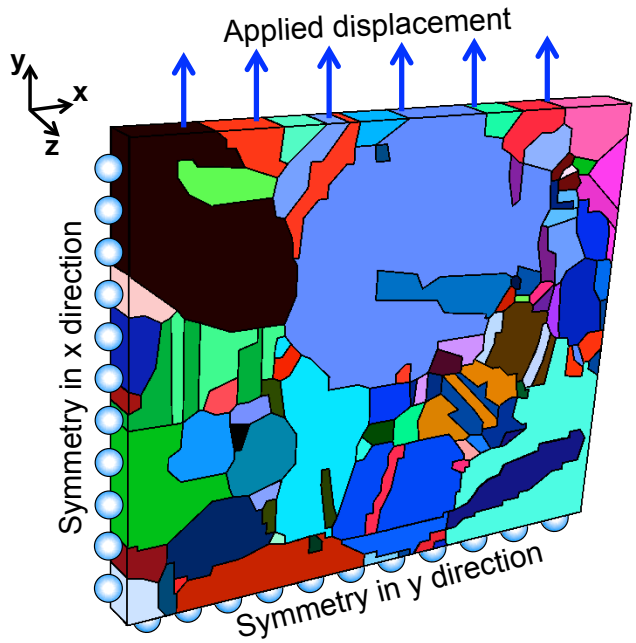

Figure 3.9: *Loading scheme for the polycrystalline specimens explained considering area C model.*

3.3.2 Comparison With Experimental Results

Following the experimental results as shown in Fig. 3.3, the simulations were carried out on the 3 areas considering the three subsequent unloadings, resulting in overall residual strains of 1.22%, 1.59% and 2.51%.

Fig. 3.10 shows a comparison between the stress strain curves from the experiment, measured with DIC, and those extracted from the models. Global strain and stresses were obtained from the models through a volume average over the elements. A good agreement is observed between the models and the experiment. This output pointed out

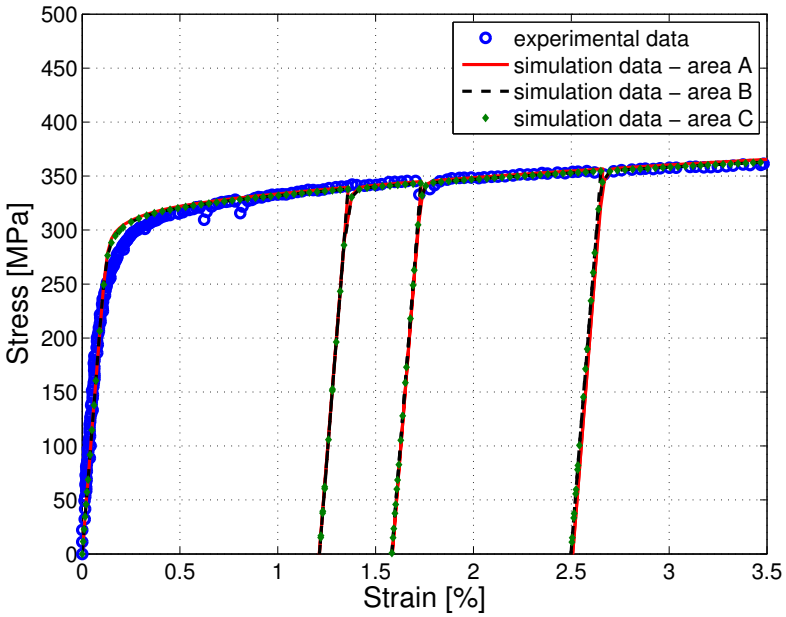

Figure 3.10: *HT polycrystalline simulation: comparison between the experimental stress-strain curve and the FE analysis of the 3 models.*

that the models, despite the difference in surfaces extensions, contained enough grains to be able to describe the experimental global behaviour. After discussing the overall results, for the following analysis only the first one (1.22%) will be considered; it was taken as a reference to compare the simulations and the results on the micro-scale level.

Fig. 3.11 shows a summary of the results after unloading, matching experiments with the models. The comparison showed where the strains localize along the grains, in both the real medium and the simulated one. This type of simulations was able to capture several grains activation and strain accumulations along bands, but many mismatches were also detected. This pointed out that this type of modeling, based only on the EBSD angles, was not able to describe all the effects that contribute to strain localization, like the presence of incongruent particles. In fact in Haynes 230 the presence of inclusions like carbides is very high like shown in [17], so the next step of the models concerned the introduction of several carbides in the polycrystalline matrices.

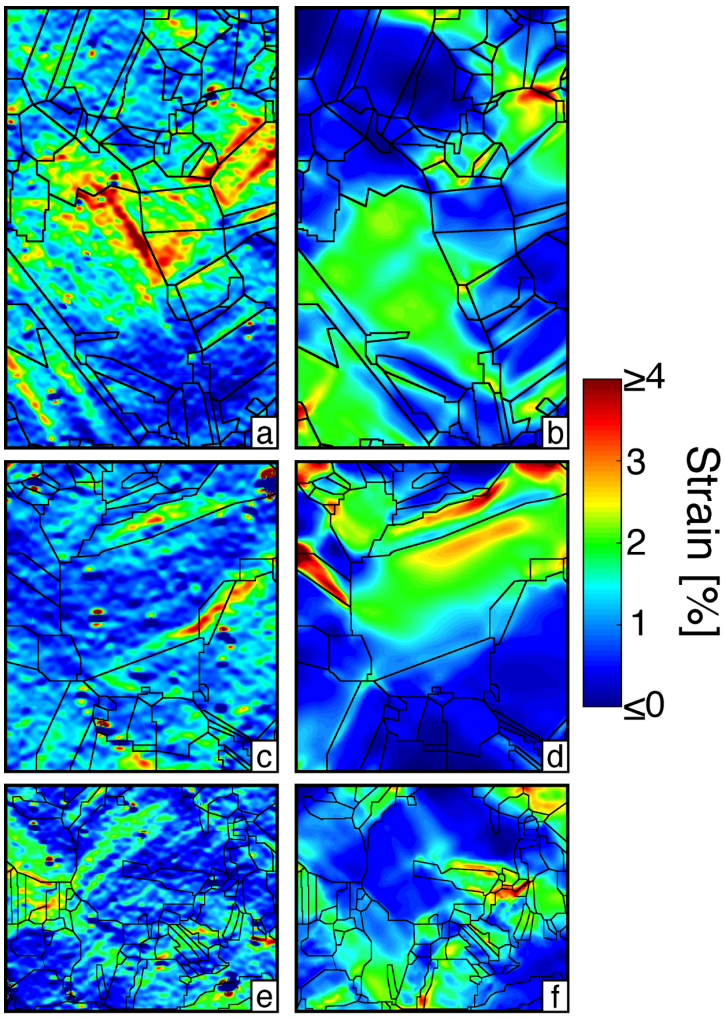

Figure 3.11: *HT polycrystalline simulation: strain localization in the three considered areas. (a), (c), (e) are DIC results and (b), (d), (f) are the simulations. Can be compared considering that: (a) and (b) refers to area A; (c) and (d) to area B; (e) and (f) to area C.*

3.3.3 Analysis Of The Effects Of Carbides

The introduction of carbides in the model of area A and B (Fig. 3.8) was done following the identification of some carbides within the cited surfaces. The dimension of the carbides to be included in the matrix was the key feature for their selection: no carbides with a dimension lower than about 1.5 μm were chosen. Fig. 3.12 shows where the carbides of the two selected areas were detected and embedded in the models. The carbides were modeled as purely elastic materials [96], with an elastic modulus much higher than the one of the crystals. The outcome of these simulations revealed that the inclusion of carbides influenced only the local answer of the material, while the stress strain curves were consistent with those showed in Fig. 3.10. The local strain intensi-

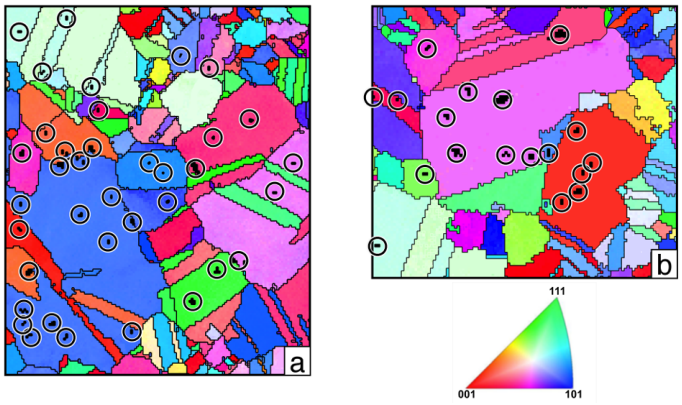

Figure 3.12: *HT polycrystalline simulation: carbides position with reference on the EBSD maps of area A (a) and B (b).*

fication, due to the carbides, reported in Fig. 3.13, enhanced the approximation of the experiment, helping to obtain a better description of the deformation that accumulates along grains and grain boundaries.

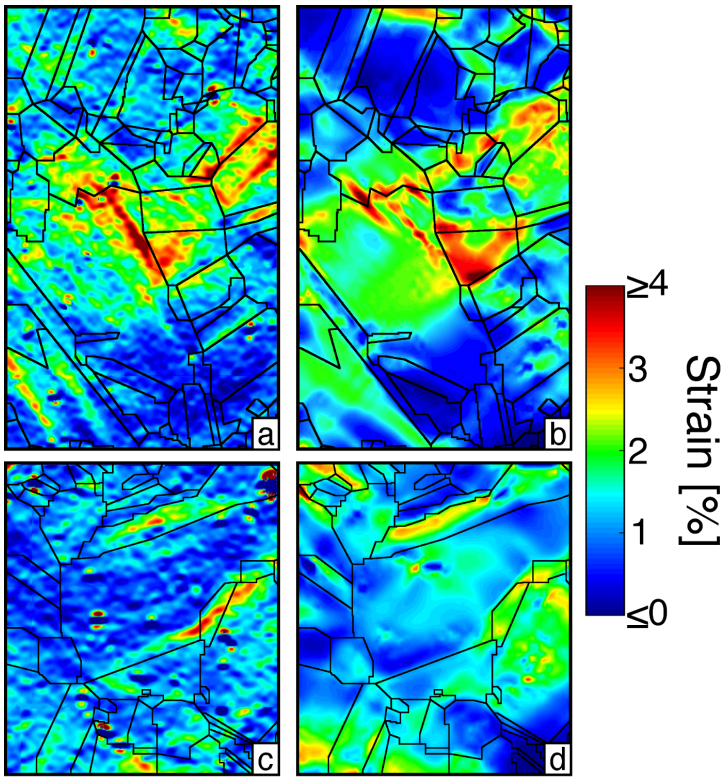

Figure 3.13: *HT polycrystalline simulation: comparison of the strain localization considering the effects of carbides on two of the selected areas: (a)-DIC and (b)-SIM refers to area A; (c)-DIC and (d)-SIM to area B.*

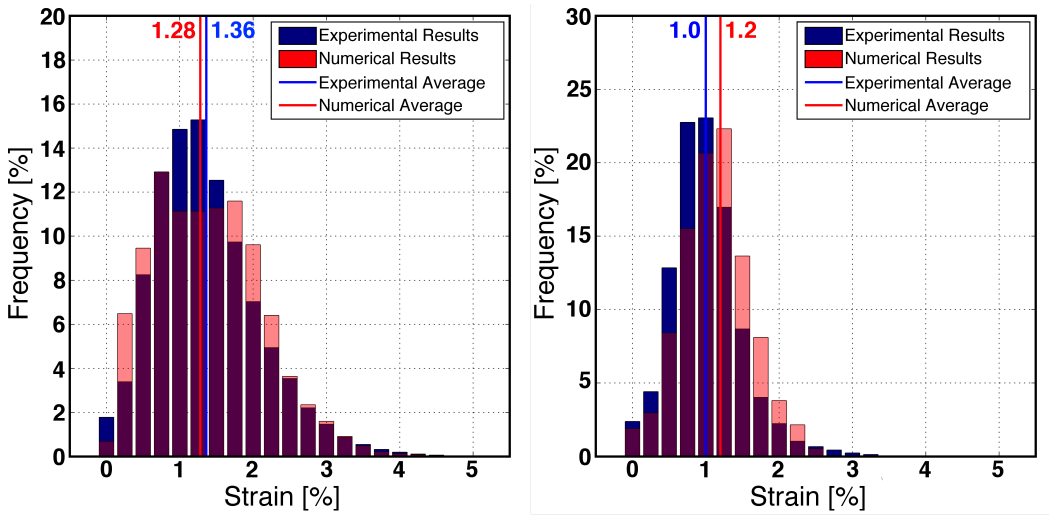

(a) (b)

Figure 3.14: *Histogram comparison between simulation and experimental strain distribution across area A and B: (a) area A; (b) area B.*

An analysis of the strain distribution, Fig. 3.14, was then made as a further comparison with the experiment through strain levels histograms. For consistency, the numbers of strain values sampled with DIC and FE models had to be the same. For area A, the DIC showed a majority of values around the average while the simulation showed a plateau. Area B simulation instead showed a trend comparable with the one coming from the experiment, despite having a difference of 0.2% in the average strain. The difference can be associated with the fact that the model was loaded to reproduce the global behaviour of the whole specimen (see Fig. 3.3 and Fig. 3.8), measured over the entire DIC area of interest, while locally the DIC on area B registered a lower mean cumulated strain.

Then, analyses were done investigating line scans across the selected surfaces. Fig. 3.15 shows, for models A and B, the comparison between 3 datasets: the experiment, the simulations without carbides and the simulation with carbides. It can be observed that the three curves, in both models, are similar in terms of trends and magnitudes. The trends were well captured with the first simulations (those without carbides), considering peaks and valleys, and improved by the introduction of carbides.

Further analyses had the objective to evaluate the stress localization close to several of the introduced carbides. Those investigations involved the identification of the slip planes were the shear stress has its maximum magnitude close to the carbide. This analysis was pursued following the scheme presented by Gall in [97,98]. Starting from the definition of all the slip systems in the reference coordinate frames (see Tab. 1.2),

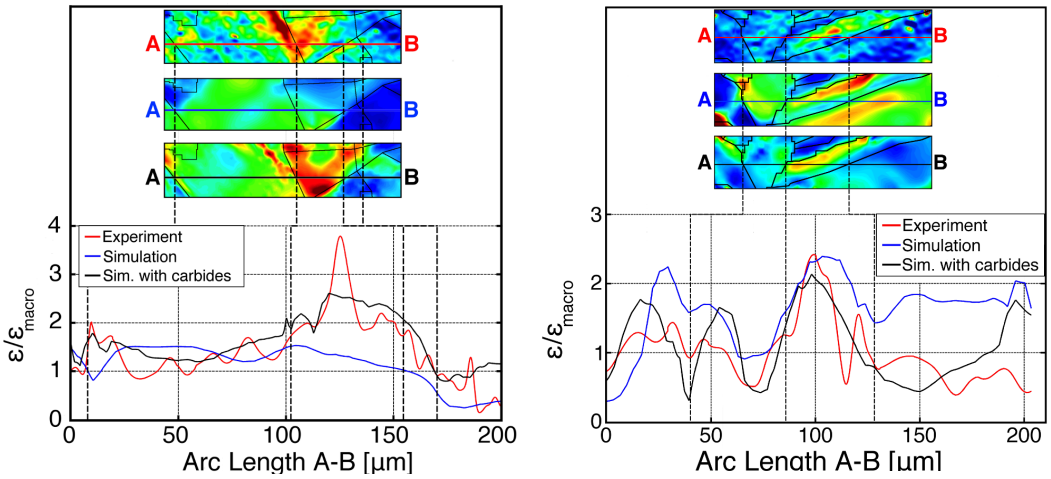

(a) (b)

Figure 3.15: *Line scans along an arc AB considering the same position on DIC, simulation without carbides and simulation with carbides: (a) area A; (b) area B.*

the rotation matrices that have to be applied to the stress tensor, to obtain it on the slip planes, could be evaluated. Considering the Euler angles (in the Kocks convention), named (e_1, e_2, e_3), the rotation matrix for the considered grain (Q_G) can be evaluated as:

$$[Q_G] = \begin{bmatrix} q_{G_{11}} & q_{G_{12}} & q_{G_{13}} \\ q_{G_{21}} & q_{G_{22}} & q_{G_{23}} \\ q_{G_{31}} & q_{G_{32}} & q_{G_{33}} \end{bmatrix} \tag{3.1}$$

where its components can be evaluated as follows:

$$\begin{aligned}
q_{G_{11}} &= -\sin(e_1)\sin(e_3) - \cos(e_1)\cos(e_3)\cos(e_2) \\
q_{G_{12}} &= \cos(e_1)\sin(e_3) - \sin(e_1)\cos(e_3)\cos(e_2) \\
q_{G_{13}} &= \cos(e_3)\sin(e_2) \\
q_{G_{21}} &= \sin(e_1)\cos(e_3) - \cos(e_1)\sin(e_3)\cos(e_2) \\
q_{G_{22}} &= -\cos(e_1)\cos(e_3) - \sin(e_1)\sin(e_3)\cos(e_2) \\
q_{G_{23}} &= \sin(e_3)\sin(e_2) \\
q_{G_{31}} &= \cos(e_1)\sin(e_2) \\
q_{G_{32}} &= \sin(e_1)\sin(e_2) \\
q_{G_{33}} &= \cos(e_2)
\end{aligned}$$

After defining Q_G, the slip systems normal and direction can be projected in the grain's

reference system as:

$$n_{\mathrm{G}}^{(s)} = [Q_G]\, n^{(s)^T} \tag{3.2}$$

$$b_{\mathrm{G}}^{(s)} = [Q_G]\, b^{(s)^T} \tag{3.3}$$

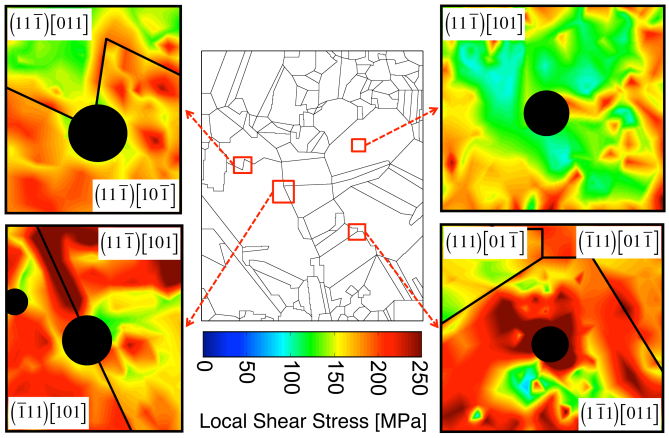

(a)

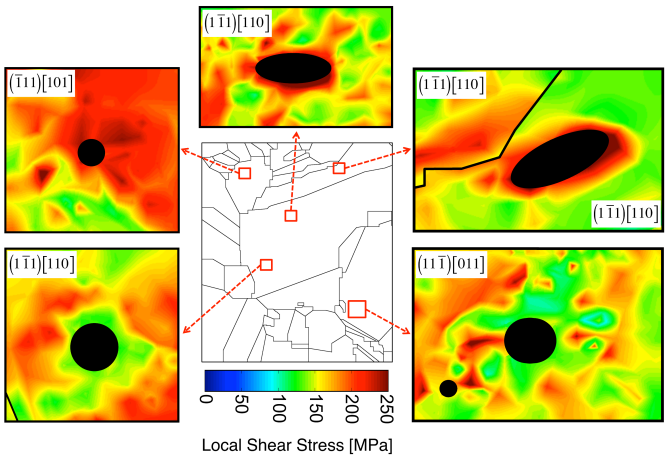

(b)

Figure 3.16: *Maximum local shear stress around several carbides introduced in the polycrystalline matrix: (a) carbides embedded in area A; (b) carbides embedded in area B.*

the third direction $l_{\mathrm{Grain}}^{(s)}$ is the cross product of $n_{\mathrm{Grain}}^{(s)}$ and $b_{\mathrm{Grain}}^{(s)}$. From these definitions is possible to calculate the rotation matrices for each slip system as:

$$[R]^{(s)} = \left[b_{\mathrm{Grain}}^{(s)^T}\, n_{\mathrm{Grain}}^{(s)^T}\, l_{\mathrm{Grain}}^{(s)^T} \right] \tag{3.4}$$

Then the rotated stress tensor can be evaluated as:

$$[\sigma]^{(s)} = [R]^{(s)}\, [\sigma]\, [R]^{(s)^T} \tag{3.5}$$

Finally from $[\sigma]^{(s)}$ the shear stress on each slip plane can be extracted, it corresponds to $\sigma_{13}^{(s)}$ component. Fig. 3.16 summarizes the results for some of the carbides identified on area A and B. These pictures show the stress field around the carbides and the slip plane that sees it. From these analyses it is possible to observe that not all the introduced carbides lead to high shear stresses but some of those brought to a shear that locally exceeds the yielding value (around 130 MPa).

3.3.4 Stress Field And Dislocation Density

The investigation then moved on the analysis of results that require constitutive equations and can not be obtained with DIC, more precisely stress field and geometrically necessary dislocations maps.

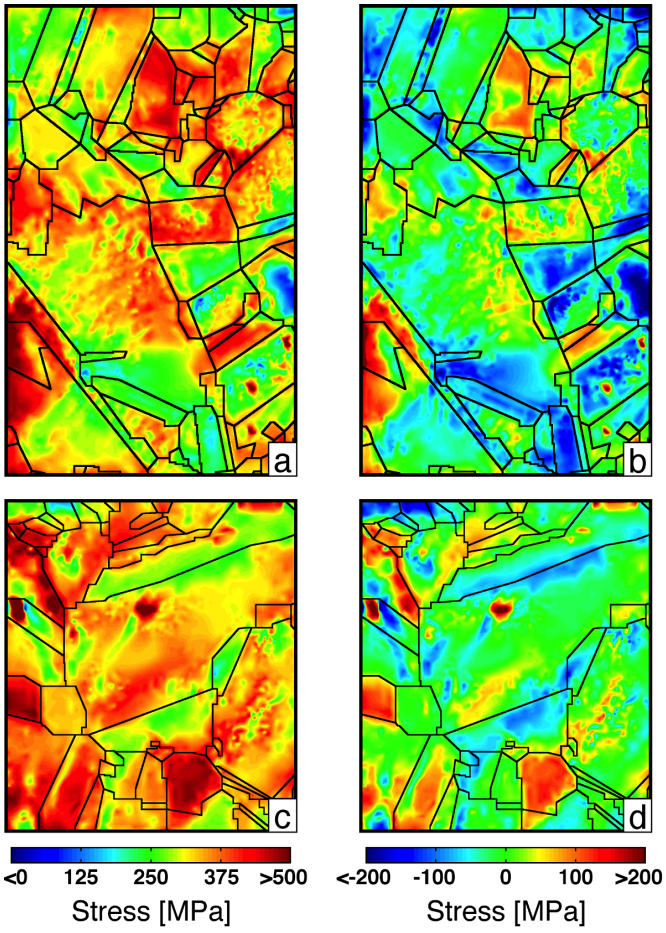

Figure 3.17: *HT polycrystalline simulation: stress fields along the loading direction. (a) and (c) are the stress field at maximum stress before the unload ((a) refers to area A and (c) to B); (b) and (d) are the residual stress field at 0 load applied and residual strain of 1.22% ((b) refers to area A and (d) to B).*

Fig. 3.17 shows the stress along the remote loading direction for Area A and B; shown are the stress fields at maximum applied stress and at the unloading, where the residual stresses can be evaluated. From the stress tensor obtained by the simulation it is possible to evaluate the local shear stress along slip traces. Considering now only the model concerning Area B, slip traces were identified for two grains [99, 100]: activated slip systems were identified by detecting the highest strain accumulation orientations. Considering the stress tensor at the maximum peak of the remote applied stress, before the first unloading, it was possible to evaluate the local shear stress along the identified traces. These results were then compared with the value of the externally applied resolved shear stresses, Fig. 3.18, obtained with the Schmid law [101]:

$$\tau_{\text{remote}} = m_{\text{SF}} \cdot \sigma_{\text{remote}} \tag{3.6}$$

where this shear stress is evaluated from the remote applied stress multiplied by the Schmid factor (m_{SF}) of the grain. This value is usually considered constant in the application of energy models for crack nucleation [102]. Fig. 3.18 shows that the constant values coming from Eq. (3.6) and the local shear stress are comparable and of the same order, agreeing with the hypothesis of Sangid et al. [102].

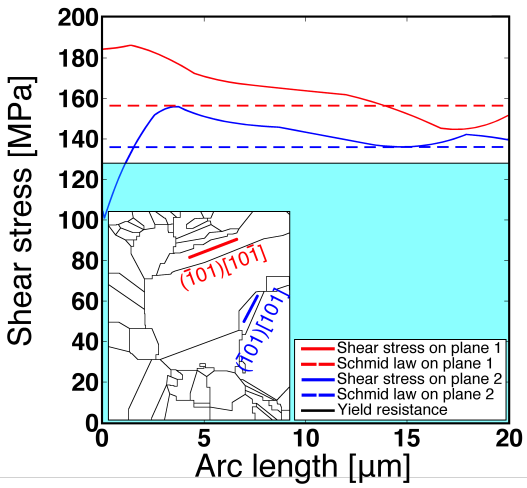

Figure 3.18: *Shear stresses variation along two identified slip traces and comparison with the Schmid law.*

Finally, since the adopted model provides the Nye tensor as an output [8], it was possible to determine the necessary dislocation density map through the relationship [35]:

$$\rho b = ||\alpha|| = \sqrt{\alpha : \alpha} \tag{3.7}$$

This quantity, in Fig. 3.19 for both area A and B, indicates the regions of high plastic strain incompatibility, where large densities of necessary dislocations developed to

maintain the compatibility throughout the model.

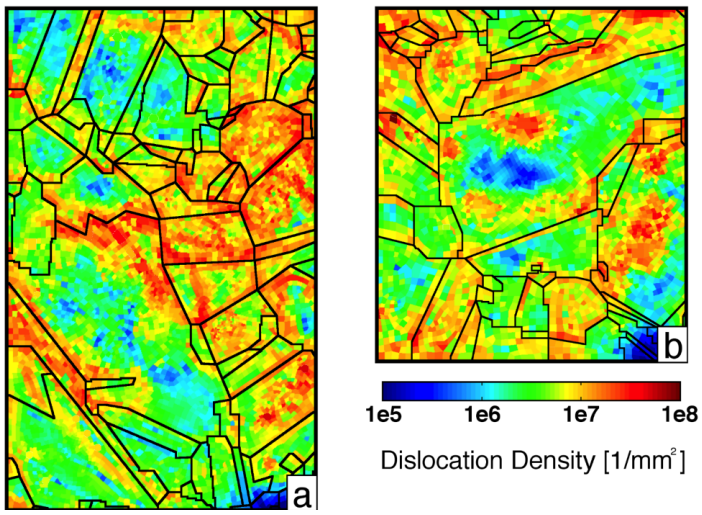

Figure 3.19: *Dislocation density maps at 1.22% residual average strain for area A (a) and area B (b).*

3.4 Conclusions

The models of this chapter allowed the description and the study of how the localization of strains acts on local scale level.

The global behaviour was well captured by the approximation of the stress-strain curves, for single crystals and polycrystalline models. In the study of the high temperature test, three models were created by assembling grains, different in sizes, dimensions and numbers. The interaction of the grains, each one can be considered locally as an anisotropic system, was able to reproduce the global behaviour of a specimen that on the macro-scale can be seen as homogeneous and isotropic. This result was accomplished since the models consisted of enough grains with as many orientation as needed to create a representative polycrystalline aggregate.

Finally the strain accumulations, on local scale, showed good agreements in terms of active grains. The introduction of carbides improved upon the description of the residual strain field, showing that they have a significant role inside the material.

The last result is related to the overall tensile curve reproduced by the models. Specifically, when the model is reloaded it was observed that the material changes from elastic to plastic behaviour before reaching the previous peak load. Thus there is strain accumulation within one unloading/reloading cycle. This capability of the CP model will be investigated more in detail in Chapter 4, where a cyclic test at room temperature is taken into account.

CHAPTER 4

Simulation Of A Ratcheting Test

This chapter focuses on the application of the crystal plasticity code to a ratcheting test, to see the capabilities in predicting strain accumulation under cyclic loads. Ratcheting is the progressive accumulation of plastic deformation cycle by cycle, and is not easy to simulate it accurately. Despite this fact models able to describe ratcheting are required in design and life assessment of components subjected to cyclic loadings with non-zero mean stress. Most of the models in literature rely on nonlinear kinematic hardening for continuum plasticity, defined starting from the work of Armstrong and Frederick [103], a definition that was proven necessary to predict life due to ratcheting fatigue. One of the major drawbacks of these model is that they predict good agreement on the macro scale, neglecting the link to the material microstructure. Their prediction can be considered as an average over many polycrystalline grains and is not able to capture the effective damage occurring at micro-level due to stress/strain intensifications. Another drawback of the models is linked to their applicability, for complex phenomena like ratcheting they are limited to special cases: most of the models were developed phenomenologically based on macroscopic experimental results [104].

Some authors [105, 106] provided results on simulations of ratcheting tests with crystal plasticity codes. Their analyses showed attempts in reproducing the local behaviour of a reference volume element, generated by statistical informations acquired

by EBSD, under cyclic loads. The results gave a fine approximation of the overall behaviour with a room of improvement for a better description. Furthermore, these studies pointed out the necessity to develop crack nucleation models that account for local damage, high plastic strain localization are potential sites for micro-crack initiation.

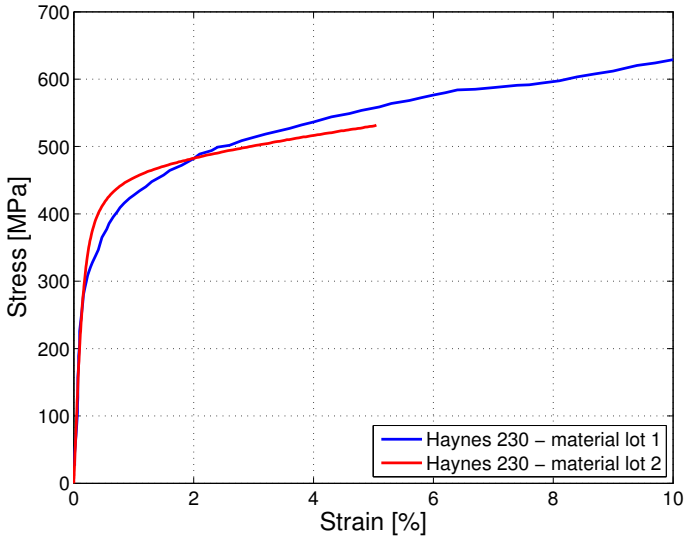

Figure 4.1: *Comparison of two different lot of Haynes 230.*

The material used for this chapter's experiments comes from a second lot of Haynes 230, which exhibits a different behaviour at room temperature if compared with the one analyzed in Chapter 3 (see Fig. 4.1). These differences, in yield stresses, 400 MPa vs 353 MPa, and in the work hardening slopes, require the identification of different parameters able to describe the new behaviour. In opposition with the procedure adopted in Chapter 3, the evaluation of the CP model parameters is carried out by the analysis of one tensile test conducted on a polycrystalline specimen, and not by the analysis of single crystals.

Then, with the new parameters, a ratcheting simulation of a polycrystalline aggregate is performed, considering both the overall behaviour and the effects of the number of cycles, focusing on the increasing of strain concentration across grains and grain boundaries.

4.1 Experimental Procedure

In this section, two experiments conducted on polycrystalline specimens are described: one tensile test that will be used as a feedback for the identification of the CP model parameters; one ratcheting test to verify the prediction of the model on strain accumulation during cyclic loadings.

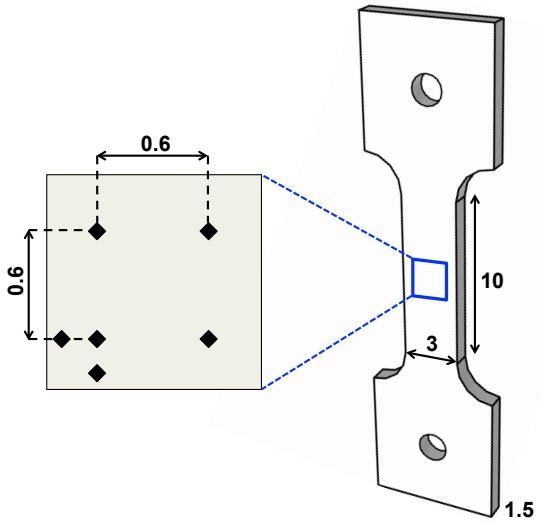

Figure 4.2: *Dog-bone specimen geometry adopted for tensile and ratcheting tests.*

The geometry of both specimens is schematized in Fig. 4.2. The two specimens have a dog-bone shape with parallel length of 10 mm, width of 3 mm and a thickness of 1.5 mm. At first they were mirror polished to perform EBSD analyses, necessary to create the models for the simulations. To constraint the area where EBSD has to work, the specimens were marked in the center of one face by Vickers micro-indentation. The markers were located in order to approximately describe a square of edge 0.6 mm.

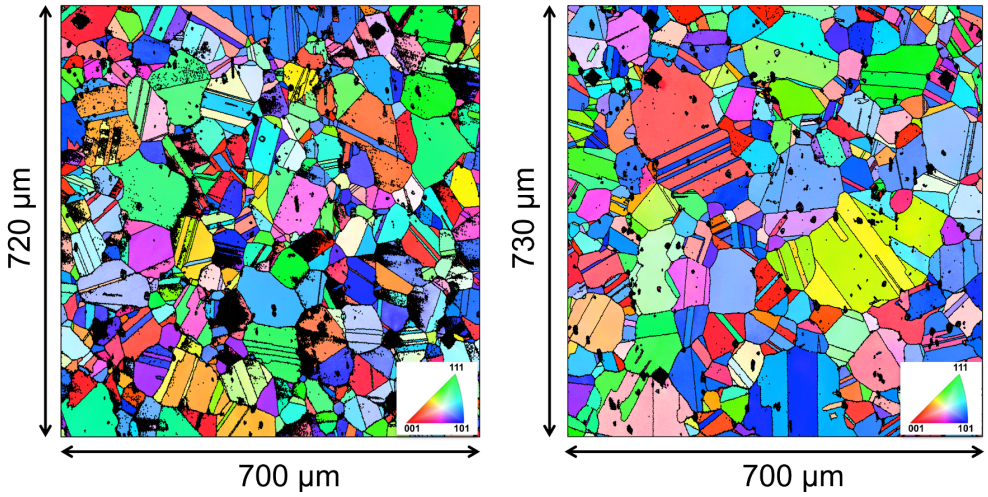

(a) (b)

Figure 4.3: *EBSD scan of the specimens selected for (a) tensile and (b) ratcheting tests. The EBSD analysis was performed with the axial/loading direction of the specimens oriented along the horizontal.*

The results of these scans are shown in Fig. 4.3, where map (a) refers to the specimen used for the tensile test, counting 706 grains, and map (b) to the ratcheting test, 537 grains. The EBSD was performed with the specimen bended, which means that the loading direction is horizontal (in Fig. 4.3) and not vertical like in Chapter 3. *Ex-situ* high-resolution DIC was used for strain measurement. In order to perform it, the marked areas were prepared. A speckle pattern suitable for high resolution DIC was applied on the surfaces. Images were captured at first, before testing the specimens, out of the load frame by means of a Carl Zeiss Axio Cam A1 optical microscope, with a resolution of: 0.34 μm/pixel (magnification of 100x) for the tensile test and 0.17 μm/pixel for the ratcheting test (magnification of 200x). Then, the tested specimens followed the same procedure of capturing images after the test, to perform correlations and obtain details about the strain field. The resulting strain field were then overlapped by the grain boundaries frames obtained by the EBSD using the markers as a reference.

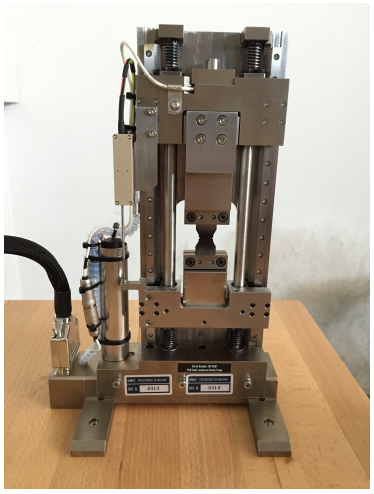

Figure 4.4: *Testing machine: DEBEN micro-testing machine 5kN dual leadscrew*

Both tests were carried out on a Deben micro-testing machine (Fig. 4.4). This electric testing machine is able to perform tests within a load range of 5 kN.

4.1.1 Tensile Test

The tensile test was performed in displacement control, the average deformation was measured by low magnification DIC instead of using an extensometer, which due to the dimensions was not applicable to the specimen. The specimen went through a loading/unloading tensile test, reaching a deformation of 5.05 % at peak load and then, after the unloading, the residual average deformation was 4.74 %. The specimen was then analyzed under an optical microscope (with a magnification of 100x) to capture the images which have to be correlated with the reference one to obtain the strain field.

This procedure allowed the evaluation of strain accumulation along grains and grain boundaries. From the procedure of the test, the outcome of this DIC investigation is the residual strain field at the end of the test. The results of the tensile experiments are summarized in Fig. 4.5: (a) is the monotonic curve, (b) is the strain field measured on the area where the EBSD was performed.

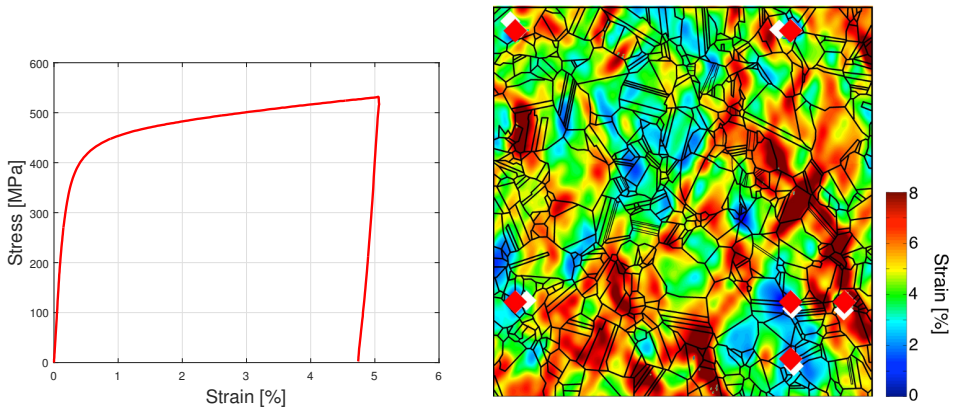

Figure 4.5: *Room temperature polycrystalline tensile test, experimental results: (a) monotonic curve; (b) ex-situ high resolution DIC.*

4.1.2 Ratcheting Test

The second dog-bone specimen was cycled in load control with a nominal applied stress range of $\Delta\sigma$ = 495 MPa and a load ratio of R = -0.1. The specimen was cycled between the maximum load of 450 MPa and the minimum load of -45 MPa.

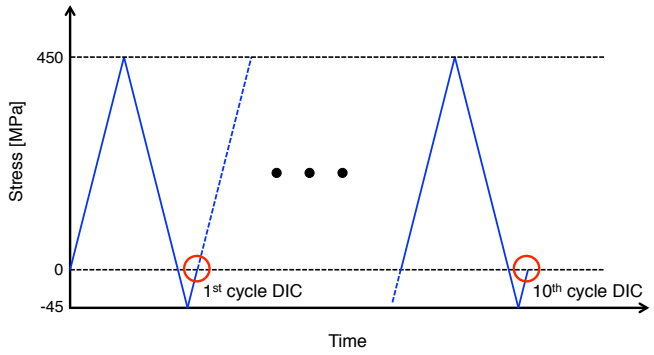

Figure 4.6: *Ratcheting test loading history and definition of the load instant when the ex-situ DIC was performed*

For DIC analyses the residual strains were registered after 1 cycle and 10 cycles:

the test was put on hold and the specimen was inspected under an optical microscope at a magnification of 200x. The stops followed the logic reproduced in Fig. 4.6, meaning that the specimen was removed when the test passed through the 0 load after the minimum valley.

The ratcheting test curves measured during the test for the first and the tenth cycles are shown in Fig. 4.7-a, and put in comparison with the tensile test in Fig. 4.7-b: the comparison shows a small variation in the yielding.

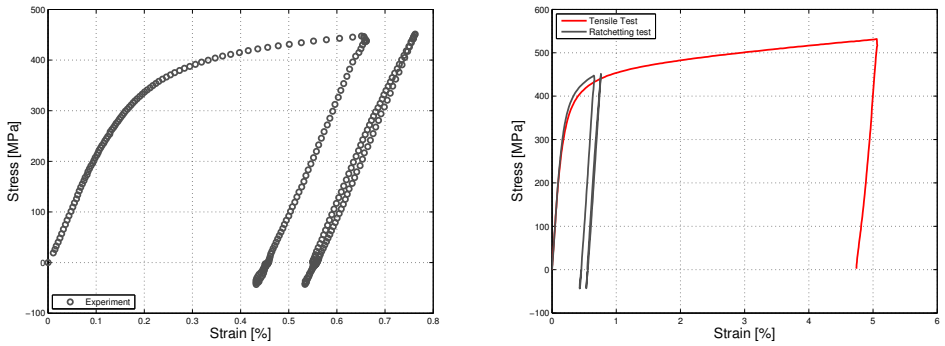

(a) (b)

Figure 4.7: *Stress-strain results for ratcheting test: (a) first and tenth cycles; (b) comparison between ratcheting and tensile curves.*

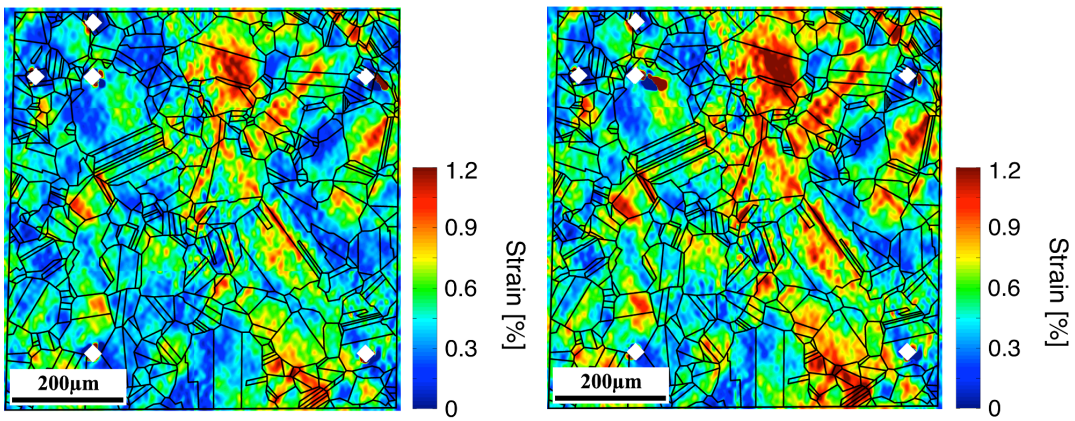

(a) (b)

Figure 4.8: *Measured strain localization during ratcheting experiment: (a) after 1 cycle, (b) after 10 cycles.*

The correlation of the images, with respect to the reference condition of un-tested specimen, allowed to the residual strain field identification and its intensification at

various hot spots. Fig 4.8 summarizes the 2 results (a) after the first cycle and (b) after 10 cycles. The comparison between the two deformation fields showed the grains whose activated slip planes saw an increasing in strain magnitude during the ten cycles test.

4.2 Parameters Identification

The identifications followed the iterative procedure of trial and error with the main objective of reproducing the tensile curve of Fig. 4.5-a. The evaluation of the constants for the model followed the idea of Chapter 3, with the main difference that here the estimation was done modeling a polycrystalline aggregate instead of three single crystals.

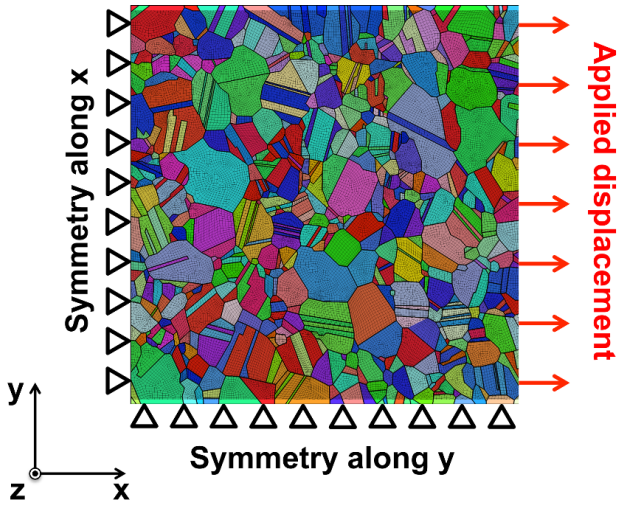

Figure 4.9: *Room temperature polycrystalline tensile test model: definition of constraints and applied load.*

The finite element model was created to simulate the specimen with microstructure shown in Fig. 4.3-a. The geometry of the generated model is shown in Fig. 4.9, where grains shape was reproduced from the information derived from the EBSD scan. Then each grain was reproduced assigning to the elements, that reproduce its geometry, the informations about the crystallographic orientations. The entire model counts about 102000 linear hexahedral elements over a volume of surface 0.722 mm by 0.702 mm with a thickness of 0.08 mm. The simulation of the tensile test was carried out by imposing displacement to the right surface of the volume (the loading direction of the specimen lays on the horizontal direction) and a double symmetry on the other two surfaces, as in the picture (this approach in the model follows that of Chapter 3).

The simulation was carried out with the main objective of capturing the overall stress strain behaviour of the material, and the parameters were modified according to

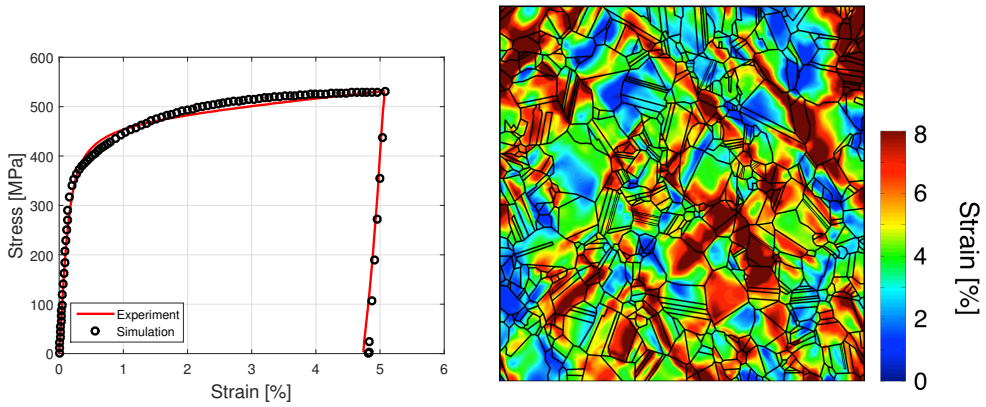

(a) (b)

Figure 4.10: *Room temperature polycrystalline tensile test, numerical results: (a) monotonic curve; (b) strain field obtained with the simulation.*

the best fit of the experimental curve. The localizations were investigated to capture the local strain field and compare it with the residual deformations observed with DIC. The fitting of the tensile curve pursued by this simulation was made considering the parameters of Tab. 4.1, that produce the results of Fig. 4.10. In Fig. 4.10-a it is possible to observe an excellent agreement between the predicted tensile test curve and the experimental one; Fig. 4.10-b shows that the prediction, if compared with

Table 4.1: *Material parameters for the second lot of Haynes 230.*

Property	Description	Value
E	Young's modulus	195 GPa
ν	Poisson's ratio	0.33
μ_0	Shear modulus	80 GPa
b	Burgers Vector	$3.5\,E-7$ mm
$\hat{\tau_a}$	Athermal slip resistence	0 MPa
$\hat{\tau_y}$	MTS strength for intrinsic barrier (yield)	119.8 MPa
$g_{0,y}$	Normalized activation energy for intrinsic barriers	2.37
q_y	Shape coefficient for intrinsic barriers	1.8
p_y	Shape coefficient for intrinsic barriers	0.9
$\epsilon_{0,y}$	Strain rate sensitivity for intrinsic barriers	$1\,E10$ s^{-1}
$\hat{\tau_v}$	MTS strength for work hardening	65 MPa
$g_{0,v}$	Normalized activation energy for work hardening	1.6
q_v	Shape coefficient for work hardening	0.34
p_v	Shape coefficient for work hardening	0.5
$\epsilon_{0,v}$	Strain rate sensitivity for work hardening	$1\,E7$ s^{-1}
ϑ_0	Initial hardening slope	24000 MPa
k_0	Geometric hardening parameter	5

Fig. 4.5-b, leaks on some grains while on other is able to capture the activation and the magnitude of the localized deformation. Considering Tab. 4.1, the main difference with Tab. 3.1 is in ϑ_0 parameter. The new value is higher and it had been chosen in order to have a more accurate description of the first part of the tensile curve. A choice made considering that the ratcheting test was cycled close to the yielding of the material.

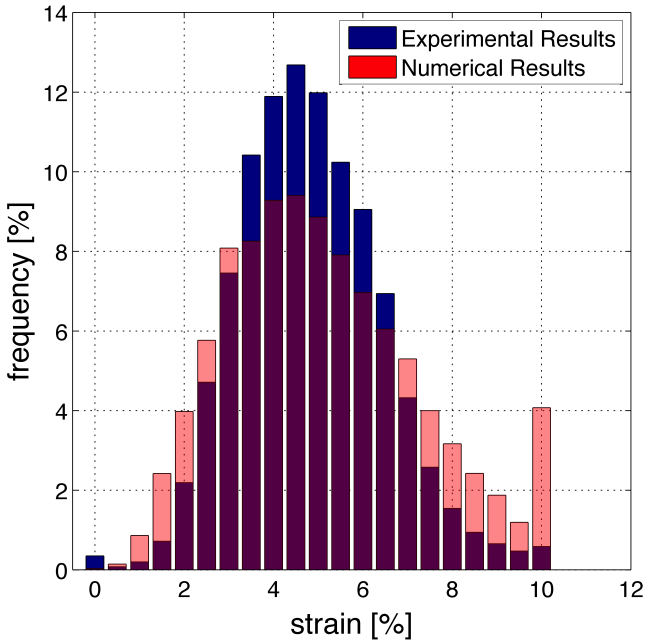

Figure 4.11: *Histogram comparison of the strain fields detected by DIC and simulation for room temperature tensile test.*

Further analysis of the agreeability between the localization of the experiment and the simulation can be derived by the histogram of the strains. Fig. 4.11 shows a reasonable capacity of the model to capture the trend of the strain distribution along the analyzed area, with a good approximation of the mean value, 4.83% for the experiment and 5.04% for the simulation. The simulation distribution has higher occurrences along the tails, which implies that the frequency around the mean value is lower than the one observed by DIC.

4.3 Ratcheting Model

The simulation of the ratcheting test required the definition of the model starting from the EBSD of Fig. 4.5-b.

The model of Fig. 4.12 reproduces the outcome of the EBSD, and, as the previous model, each elements contains the information about the euler angles of the grain it represents. The ratcheting model counts 111000 linear hexahedral elements, contained

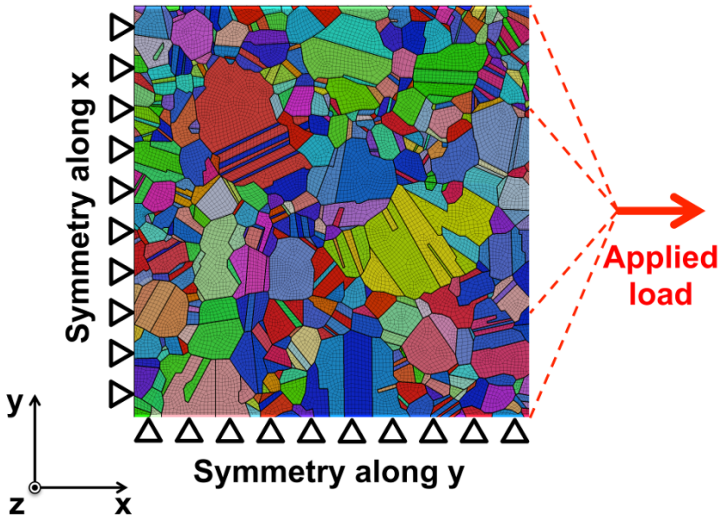

Figure 4.12: *Room temperature polycrystalline ratcheting test model: definition on constraints and applied load.*

in a volume of 0.703 mm by 0.731 mm by 0.08 mm (thickness). A double symmetry was modeled by the constrains, as in the figure, and the load was applied coupling the displacements of the free surface perpendicular to the loading direction (horizontal) to those of the node where the force is applied.

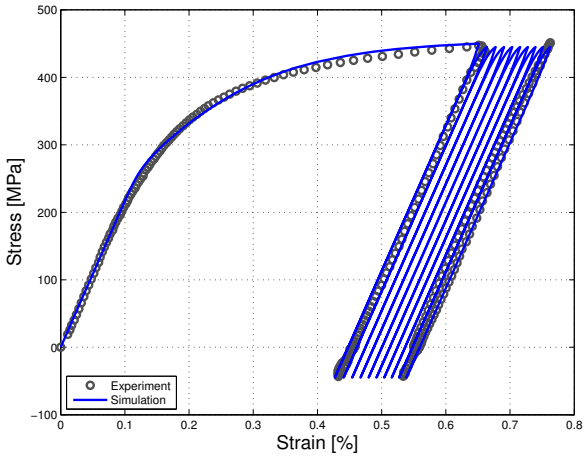

Figure 4.13: *Matching between experimental and simulated stress-strain curve for the ratcheting test.*

The prediction on the stress-strain curve, Fig. 4.13, shows an excellent agreement with the test, capturing both the measured cycles (first and tenth). As for the strain localizations shown in Fig. 4.14, the agreement is good on several of the hot spots identified by the experiment, with a good estimation of the reached strain peaks.

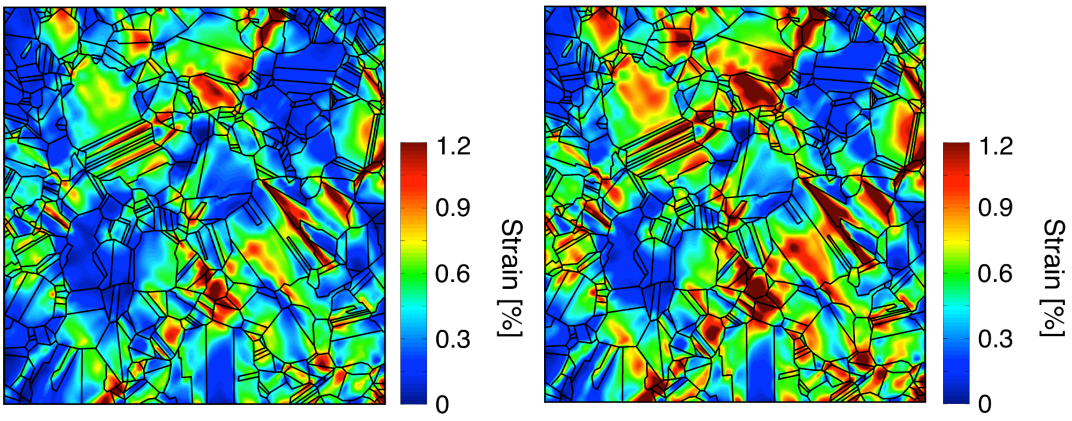

(a) (b)

Figure 4.14: *Ratcheting simulation, strain localization detected: (a) after 1 cycle, (b) after 10 cycles.*

4.4 Conclusions

In this chapter the parameters for the crystal plasticity model were estimated from a polycrystalline tensile test (polycrystal specimen are usually less expensive than single crystal one) and a good agreement was observed on the comparison between the experimental monotonic curve and the simulated one.

Further applications of the crystal plasticity code concerned the simulation of a ratcheting test. The results pointed out a good capability in capturing both the overall behaviour of the test and the strain localization/accumulation with cyclic loadings.

Eventually, the possibility to apply the CPFE simulation to predict the cyclic behaviour may lead to the implementation of a model which accounts for crack nucleation, like the one proposed by Sangid [102].

CHAPTER 5

Fatigue Crack Growth In Single Crystals

The topic of this chapter deals with the analysis of crack propagation in single crystal specimens, with the aim to provide a more accurate understanding of crack growth mechanisms in grains. In the first part a discussion of the experimental procedure is reported together with crack growth measurements: DIC was used for determining closure levels and the cyclic plastic region at the crack tip.

The following sections, provide a comparison between experimental results and numerical ones, obtained with CPFE models. At first the single crystal medium is analyzed performing simulations on quasi-static crack models, to provide an initial assessment of the plastic zone; then crack closure is studied by implementing a node release technique to consider crack advancement.

5.1 Experimental Setup: Single Crystal Crack Growth

The tests were performed in order to study the displacement field around the crack tip, hence the strain localization, and obtain a measure of the crack opening levels. These analyses required the use of the DIC technique.

Single crystals were obtained from seeds, adopting the Bridgman technique [94] in vacuum: its initial orientation was determined using EBSD. The two tested speci-

mens had [001] and [111] orientations along the loading direction. Single edge notch specimens were chosen to complete the experiments: notches were made by electrical discharge machining (EDM). The specimens nominal dimensions are registered in Fig. 5.1: a width of 3 mm, a parallel length of 8 mm and a notch length of 0.5 mm. The nominal thickness of 1mm was indeed 1.09 mm for the [001] specimen and 1.3 mm for the [111].

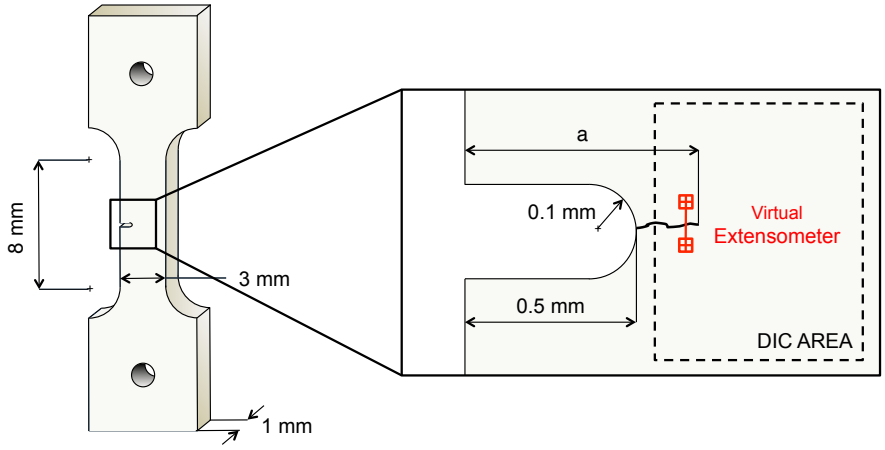

Figure 5.1: *Geometry of the single crystal specimen with details of the notch and position of the virtual extensometers.*

The specimens were mirror polished to apply the speckle pattern, using black paint, for DIC analysis. The tests were performed with a cyclic frequency of 5 Hz on a servo hydraulic load frame with a load ratio R equal to 0.05. Specimen [111] was loaded with $\Delta\sigma = 181$ MPa, while [001], which exhibits a lower yield stress (see Fig. 3.4), was loaded with $\Delta\sigma = 133$ MPa. Once a crack was observed, measurements were performed every 4 seconds, to get enough pictures to characterize the fatigue load cycle. The displacement field around the tip was characterized with DIC. The correlations were made considering a reference image at the minimum load, it means that all the displacements were calculated with respect to the fully closed crack configuration. The strain field was computed from DIC measured displacements: Lagrange strain tensor equations were employed to calculate strains.

In order to measure crack opening loads, a series of 2 points extensometers were placed along the crack flanks (see Fig. 5.1. This feature tracks the relative displacement of 2 points belonging to the opposite face of the crack. The opening was evaluated by placing the digital extensometers perpendicular to the crack plane and by considering the difference in crack tip displacements.

For [001], where the crack propagates horizontal under mode I, only the vertical displacement was considered. For [111], where the crack propagates on a inclined plane

under mixed mode (I+II), both horizontal and vertical displacements were measured. Fig. 5.2 shows a summary of the DIC results for the 2 specimens. More detailed descriptions are recorded in [13, 107]

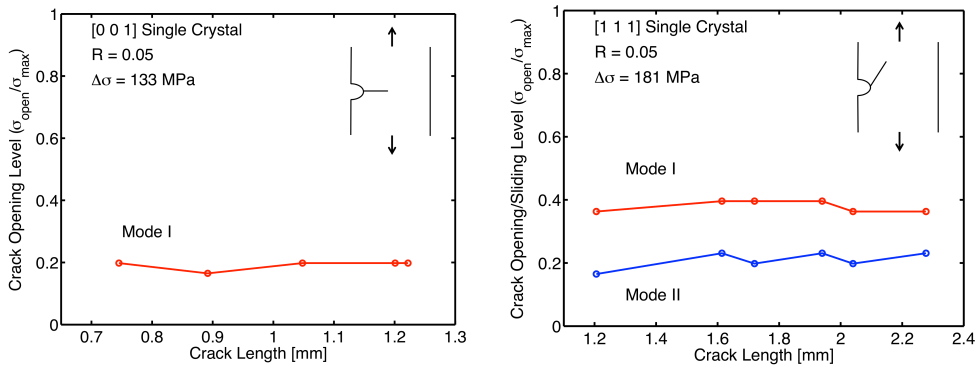

(a) (b)

Figure 5.2: *Crack opening level measured experimentally for (a) [001] and (b) [111] oriented single crystal specimens [13].*

5.2 Single Crystal Models

The single crystal analyses were performed at first considering a quasi-static crack under the effective applied load (defined as the load range between the instant the crack is fully open and the maximum applied load) to obtain a first approximation of the plastic zone ahead of the crack tip [107] . Then a crack propagation model was implemented for the [001] oriented specimen to have a better comparison with the experimental results. The crack propagation model for the [111] direction is still under development.

5.2.1 Quasi-Static Crack Analysis

An first assessment of crack tip plastic zone was obtained by considering the crack as stationary, neglecting the effects of plastic wake during crack propagation. The definition of the models for [001] and [111] specimens is depicted in Fig. 5.3: in Fig. 5.3-a are showed the crystal direction that were used for the simulations and in purple are the plane where the crack propagates (cyans are the slip planes); in Fig. 5.3-b the dog-bone specimen used for the 2 simulations is reproduced, with evidence on the geometry of the two cracks embedded. [001] model has a crack of 0.955 mm under mode I, [111] specimen has a crack of 1.6 mm under mode I+II.

The models were constrained to fully reproduce experimental conditions: an constrains neglected all displacements of the bottom face, whereas the force was applied,

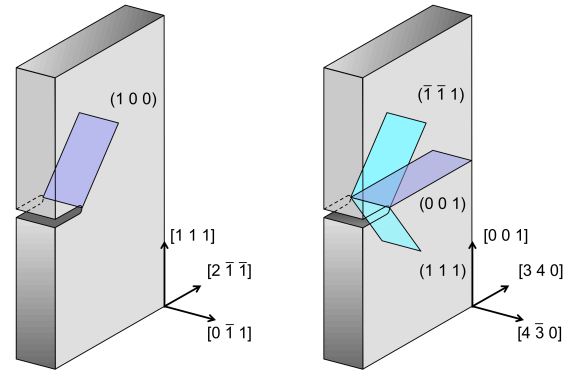

(a)

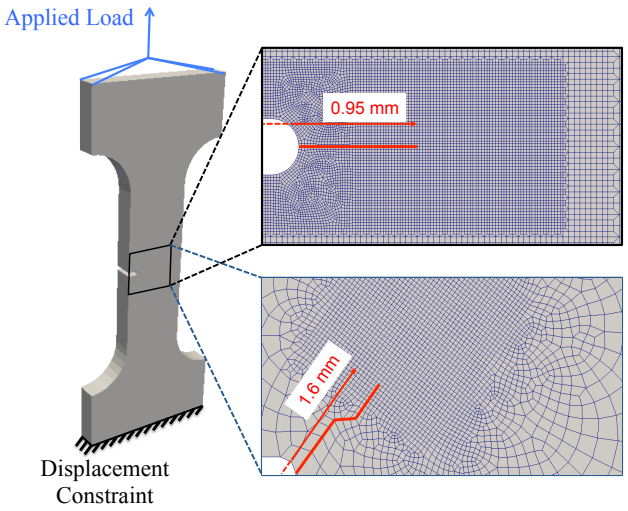

(b)

Figure 5.3: *Schematization of the single crystal specimens: (a) identification of the crack planes [13]; (b) geometry of the models used for the quasi-static simulations with details of crack extension for the two specimens.*

through a coupling constraint, on the upper surface of the model. In order to accurately describe the strain field ahead of the crack tip, 8-node 3D isoparametric elements with an in-plane dimension of 1% of the model thickness was employed during the analysis.

A first assessment of the crack propagation direction was made with models without crack; they were loaded with nominal stress ranges of 133 MPa for [001] and 181 MPa for [111], obtaining the results of Fig. 5.4, which shows strains accumulations along directions that are related to those depicted in Fig. 5.3.

The quasi-static models were developed neglecting the effects of crack growth and closure. The applied load was modified with respect in order to keep the crack always open and to apply the experimentally measured effective stress intensity factor range.

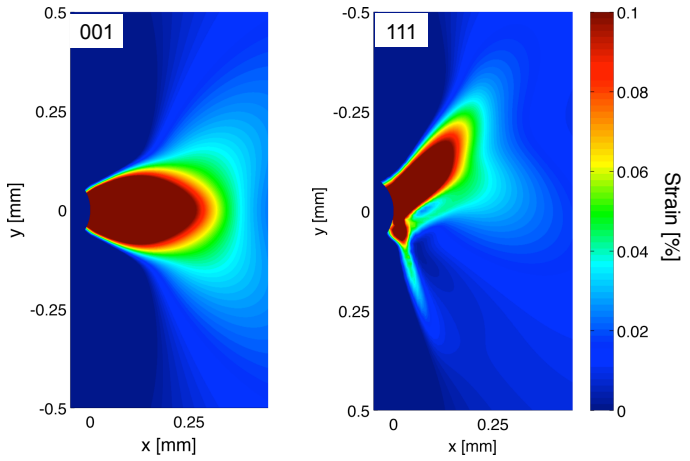

Figure 5.4: *Assessment of the capabilities of the CP model in predicting crack propagation directions from the notch for [001] and [111] oriented specimens.*

For the two models, the load range was taken between opening in mode I and maximum load, as reported in Fig. 5.5-a.

DIC does not provide an absolute measurement of strains. All the strains are evaluated with respect to a reference image taken at minimum load. Therefore the experimental strain field represents the difference between the strains at the maximum peaks and at the minimum. Thus, a comparison between FEM and DIC is only possible if the difference between the strains computed at the peak and at the opening stress is

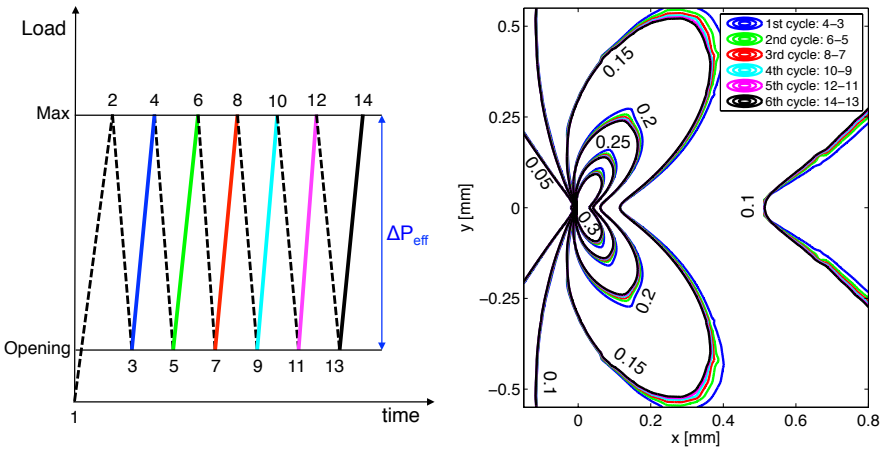

(a) (b)

Figure 5.5: *Strain field saturation in quasi-static analysis for the [001] oriented specimen with a crack of 0.955 mm [107]. (a) loading history of the quasi-static model considering 6 cycles. (b) Strain field contours (strains are in percentage) for each cycle to analyze results saturation.*

considered. In Fig. 5.5-b, the evolution of axial strain difference, $\Delta\epsilon_{yy}$, during six consecutive cycles is reported for [001] specimen (this six cycles are those coming from Fig. 5.5-a, the strains differences are between point 4 and 3 for the first cycle, 6 and 5 for the second and so on for the others); a major difference between the first and the following cycles is observed, whereas saturation is achieved after the fifth cycle.

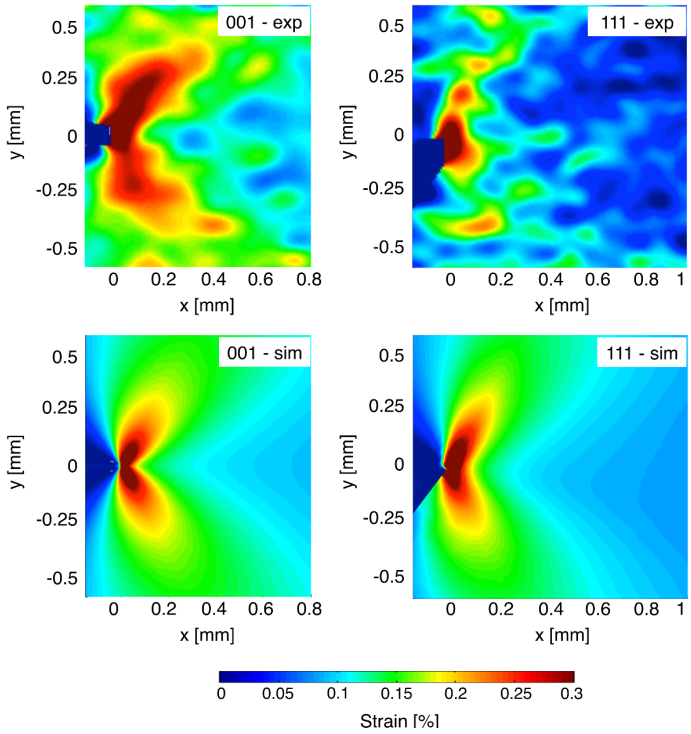

Figure 5.6: *Comparison between the extension of the plastic zones measured experimentally, for [001] and [111] specimens, and those evaluated by the quasi-static simulations.*

Finally, a comparison between experimental and numerical results is reported in Fig. 5.6, it shows that the extension of the plastic zones is quite different, whereas a good agreement in terms of band orientation is obtained. These observations leads to the conclusion that the quasi-static models cannot fully represent the fatigue cracks: the assumption of neglecting the plastic wake, and the subsequent crack closure effect, is the main limit of this models, since no irreversibility and strain accumulation ahead of the crack tip are modeled during fatigue crack growth.

5.2.2 Crack Propagation Model For [001] Oriented Specimen

The results of the quasi-static analysis can be summarized in the capabilities of the CP model to capture the slip angles where the crack may propagate and in a first estimation of the number of cycles necessary to reach strain field saturation. Those informations

were employed to develop an enhanced model, in which the effects due to crack growth were taken into account.

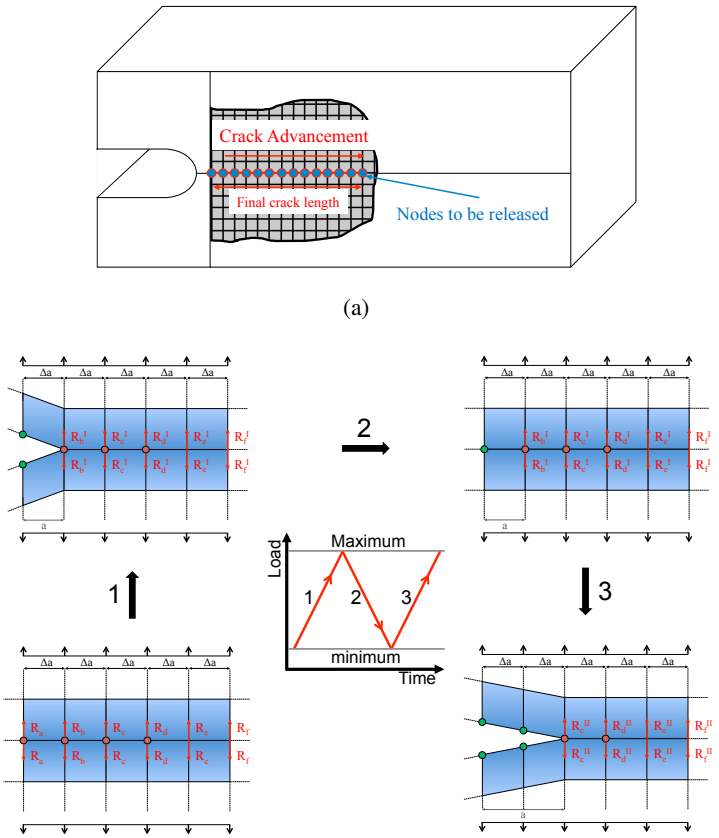

Figure 5.7: *Node release technique: (a) definition of the plane where the crack propagates; (b) procedure for node release with redistribution of the reaction forces between the nodes of the remaining ligament.*

The crack propagation is realized via a node release technique. It consists in releasing, during a pre-defined load cycle, all the nodes belonging to the current crack front. The instant node release can occur before or after the maximum peak or after the minimum load [51]. Accordingly, the crack is advanced uniformly over the thickness during the simulation, by an amount equal to the element size. Fig. 5.7 shows a schematic of the definition of the plane where the crack belong (Fig. 5.7-a) and advancement of the crack when the nodal constraint is released at the maximum peak (Fig. 5.7-b): when the constraint is released its reaction forces go to 0 and stresses/strains are redistributed to the nodes that are still on the material ligament. To avoid numerical error the redistribution of the loads is not instantaneous but takes some steps to be accomplished.

The simulation was performed implementing a small precrack emanating from the

notch. This transition crack removes the influence of the notch field from the stress intensity factor: this small crack was estimated as $0.13\sqrt{L_{\text{notch}}R_{\text{notch}}}$ (where L_{notch} and R_{notch} are notch length and its radius) [108]. Accordingly, a precrack of 30 μm was included in the model at the notch root.

As defined, the crack propagates by a quantity equal to the in-plane element size, this dimension was taken equal to 0.01 mm: this values comes the relationship, provided by McClung et al. [51], between element size (Δa) and the plastic radius (r_p), which states $\Delta a/r_p \leq 0.05$. A further mesh refinement was made to evaluate mesh size effects, considering 0.005 mm elements, but no significative difference was observed: thus for computational time the model with element dimensions of 0.01 mm was preferred. Fig. 5.8 shows a close up of the mesh along the crack region for the specimen, where the crack propagation was considered till reaching a length of 0.95 mm, close to the quasi-static model one. In the same picture, the loading direction and the constraints applied to the model are displayed: to reduce computational times, two symmetries were considered, meaning that only one quarter of the specimen was modeled. Symmetries were modeled constraining displacements along the direction normal to the symmetry plane, and a coupling constraint was applied to the upper surface to impose the remote load.

The simulation keeps track of the cyclic loading of the experiment, a stress range of $\Delta\sigma = 133$ MPa with a load ratio R=0.05 was applied. The loading cycle was studied to be able to capture the opening effect and to grant a good redistribution of stresses and strains at the crack tip when the node release occurs. Considering the load cycle in Fig. 5.8, it refers to the node release at maximum load. The small increments at the beginning of the cycle were necessary to provide better resolution in order to detect the opening load. Another step refinement involves the instants immediately after the peak load, where the node was released: this feature is necessary to have full redistribution of the reaction forces acting on the released nodes. Finally, another step refinement was placed in the last part of the cycle, to avoid numerical error during crack flanks contact.

Following the saturation results showed in Fig. 5.5-b, three different node release strategy were considered: a node release every cycle, every two cycles and every five cycles (the shape of the loading cycle stays the same as described before, also for the cycles where node release does not occur). From this simulation it was possible to obtain strain field saturation even for this case. To reproduce the experimental results, observed in section 5.1, it was necessary to compute the difference between the strains registered at maximum and minimum load. Fig. 5.9 shows the range of the vertical strain registered at the end of the simulation for the three node release strategies: the analysis of the saturation of the strain field contours pointed out that in the node release

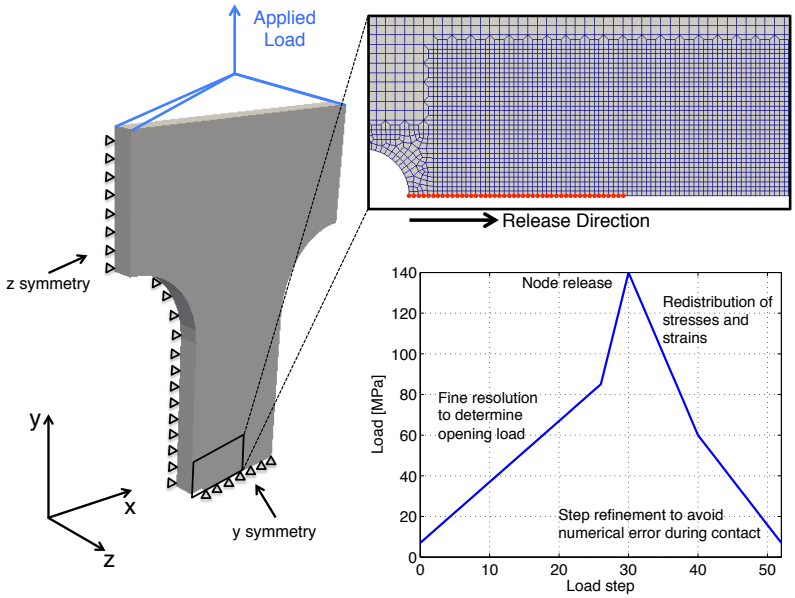

Figure 5.8: *Model for crack propagation in [001] single crystal: model loading conditions and symmetry constraints; definition of the crack and the nodes which are released during the simulation; details of the load cycle for node release after the maximum load.*

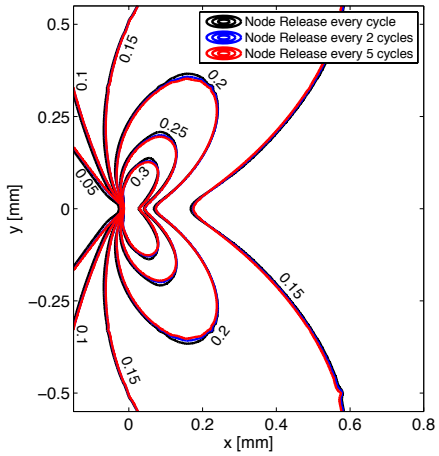

Figure 5.9: *Effect of the node release strategy on the strain field measured at a crack length of 0.95 mm: the comparison relies on contours with strains expressed in %.*

models the saturation is reached in less cycles than those observed in Fig. 5.5 for stationary crack. Accordingly, the differences between the results with a node release every cycle and every 5 cycles are negligible in terms of strain field range.

Crack opening levels were calculated following the procedure described in [109, 110] and depicted in Fig. 5.10-a: here the ratio between the vertical displacement at the second node behind the crack tip and the maximum displacement of this node was plot-

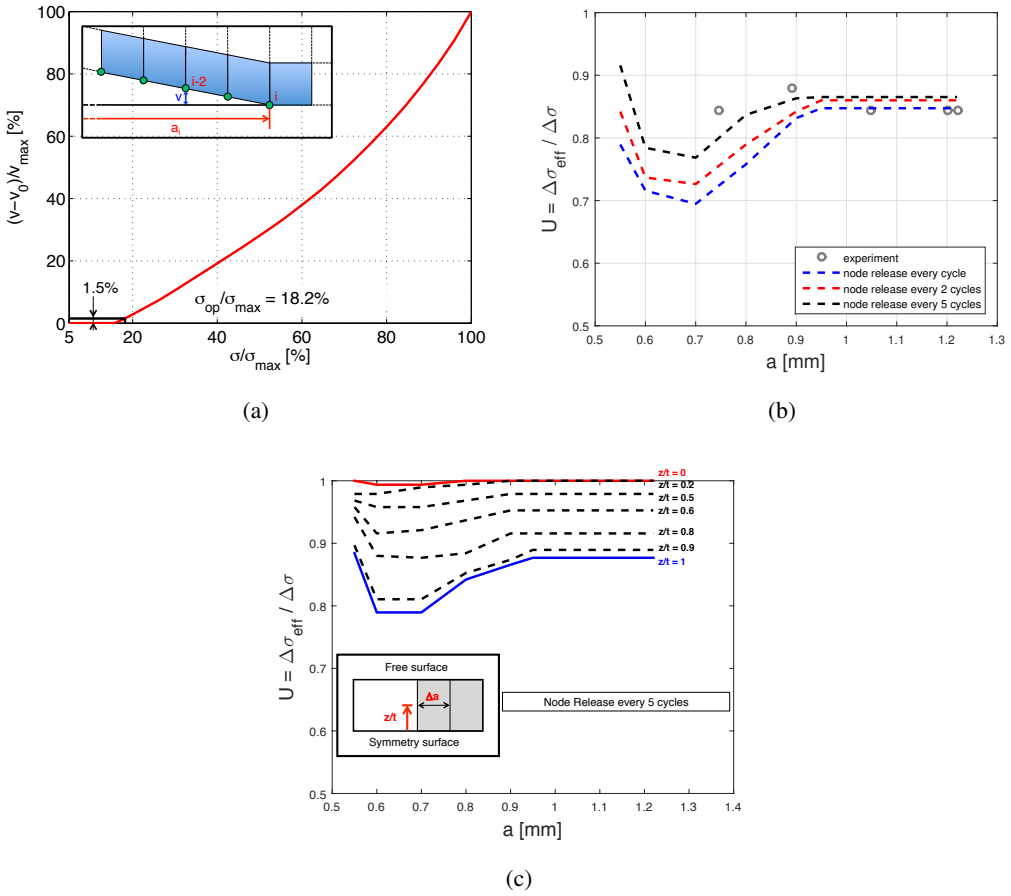

Figure 5.10: *Crack closure measurements in the numerical model. (a) Numerical criterion for the determination of the opening level from finite element analysis [109, 110]; (b) comparison between experimental and numerical results considering the three node release strategy; (c) analysis of the COD through the thickness of the specimen for the releasing strategy every 5 cycles.*

ted against the applied stress. The crack is assumed to be open when the ratio was equal to 1.5% [109]. It was found out that crack opening levels for the 0.955 mm long crack depend on the number of cycles between each release: release every cycle predicts an opening at 19.5% of the peak stress, every two cycles at 18.5% and every five cycles at 17.8%. The difference between the model with an advancement every cycle and the one that considered crack propagation every 5 cycles was lower than 10%, meaning that a good estimate of crack opening levels can be obtained even with a model that considers a limited number of cycles between two node releases, as reported in Fig. 5.10-b. In this picture a good agreement between experimental and FEM opening results is observed in terms of stress reduction factor $U = \Delta\sigma_{\text{eff}}/\Delta\sigma = \sigma_{\max} - \sigma_{\text{op}}/\Delta\sigma$

for increasing values of crack length. In this formulation $\Delta\sigma_{\text{eff}}$ is the effective stress range evaluated as the difference between the maximum applied stress $\sigma_{\max}$ and the opening stress σ_{op}. Following [59] the COD levels are evaluated in the thickness, Fig 5.10-c shows the variation of the opening level from the central section of the model to the surface: according to the literature the COD values decrease from the external surface (plane stress condition) till reaching the minimum values at the central/symmetry surface (ideally in plane strain condition) where the crack is considered as being always open.

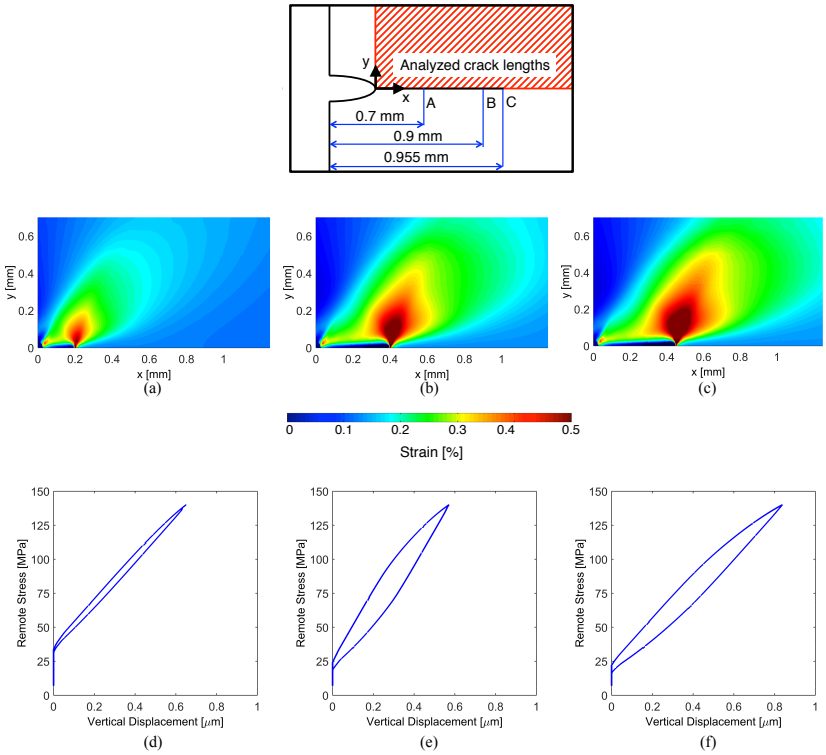

Figure 5.11: *Plastic wake for [001] specimen when the crack is 0.7, 0.9 and 0.95 mm long. (a-c) total strain field at the peak stress of the fatigue cycle; (d-f) remote stresses against vertical displacements measured at the second node behind crack tip.*

The attention was then shifted on the study of the capabilities of the model to describe the plastic wake extension and its effect on σ_{op}, as reported in Fig. 5.11, where the results of the model with the precrack and a node release every 5 cycles are reported. In Fig. 5.11-a,b,c the peak strain fields (no difference with the reference condition was made) for three different crack lengths (0.7 mm, 0.9 mm and 0.95 mm) are shown: it can be observed that the crack tip plastic zone is increasing during the propagation. Then a link between the opening values and the augmentation of the hysteretic behaviour of the material was evaluated, the remote applied stress is plotted against the

displacement at a node behind crack tip (as in Fig. 5.10-a). This plots are summarized in Fig. 5.11-d,e,f where the hysteresis loop is increasing going from the smaller crack length to the final one; the opening level that can be estimated from these plots are comparable with the one showed in Fig. 5.10-b.

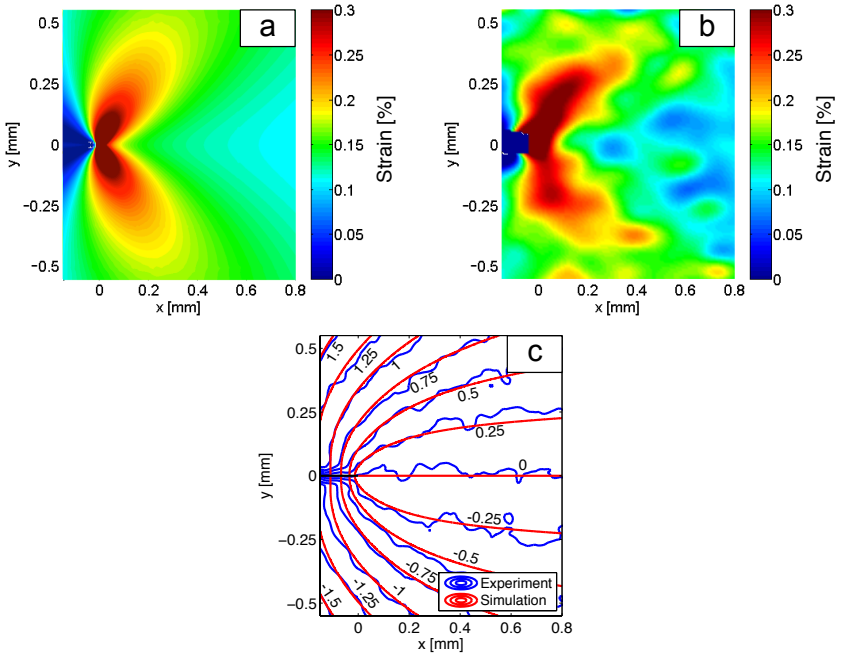

Figure 5.12: *Comparison between experimental and numerical results for [001] single crystal crack propagation at a crack length of 0.95 mm, considering the model with a node release every 5 cycles: (a) experimental strain field; (b) numerical strain field; (c) comparison between experimental and numerical vertical displacement fields (contours are in μm).*

Finally a summary of the results achieved by the simulations is recorded in Fig. 5.12, the results here are depicted for the case of node release every 5 cycles. Fig.s 5.12-a,b compare the strain fields ahead of the crack tip for simulation and experiment: a larger strain concentration is observed at the crack tip, meaning that the strain accumulation during crack propagation is the main cause for the wrong assessments provided by the quasi-static simulations. A good agreement and a better understanding of the capabilities of the numerical model can be observed from Fig. 5.12-c, where the vertical displacement is compared: hence the model is capable of describing not only the process zone, but also those points outside the singular region.

The results showed till here consider the crack advancing with node release at maximum peak. Considering node release at minimum load, the results, obtained in comparison with the previous type of modeling, can be summarized in Fig. 5.13. Here can be observed that the displacement fields predicted at the crack tip show no differences

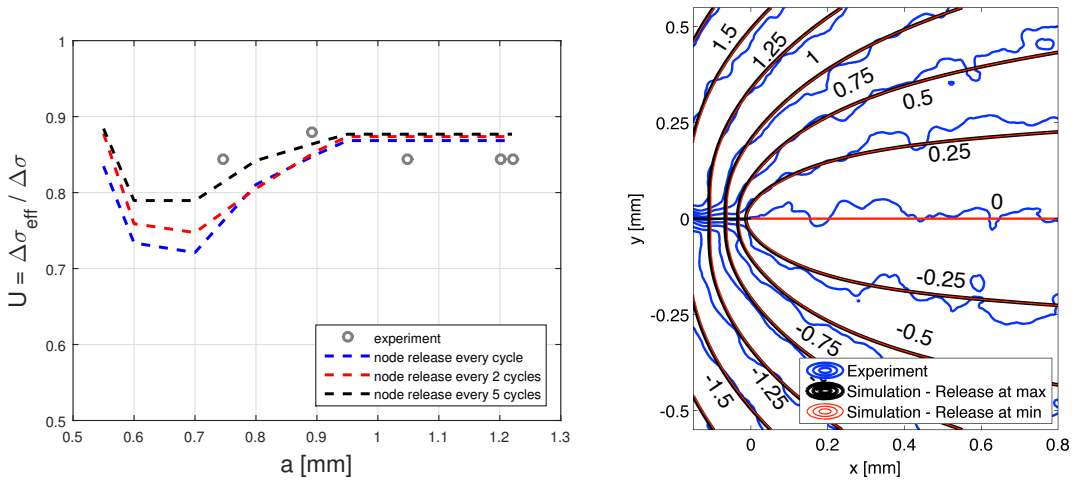

(a) (b)

Figure 5.13: *Effect of the node release at minimum load: (a) opening values for the three node release strategies and comparison with the experimental results; (b) comparison of vertical displacements from experiment and simulations with node release at maximum load and minimum load (contours are in μm).*

between the two cases and the COD estimated is still in good agreement with the experimental results. Comparing the numerical values obtained in Fig. 5.10-b with those of Fig. 5.13-b, the simulation with node release at minimum load shows a decreasing of the estimated COD by 1-2%; this result is in accordance with those described in [51, 52].

Effect of the notch on the crack opening

In the study of crack propagation the assumption of considering a small precrack at the notch was made, to prevent its effects on the first plasticization of the near area. If the tip of the notch is considered as starting point for crack propagation, the results are not influenced far from it but close to it the plastic area and the opening values are affected.

Fig 5.14 shows a comparison in terms of total strain field and COD with the previous analyses: Fig. 5.14-a,b shows a difference in the residual strain region at the beginning of the propagation, close to the notch, while after a certain crack length there are no sensible differences. Fig. 5.14-c,d, where crack opening values are put in comparison, shows a significant difference in the transitory regime before reaching saturation after the crack reaches about 0.7 mm.

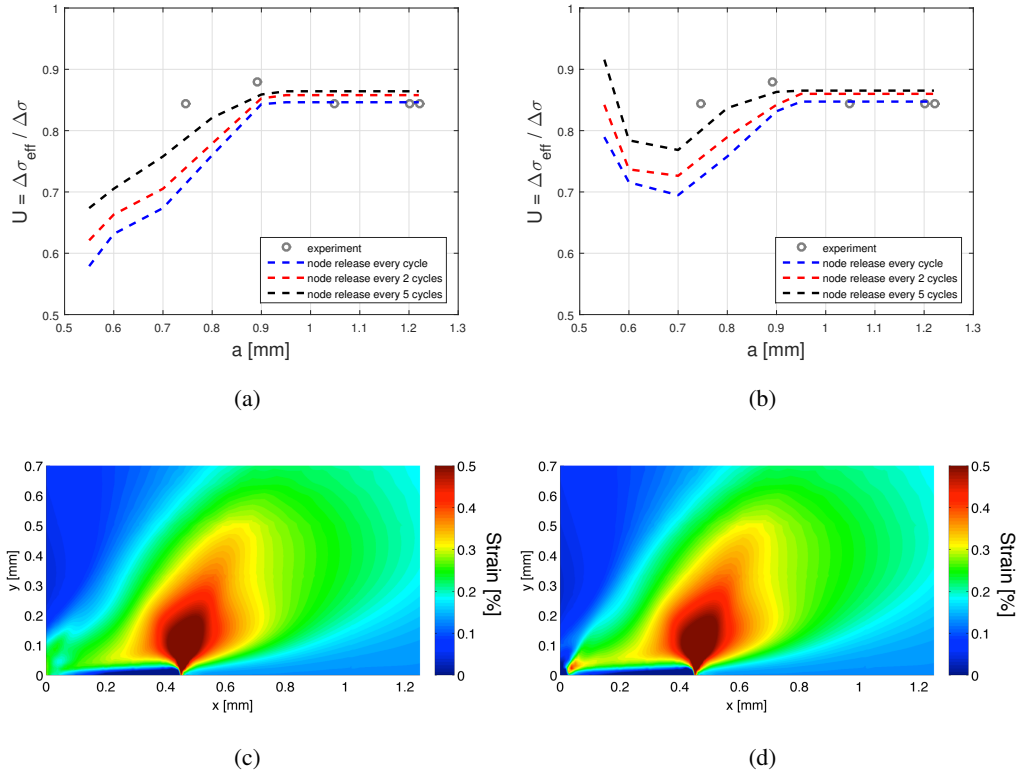

Figure 5.14: *Effects of the notch on the fatigue crack propagation results for [001] single crystal specimen, considering node release at maximum peak: (a) opening values with notch effects; (b) opening values without notch effects; (c) total strain field at peak stress with notch; (d) vertical strain field at peak stress without notch.*

Effect of the node release law on the solution

The effect of choosing node release every cycle, every two cycles or every five cycles, have been previously shown in Fig.s 5.9, 5.10-b and 5.13-b. Fig. 5.9 shows that there are no sensible differences while depicting the vertical strain range at the crack tip; on the other hand the opening values showed that the number of cycles has some influence on them. Considering now the total strain field at crack tip (and not the strain range) of Fig. 5.15, it can be observed that there are several differences in both the plastic wake and the extension of the plastic zone at maximum peak.

These differences can be related to the strains that the model accumulate when the crack is not propagating. Considering Fig. 5.16, the cumulated strain at the crack tip for a fixed crack length (0.9 mm in this case) can be evaluated as the difference between two minimum loads which includes all the cycles between two subsequent node releases (as schematized in Fig. 5.16-a). These results show that the more cycles a crack sees without propagating the more strains it accumulates at the crack tip; this

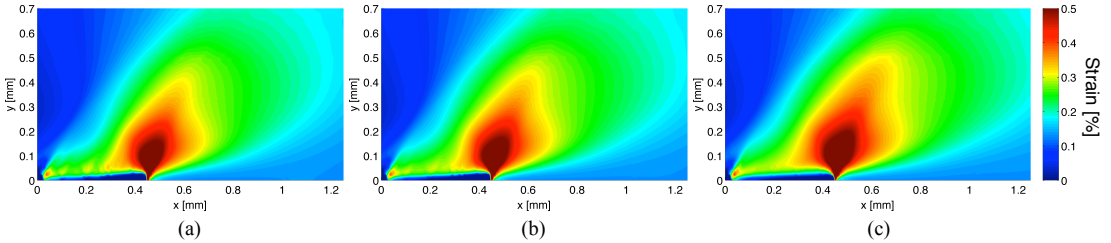

Figure 5.15: *Total strain fields at maximum load for three different node release strategies, considering the pre-cracked model: (a) release every cycle, (b) release every 2 cycles; (c) release every 5 cycles.*

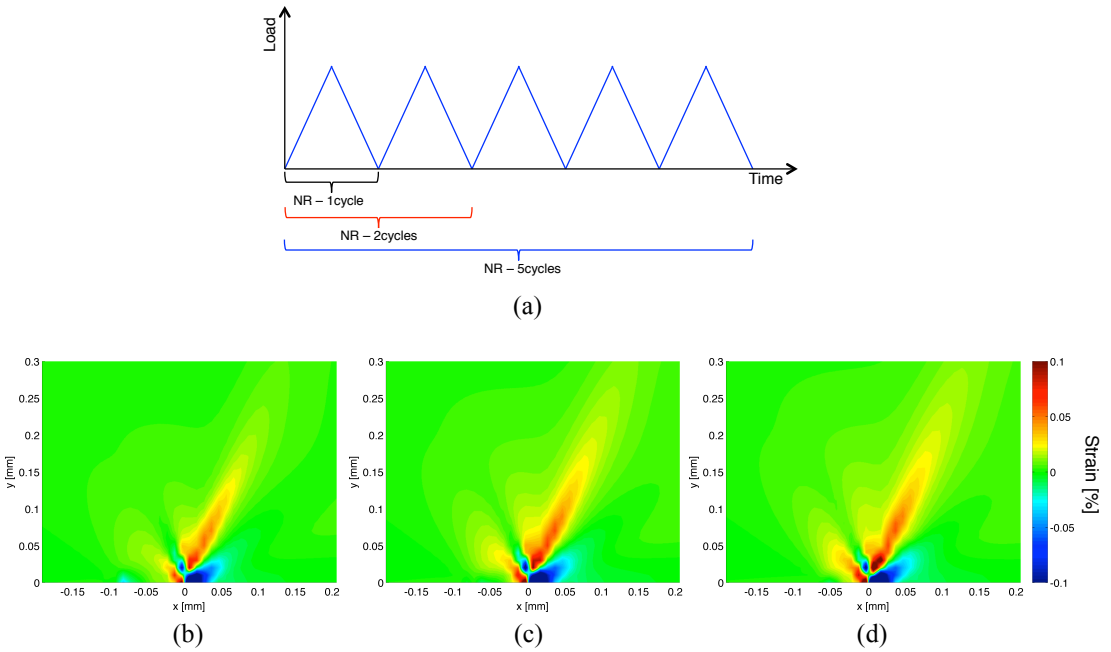

Figure 5.16: *Strain accumulations between two node releases in [001] single crystal crack propagation model. (a) schematic for the evaluation of the cumulated strain between 2 minimum valley for the three node release strategies adopted; (b) cumulated strain when the nodes are released every cycle; (c) cumulated strain when the nodes are released every 2 cycles; (d) cumulated strain when the nodes are released every 5 cycles*

variable accumulation can justify the difference in the predicted plastic wakes and and plastic zones extensions. Considering Fig. 5.15, the differences between the three strain fields are related to this effect.

Application of the results to fatigue life prediction

Numerical results provided an assessment of crack opening levels. These levels, together with a crack propagation curve obtained with a loading ratio of R = 0.7 can be used to develop a propagation model to simulate crack advancement in single crystal specimens. In [14], an experiment on a Haynes 230 SE(B) specimen, a polycrystal, was carried out to evaluate Haynes 230 crack propagation curve in absence of closure. The effects of crack closure were eliminated, in these tests, by applying a high stress ratio, equal to 0.7.

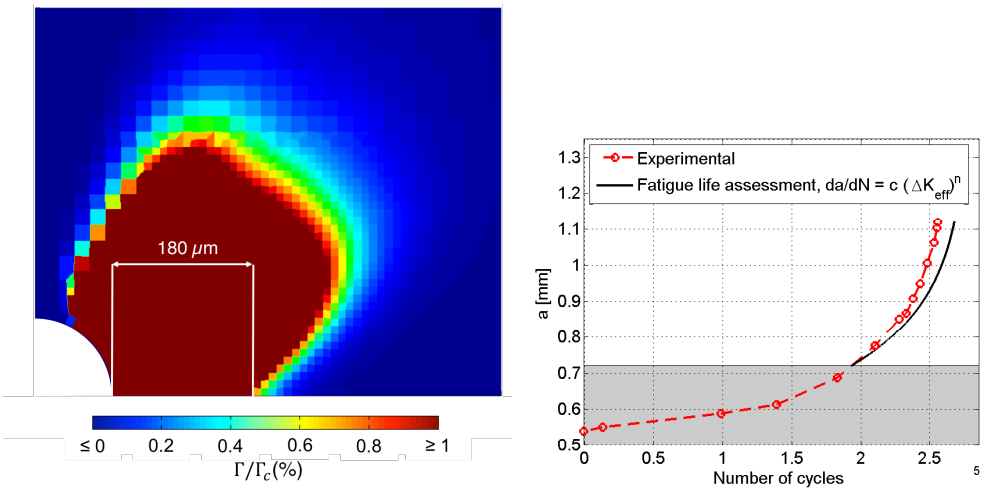

(a) (b)

Figure 5.17: *Fatigue life of [001] single crystal specimen. (a) plastic zone around the notch at the peak stress of the first load ramp; (b) comparison between experimental results and fatigue life estimation curve based on the adopted numerical model.*

In this work, the closure-free propagation curve measured in polycrystal Haynes 230 was employed to assess fatigue life of the single crystal specimen. In order to remove the effects of the notch on propagation, a numerical simulation was performed to evaluate the size of the plastic zone generated at the notch during the first load ramp. The extension of the plastic zone was calculated following Rice's proposal [70]: an element was considered yielded when Γ, the sum of the magnitudes of the slips ($\Gamma = \sum \mid \gamma^s \mid$), was greater than $1\%\ \Gamma_c$, the slip at yielding, calculated as:

$$\Gamma_c = \frac{\tilde{\tau}_{(\epsilon_p=0)}}{\mu_0} \tag{5.1}$$

Numerical results, presented in Fig. 5.17a, show that the plastic zone under monotonic loading around the notch extends by 180 μm. Accordingly, fatigue life was assessed by calculating the number of cycles necessary to propagate the crack from an initial defect

size of 0.68 mm to the final one, measured when the test was ended. An analytical procedure was implemented: the steps computed in each iteration were the following:

- calculation of the $i-th$ effective stress intensity factor range, $\Delta K_{I,eff}$ as:

$$\Delta K_{I,eff} = YU\Delta\sigma\sqrt{\pi a} \tag{5.2}$$

  where Y is a geometric factor that accounts for specimen geometry, calculated as proposed in Eq. (5.3) [111], in which w is specimen width, U is the stress range reduction factor, calculated as proposed in Eq. (5.4), in which σ_{max} and σ_{min} are, respectively, the maximum and the minimum applied stress, and σ_{op} is the crack opening stress, calculated by FEM ($\sigma_{op} = 17.8\%\ \sigma_{max}$).

$$Y = 0.265\,(1 - a/w)^4 + \frac{0.857 + 0.265\,(a/w)}{(1 - a/w)^{3/2}} \tag{5.3}$$

$$U = \frac{\sigma_{max} - \sigma_{op}}{\sigma_{max} - \sigma_{min}} \tag{5.4}$$

- Calculation of the $i-th$ crack increment as:

$$da_i = A\,(\Delta K_{I,eff})^m \cdot d\hat{N},\ \text{with}\ d\hat{N} = 1 \tag{5.5}$$

  where A and m are the constants that describe the closure-free propagation curve presented in [14].

- Crack length update:

$$a_i = a_{i-1} + da_i \tag{5.6}$$

Fatigue life prediction, obtained considering $\Delta K_{\text{I,eff}}$, is represented in Fig. 5.17 by a black continuous line: the assessment provides good estimates. This means that fatigue crack growth, for the single crystals analyzed in this work, is driven by the effective stress intensity factor range and it can be modeled taking into account the effective crack growth curve measured in polycrystals.

5.3 Conclusions

In this chapter, fatigue crack growth was investigated in Haynes 230 single crystal with load direction oriented along [001] crystallographic direction. Crack propagation was characterized experimentally by digital image correlation, the results showed that, in single crystals, the crack stays open for an high portion of the loading cycle: an average stress reduction factor U was observed around 0.85 (loading condition: $\Delta\sigma$ = 133 MPa and R = 0.05).

Experimental results were then compared with those coming from CPFE analyses. Implementing node-release technique for crack advancement, the numerical results were able to confirm the experimental results for crack opening levels.

Single crystal experimental results were also confirmed in terms of crack tip strain fields: excellent agreement was observed both in terms of crack tip plastic zone shape and extension.

Then, numerical results were employed to develop a crack propagation model based on the effective stress intensity factor range. It was found out that fatigue crack growth in single crystal can be described taking into account numerical opening levels and the effective crack propagation curve measured during polycyrstals testing.

CHAPTER 6

Fatigue Crack Growth In Polycrystalline Medium

This chapter focuses on the study of localization around the crack tip in polycrystalline aggregates. The simulations will follow two experimental campaigns: the first considered a quasi-static crack subjected to a tensile load; the second focused on the study of crack propagation mechanisms under different loading conditions. The specimen used for the quasi-static experiment came from the lot 2 of Haynes 230, the same of the specimens studied in Chapter 4, hence the parameters listed in Tab. 4.1 were considered. The specimens used to study crack growth came from a new Haynes 230 lot which exhibits different properties than those of Chapters 3 and 4 (see Fig. 6.1).

This new material comes from a different production process: lot 1 and lot 2 came from laminate sheets, lot 3 came from an extruded bar. Fig. 6.1 shows a comparison between tensile tests conducted on the 3 lots of the material. This new lot exhibits an higher yielding than the previous: 510 MPa against 400 MPa for lot 2 and 353 MPa for lot 1.The fact of considering a whole new behaviour for Haynes 230 implied the necessity to identify a new set of parameters able to describe it. In opposition with the previous chapter, where the identification of the parameters came from the analysis of known structures like single crystals and polycrystalline media (inspected with EBSD for orientations and grains shape), the parameters for the new lot were identified considering random generated structures (no EBSD was performed for the

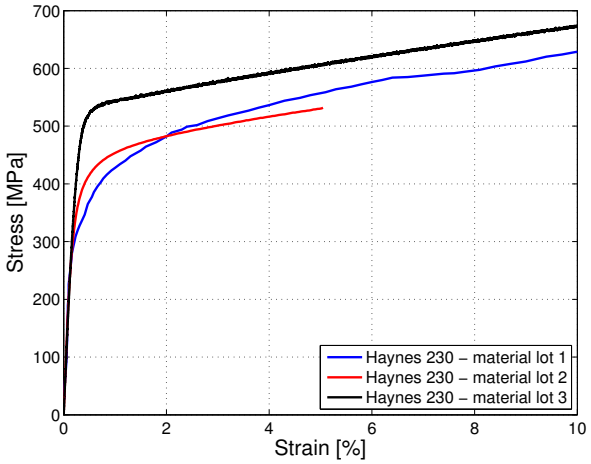

Figure 6.1: *Comparison of the tensile curves of the three considered lot of Haynes 230.*

reference tensile test of lot 3 in Fig. 6.1).

Finally, with the parameters for lot 3, a polycrystalline simulation of fatigue crack growth is provided: in this section the phenomenon is studied considering the medium composed by random generated grains with a crack propagating inside the grains. The results are then compared with the experiments in terms of estimated crack opening levels.

6.1 Experimental Procedure

Two experimental procedure were considered: a quasi-static test was conducted on a pre-cracked specimen to study the strain field generated at the crack tip when the crack does not propagate; fatigue crack propagation tests were performed under various loading conditions to study crack growth mechanisms.

6.1.1 Quasi-Static Crack Test In A Polycrystalline Medium

The setup of the test was constructed with the aim to capture, over a wide surface of the material, the localization of deformation around the crack tip. The geometry of the specimen (Fig. 6.2) was chosen according to the 4 pins grips for Deben micro-testing machine. The notch of 0.5 mm was made by electrical discharge machining. The nominal dimensions of the specimen are 15.5 mm gauge length, a width of 6 mm and a thickness of 2 mm.

At first the specimen was mirror polished and marked (with micro-indentations) to border the area where to perform both EBSD and DIC. The area is confined just ahead of the notch with the marker describing a surface of 1 mm by 0.8 mm. Then the EBSD

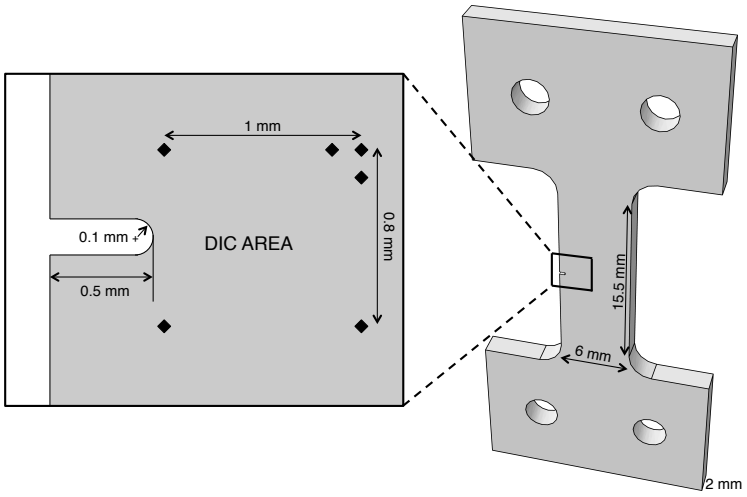

Figure 6.2: *Geometry of the specimen used for the quasi-static crack analysis, details of the area where the EBSD and the DIC were performed.*

scan gave the information about grains location, shapes and orientations as shown in Fig. 6.3.

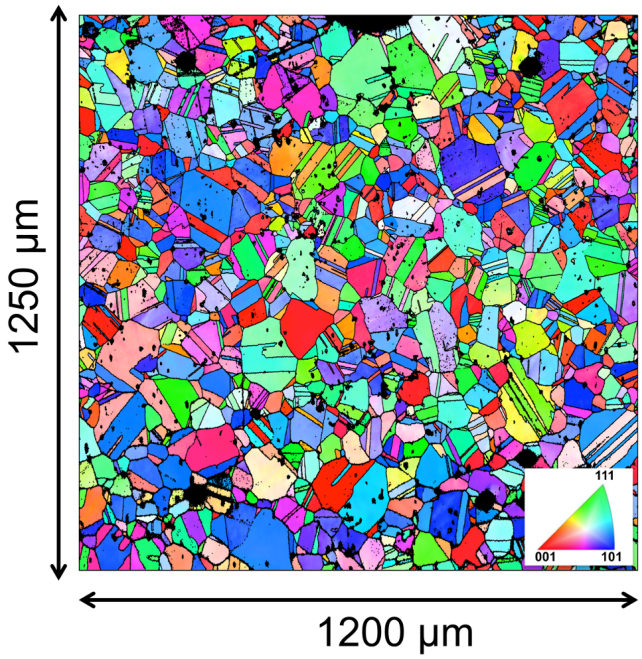

Figure 6.3: *Result of the EBSD scan conducted over the area of interest for the simulation of the quasi-static crack in a polycrystalline medium.*

Since the aim of this chapter is to study the effects of a quasi-static crack, the spec-

imen was compression pre-cracked to obtain a small crack emanating from the notch, this brings to a plastic zones lower than those which could be obtained by pre-cracking in tensile condition. This feature allows to perform the DIC considering that the pre-cracked condition can be considered as a reference for image correlation. The compressive applied load range was 2700 N (between -3000 N and 300 N), this condition ensured a plastic radius at the notch of about 100 μm. The outcome of the pre-cracking procedure is shown in Fig. 6.4, where a 60 μm crack was detected.

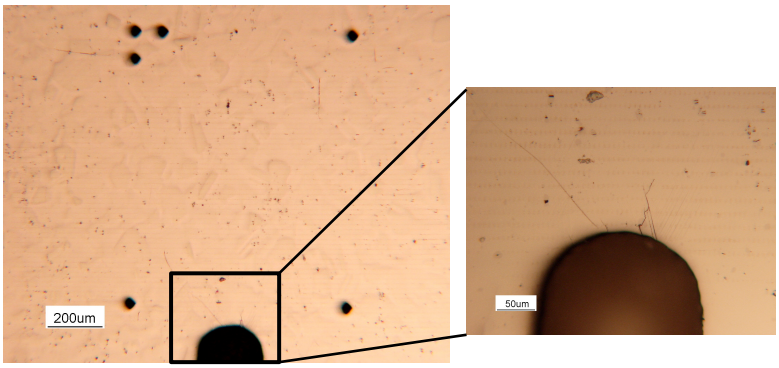

Figure 6.4: *Specimen area after compression pre-cracking: (a) details of the area where EBSD was performed; (b) focus on the generated crack.*

The specimen was then prepared for *ex-situ* high-resolution DIC. In order to perform it, the marked area was prepared. A speckle pattern suitable for high resolution DIC was applied on the surfaces. Images were captured out of the load frame by means of a Carl Zeiss Axio Cam A1 optical microscope, with a resolution of: 0.34 μm/pixel (magnification of 100x). Then, the tested specimen followed the same procedure of capturing images after the test, to perform correlations and obtain details about the strain field. The resulting strain field were then overlapped by the grain boundaries frames obtained by the EBSD using the markers as a reference.

Finally the test was done following the loading path of Fig. 6.5, where two load/unload steps were applied with objective stress intensity factors of 10 MPa$\sqrt{\text{m}}$ at first and 20 MPa$\sqrt{\text{m}}$ then. The image correlation, to determine the strain field around the crack tip, was made by considering the strain range between points 2 and 1: $\Delta\epsilon = \epsilon_2 - \epsilon_1$; this means to consider the strain cumulated by the second load/unload.

The result of this correlation is shown in Fig. 6.6, From this DIC analysis a 40 μm secondary crack which was not visible in Fig. 6.4 can be identified, emanating from the notch and located on its left side; thus it will be included in the following models.

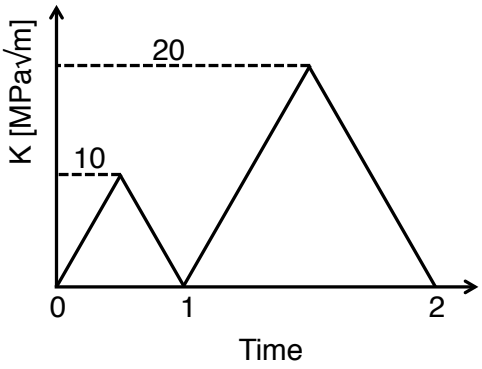

Figure 6.5: *Experimental loading history applied for the study of the material behaviour in presence of a quasi-static crack.*

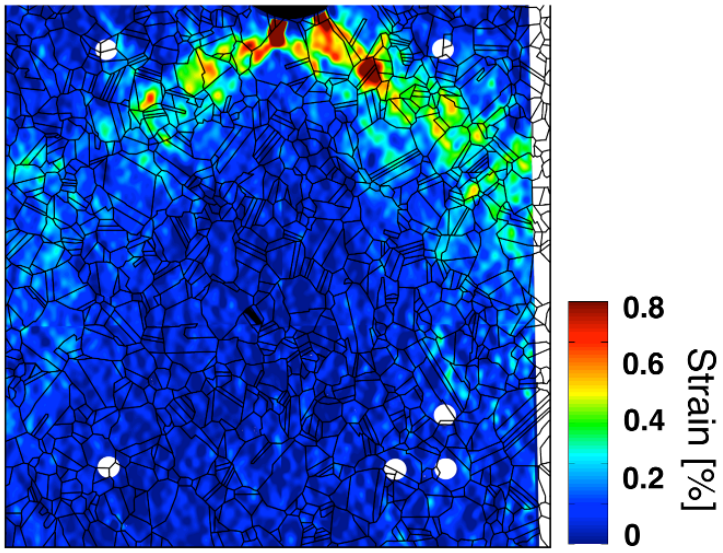

Figure 6.6: *Strain field obtained by DIC for the study of a quasi-static crack in a polycrystalline medium.*

6.1.2 Fatigue Crack Propagation Test In Polycrystalline Medium

Fatigue crack growth experiments were performed on single edge dog-bone specimens. Notches were made by EDM with a geometry shown in Fig. 6.7. The specimen surface preparation followed the single crystal procedure in order to obtain a suitable speckle pattern for DIC. Specimens were cyclically loaded at two different load ratio with the load shown in Tab. 6.1.

As for the single crystals, the COD was measured by means of virtual extensometers: since on the polycrystals the crack propagates under mode I only, the vertical

Table 6.1: *Loading levels for fatigue crack growth test in polycrystalline specimens.*

$\Delta\sigma$	Load Ratio	n. of specimen tested
140	0.1	1
180	0.1	1
240	-1	1

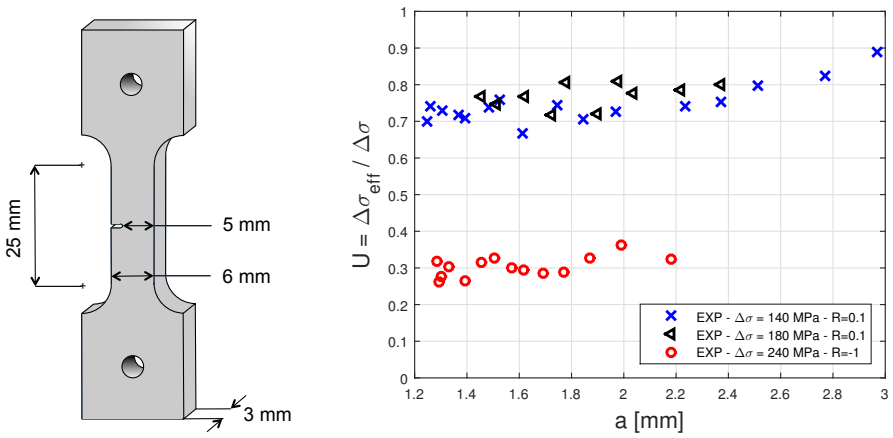

(a) (b)

Figure 6.7: *Specimen geometry for the fatigue crack propagation tests conducted on polycrystalline material (a); results of the experiments in terms of crack opening levels.*

displacement was measured. Fig. 6.7-b shows a summary of the COD results for the experiments: to compare all the load ratio on the same plot, the opening is considered in terms of stress reduction factor U:

$$U = \frac{\Delta\sigma_{\text{eff}}}{\Delta\sigma} = \frac{\sigma_{\max} - \sigma_{\text{op}}}{\sigma_{\max} - \sigma_{\min}} \tag{6.1}$$

More details about the experimental campaign can be found in [14]

6.2 Simulation Of A Quasi-Static Crack In A Polycrystalline Media

The construction of the model required some simplifications:

1. the area modeled by crystal plasticity material is confined around the notch and reproduces the EBSD scan informations (Fig. 6.3);

2. the remaining volume of the specimen is modeled as purely elastic: its main purpose is to transfer the displacement field generated by the loading condition to the CP area. This hypothesis is acceptable since the plastic deformations are confined around the notch;

3. the geometry of the grains in the thickness was considered columnar;

4. the cracks were modeled as uniform through the thickness.

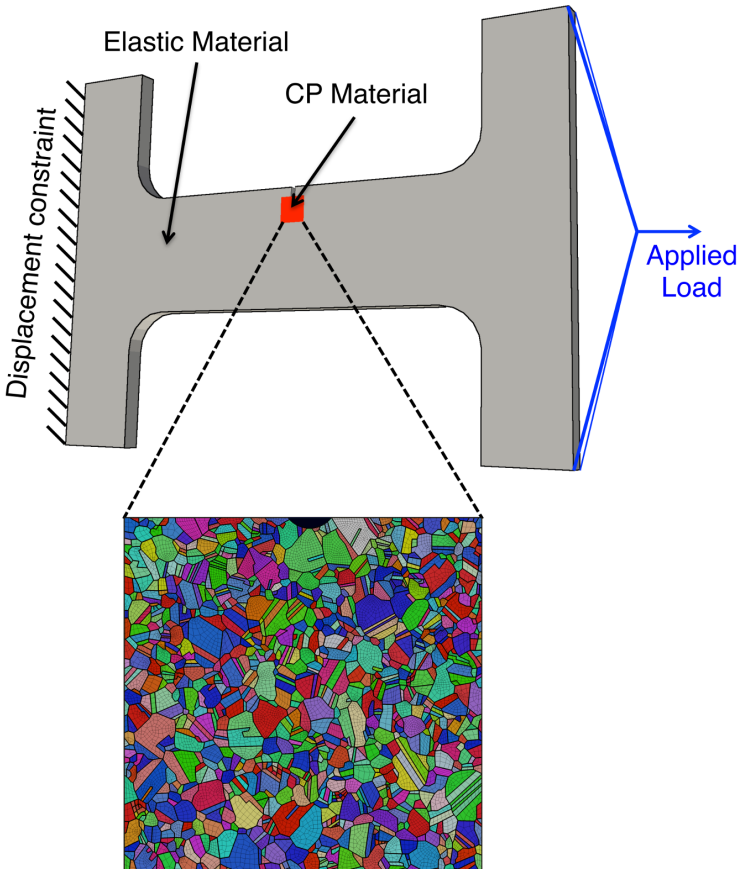

Figure 6.8: *Model of the quasi-static crack experiment: Definition of loading condition and constraints.*

The obtained model is the one showed in Fig. 6.8. Fig 6.8 shows loading and constraint configuration: the load was applied as a force to one node whose displacements were coupled to those of all the nodes belonging to the loaded surface; the opposing face of the specimen was fully constrained in displacement. Fig. 6.8 shows also the detail of the CP area modeled and the applied mesh, here grains geometry and orientations derive from the EBSD. The model in the CP area, counts about 1230 grains; they were modeled by 235000 linear hexahedral elements enhanced with the information about the orientation of the grain they belong.

The loading procedure followed the scheme of Fig. 6.5, a first step at 10 MPa$\sqrt{\text{m}}$ and a second at 20 MPa$\sqrt{\text{m}}$. To have an idea of the differences on the strain field generated by one or two cracks, two simulations were carried out: one considering

only the 60 μm crack and one considering both 60 and 40 μm cracks. Fig. 6.9 shows the outcome of the two simulations: (a) with one crack, (b) with two cracks.

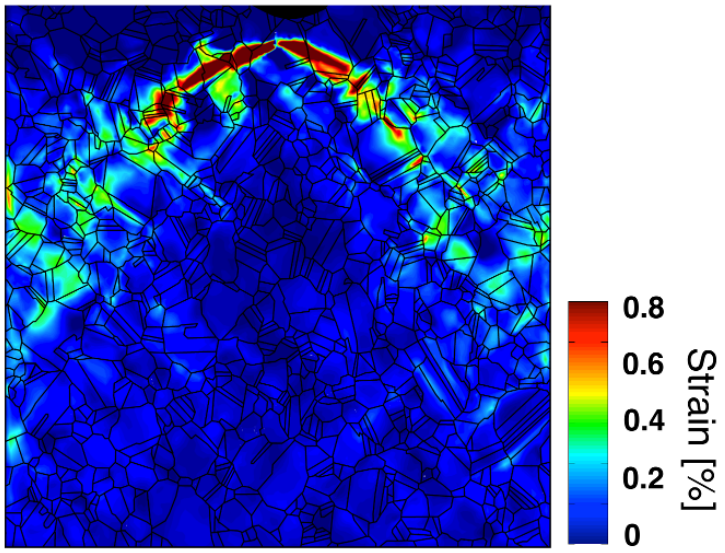

(a)

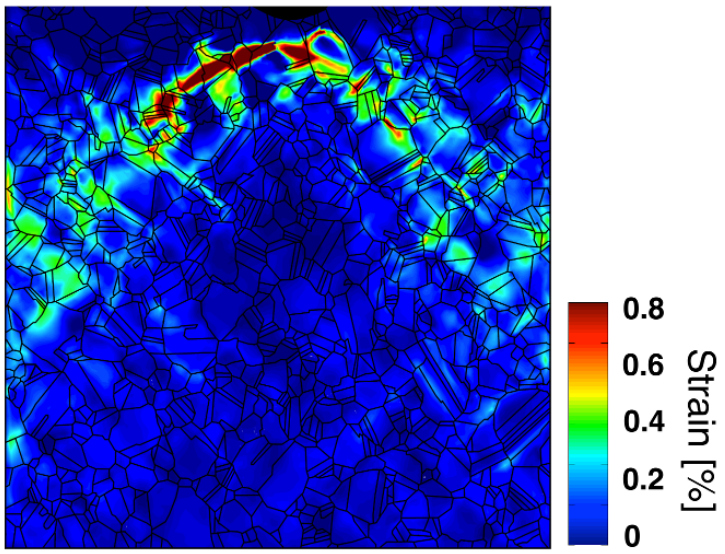

(b)

Figure 6.9: *Study of a quasi-static crack in a polycrystalline medium: strain fields in the loading direction obtained by the numerical simulation of models considering (a) one crack (b) two crack through the thickness.*

The comparison of the two simulations gave an estimation of the area of influence of the secondary crack. It affects only the right side of the notch, the left side is unchanged in the two simulations. Moreover, its area of influence is highly confined in 5-6 grains. Far from its field of influence the strains localization remain unchanged.

The main result coming from the simulation, if compared with DIC (Fig. 6.6), is the agreement with the extension of the strain filed. In addition, most of the grains with active slip systems are reproduced. The main difference with DIC is the presence of high concentrated strains at the crack tips. This feature may be related to the assumption of considering the crack extended flat through the thickness, while in reality compression pre-cracking involves surface regions of the specimen.

Starting from this observation a model where the two cracks were extended in the specimen thickness for only 30 μm (an assumption) was created. This new model, embedding two surface cracks, was then simulated following the loading cycles adopted for the previous.

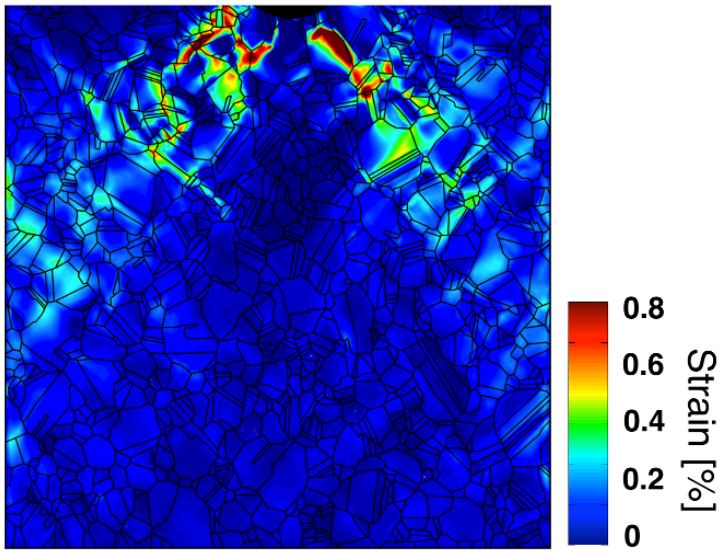

Figure 6.10: *Study of a quasi-static crack in a polycrystalline medium: strain field in the loading direction obtained by the numerical simulation of two surface cracks.*

The result of this last simulation, Fig. 6.10 pointed out the vanishing of the high concentration at the crack tip and several differences in the active grains. The strain field remains approximately similar to itself even if the strains magnitude is highly decreased. This last model pointed out the necessity to know the real crack front and extension to be able to have the most reasonable estimation of the localization occurring through the grains.

6.3 Simulation Of Fatigue Crack Growth In A Polycrystalline Medium

The simulations for crack propagation in polycrystalline media were carried out considering random generated crystalline structures. This assumption was required by the absence of an EBSD analysis on the tested specimens. Thus the numerical results and the experiments were compared only in terms of opening level values.

6.3.1 Analysis Of Random Generated Structures

The identification of the parameters followed the same steps of the previous chapters, an iterative evaluation of the overall behaviour with the aim to reproduce the monotonic curve obtained with the tensile test.

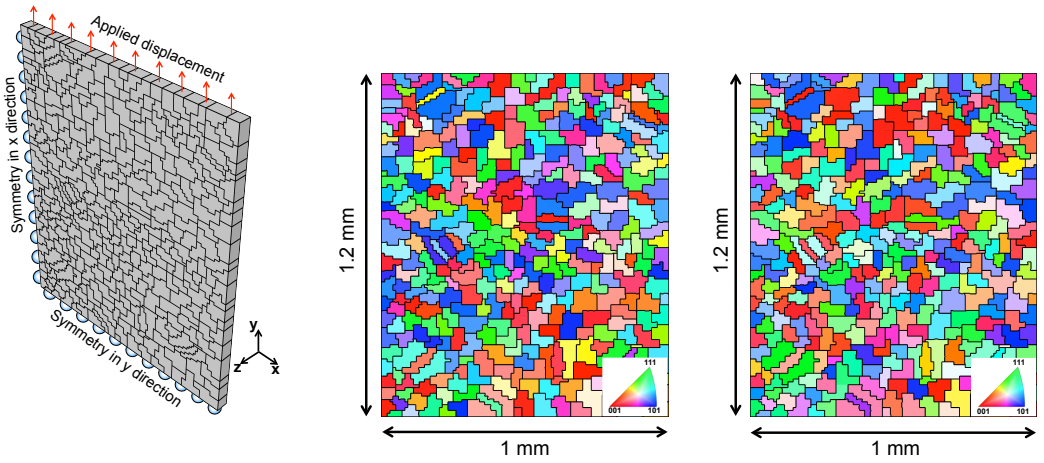

Figure 6.11: *Random generated polycrystalline model for tensile simulation. (a) schematics of the model with loadings and constraints; (b) Two possible orientation maps for the study of the tensile behaviour of the material.*

Fig. 6.11 displays the model used for this section: the main feature is the simplification of the grain boundaries by considering rectangular shaped ones. The adopted model consist of 365 grains contained in an area of 1 mm by 1.2 mm, with an average grain size of 60 μm (this grain dimension will be referred as Medium Grain, later will be considered smaller grains). The model counts 62840 hexahedral linear elements, distributed over 5 layers in the thickness which measures 80 μm. The model shows a double symmetry dictated by the constrains and was displacement loaded along y direction (see Fig. 6.11). For the parameters investigation, different sets of orientation for each grain were taken into account (Fig. 6.11 shows an example of two different EBSD resulting from the random generated orientations for the grains) while the geometry of

the grains was kept the same. Six different orientation maps were considered to evaluate if significant differences may occur in the approximation of the tensile curve. These simulations were used to the estimate the parameters of Tab. 6.3, with a prediction on the tensile test behaviour as shown in Fig. 6.12.

Table 6.2: *Material parameters for the third lot of Haynes 230.*

Property	Description	Value
E	Young's modulus	180 GPa
ν	Poisson's ratio	0.33
μ_0	Shear modulus	92 GPa
b	Burgers Vector	$3.5\,E-7$ mm
$\hat{\tau}_a$	Athermal slip resistence	0 MPa
$\hat{\tau}_y$	MTS strength for intrinsic barrier (yield)	215 MPa
$g_{0,y}$	Normalized activation energy for intrinsic barriers	0.37
q_y	Shape coefficient for intrinsic barriers	1
p_y	Shape coefficient for intrinsic barriers	1.5
$\epsilon_{0,y}$	Strain rate sensitivity for intrinsic barriers	$1\,E9$ s^{-1}
$\hat{\tau}_v$	MTS strength for work hardening	100 MPa
$g_{0,v}$	Normalized activation energy for work hardening	0.5
q_v	Shape coefficient for work hardening	0.9
p_v	Shape coefficient for work hardening	1.0
$\epsilon_{0,v}$	Strain rate sensitivity for work hardening	$1\,E7$ s^{-1}
ϑ_0	Initial hardening slope	282 MPa
k_0	Geometric hardening parameter	2

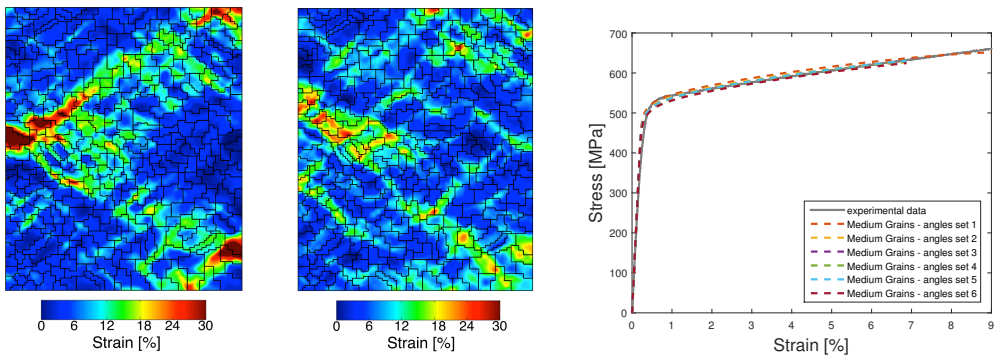

(a) (b) (c)

Figure 6.12: *Random generated polycrystalline tensile results: (a) strain localization for the first set of grains orientation; (b) strain localization for the second set of grains orientation; (c) comparison between the overall behaviour of all the simulations and the experiment.*

The same figure shows also two outcomes of the strain localization for 2 of the 6 models considered, showing that different orientations, but the same grain shape, may

lead to completely different solutions in terms of concentration of deformations.

Before moving to the analysis of the crack propagation, it would be helpful to consider how the shape of the grains and their dimension may affect the results.

Grain Boundaries Shape

The assumption made in this section is to consider rectangular grain boundaries instead of the usual smooth shape. The effects of this hypothesis can be evaluated considering 2 models: the first with smooth grains and the other with squared grains. Both models contained the same number of grains (about 120), with the same orientations. Those two models were simulated under a monotonic loading to capture any possible difference.

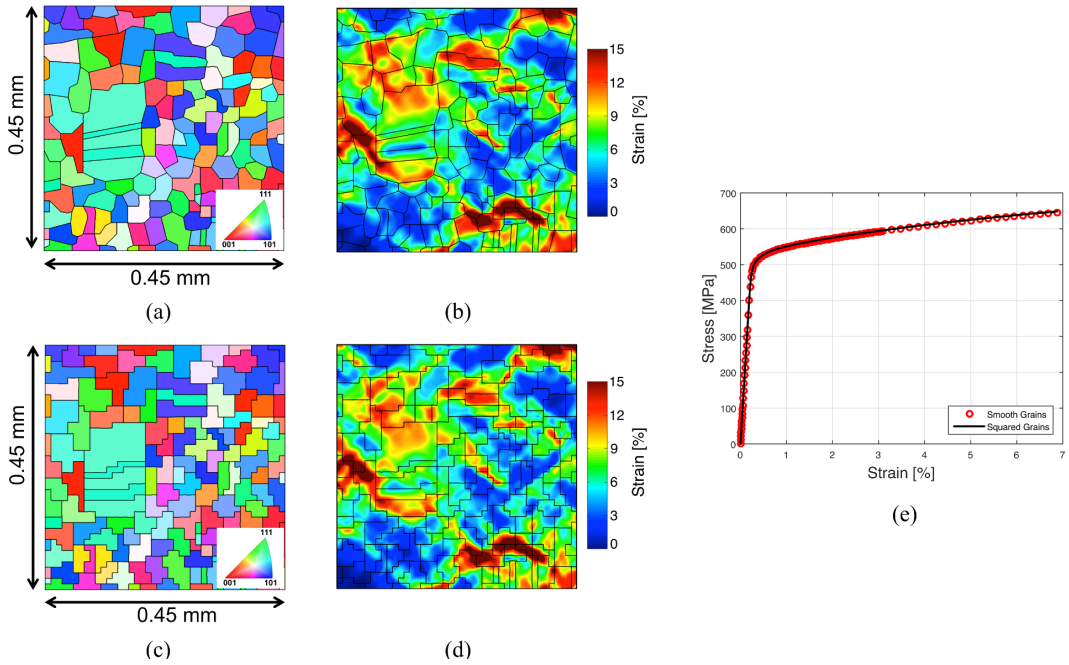

Figure 6.13: *Randomly generated polycrystal: evaluation of the implication of considering squared grain boundaries. (a) orientations map for grains with smooth boundaries; (b) strain field localization for the model considering smooth grain boundaries; (c) orientations map for grains with squared boundaries; (d) strain field localization for the model considering squared grain boundaries; (e) comparison of the overall behaviour of the two types of grain models.*

Fig. 6.13 shows the two models and the results obtained by their simulations. It can be noticed that both produce the same results not only on the overall behaviour of the tensile test, but also in strain localization. In fact no difference can be detected in the actives grains or in stain concentrations. These results led to the conclusions that

the assumption of considering squared grains is acceptable and can be applied in the following analyses.

Grains Dimensions

The last part of this section aims to evaluate if the dimension of the grains may have an effect on the predicted tensile curve. The models investigated till now were considering an average grain size of 60 μm, the new model was created reducing the dimension to an average grain size of 40 μm.

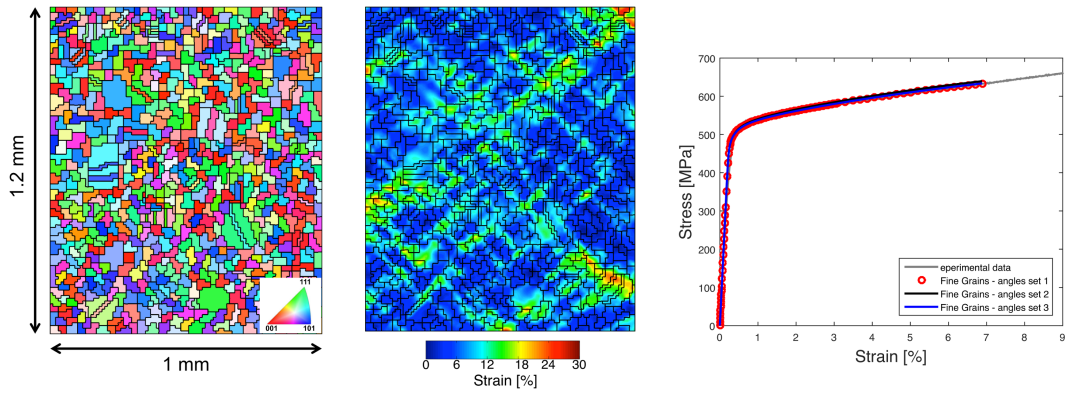

(a) (b) (c)

Figure 6.14: *Randomly generated polycrystal: grain size reduction effects. (a) grains map; (b) strain field localization; (c) comparison between the overall behaviour of the simulations and the experiment.*

Fig. 6.14-a shows the new map of grains, modeled over a surface of 1 mm by 1.2 mm (as the previous models), which consists of 60570 hexahedral linear elements distributed over 5 layers in the thickness (the thickness is 80 μm). Different grain orientations were considered, 3 in this case, and the results obtained simulating the tensile test are summarized in Fig. 6.14-b,c. From the results it was observed that the overall behaviour is well captured, as it was in Fig. 6.12 for the models with average grain size of 60 μm.

Finally for crack propagation analysis both grain sizes models will be considered, to see if they may have any effect in predicting crack opening levels.

6.3.2 Crack Propagation In Random Polycrystalline Structures

The simulation of crack propagation in a random generated polycrystalline matrix under mode I loading, required some assumptions:

1. the specimens were modeled with a double symmetry, so only one quarter of the

real specimen was modeled, and the crack propagates along a symmetry plane;

2. the grains were extended in the thickness as columnar;

3. the presence of the crack localizes the plastic deformation in a small area ahead of the crack tip, meaning that only that area can be modeled with elements described by CP constitutive equation. The remaining volume of the specimen was modeled as purely elastic with the only aim to transfer the displacement field at the boundary of the grains region;

4. the region containing the grains was located far from the notch, with the crack that starts to propagate from the boundary of the CP area: this allow to neglect the effects of the notch and its inclusion in the geometry of the model can be avoided.

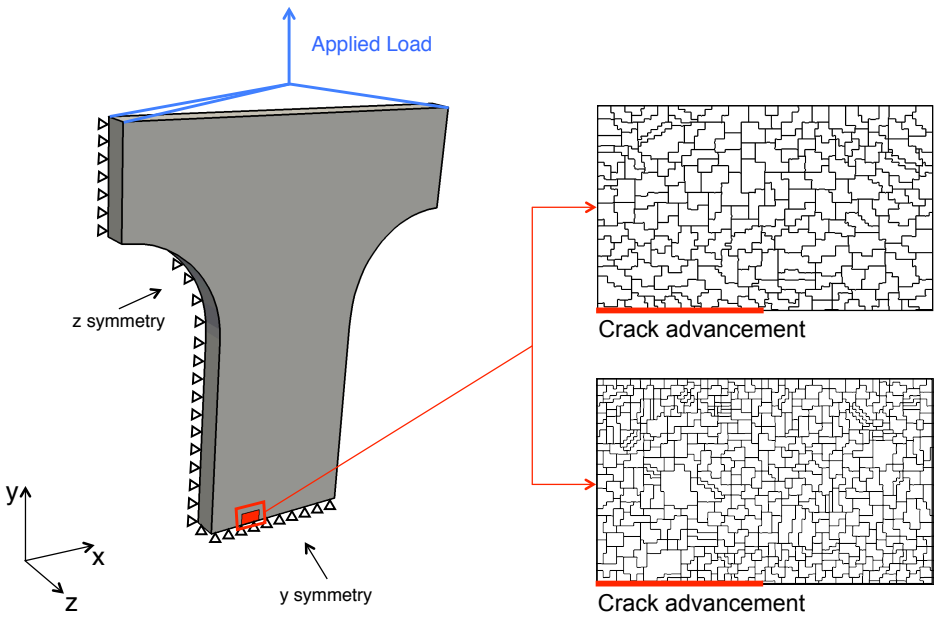

Figure 6.15: *Crack propagation model for random generated polycrystalline structure: model loading condition and symmetry constraint; identification of the volume modeled with CP type elements; definition of the two possible polycrystalline maps where the crack propagates.*

Following these simplifications, the model of Fig. 6.15 was created: in this figure the two adopted maps for the simulation are shown. As it can be seen the areas which contain the grains have dimensions of 0.6 mm by 1 mm, where the first counts 182 grains and the second one 425 grains. The crack starts with a length of 1.75 mm and advances with node release technique every two cycles by steps of 10 μm, which is the

dimension of the elements along the crack front (see section 5.2 for more details on node release technique). The crack was propagated till reaching the final length of 2.23 mm. The evaluation of the COD was made at three discrete crack length: 1.84 mm, 1.97 mm and 2.23 mm.

Table 6.3: *Results of the polycrystalline crack growth simulations in terms of σ_{op} as a function of: loading condition, model and crack length.*

Loading condition	Model	Opening for a = 1.84 mm	Opening for a = 1.97 mm	Opening for a = 2.23 mm
$\Delta\sigma$ = 140 MPa, R = 0.1	182 grains - angle set 1	59 MPa	68.5 MPa	67.8 MPa
$\Delta\sigma$ = 140 MPa, R = 0.1	182 grains - angle set 2	49 MPa	66.4 MPa	60 MPa
$\Delta\sigma$ = 140 MPa, R = 0.1	182 grains - angle set 3	47.1 MPa	73.4 MPa	61.8 MPa
$\Delta\sigma$ = 140 MPa, R = 0.1	425 grains - angle set 1	46.7 MPa	66.1 MPa	59.3 MPa
$\Delta\sigma$ = 180 MPa, R = 0.1	182 grains - angle set 1	56 MPa	82.4 MPa	79.6 MPa
$\Delta\sigma$ = 240 MPa, R = -1	182 grains - angle set 1	72.2 MPa	79.7 MPa	79.2 MPa

As shown in Tab. 6.1, the experiments on polycrystals were performed with two loading ratios and three stress ranges: 1) $\Delta\sigma$ = 140 MPa at R = 0.1; 2) $\Delta\sigma$ = 180 MPa at R = 0.1; 3) $\Delta\sigma$ = 240 MPa at R = -1. Simulations were done to have predictions for the three cases and the results in terms of opening stress value (σ_{op}) are registered for the three crack lengths in Tab. 6.3. For the first loading condition, four simulations were performed: 3 with the model containing 182 grains and 1 with the one containing 425 grains. Since the results of this four simulations were close enough, it was possible to assume the possibility to perform the analysis at the 2 remaining load levels with the model with bigger grains. This justifies the single values for the second and the third loading condition in Tab. 6.3.

Considering now the mean values for each level, the stress reduction factor U can be estimated as 0.68 for loading case 1, 0.71 for case 2 and 0.34 for case 3. These three constant values can be compared with the experimental results, this comparison is shown in Fig. 6.16. The outline of this figure is that the models were able to capture the experimental results even without exactly reproducing the local microstructures.

Further details on the simulations can be obtained considering stresses and strains localization. Fig. 6.17-a,b show an example of the residual strain fields at the end of crack propagation for both small and big grains: it is possible to observe that along crack flanks there is a no uniform accumulation, strains concentrate on the active slip planes over several grains. Then Fig. 6.17-c,d represent the stress field at the end of the simulation, showing the extension of the plastic wake that generated from the 2.23 mm crack propagation. Those two results have no direct correspondence with the experiments, since real grains geometry and orientations are unknown.

The models considered till here rely on the adopted CP code, to establish a comparison with simulations that adopt established material constitutive equations, the

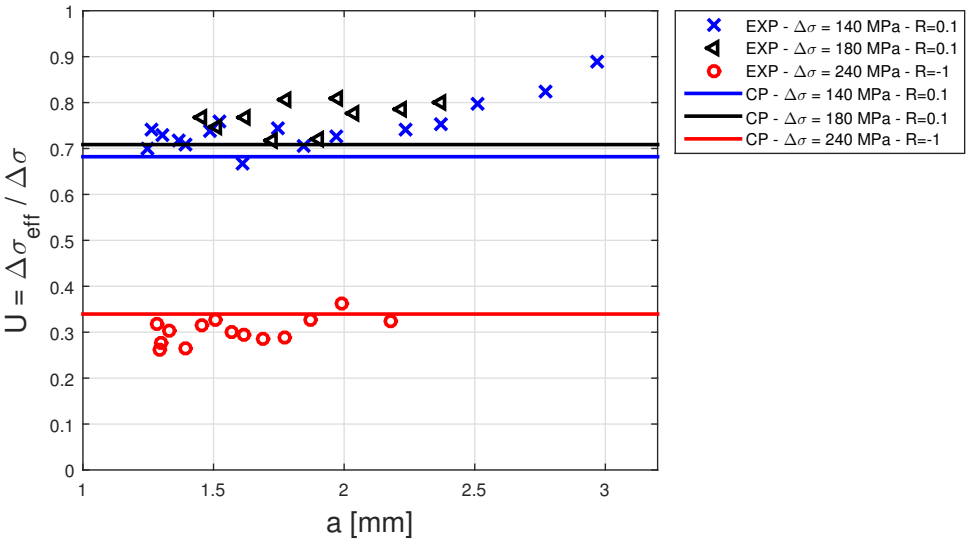

Figure 6.16: *Polycrystalline medium: comparison between the experimental opening level and those predicted by the simulations.*

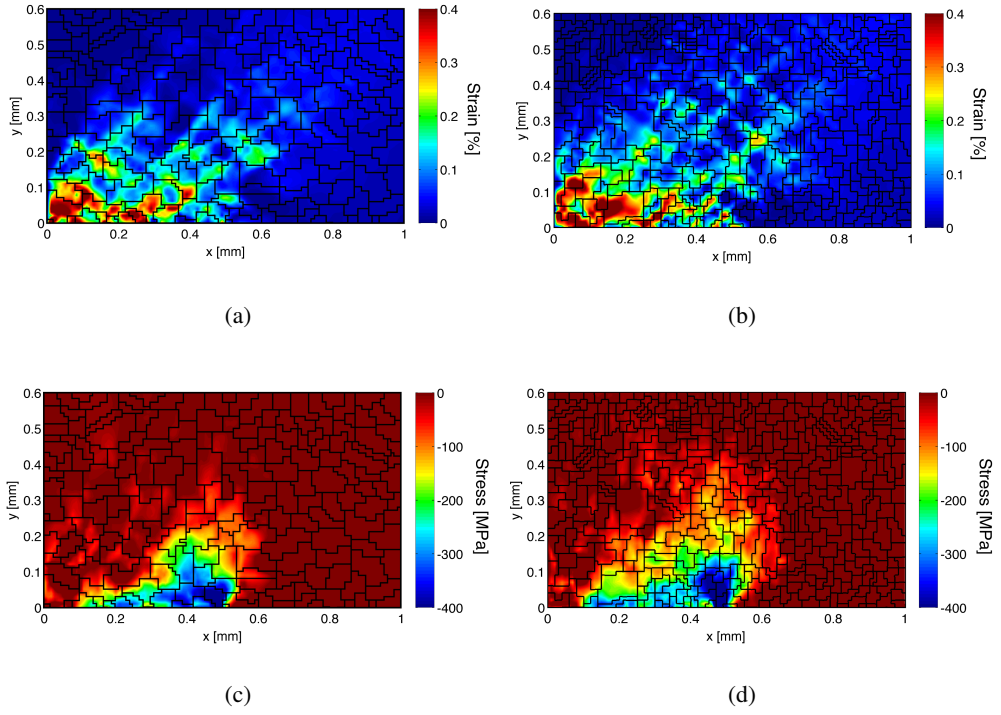

Figure 6.17: *Residual strains and stresses after crack propagation in randomly generated polycrystals. Model with 182 grains: (a) strain field, (c) stress field. Model with 425 grains: (b) strain field, (d) stress field.*

ABAQUS plasticity model was taken into account [112]. The parameters were estimated from LCF tests performed at various $\Delta\epsilon$ and load ratios, obtaining the constants of Tab. 6.4: only the kinematic parameters were taken into account avoiding the definition of the cyclic hardening parameters, doing so the stabilized hysteresis cycle is immediately reached.

Table 6.4: *Parameters for ABAQUS combined plasticity model.*

E [MPa]	ν	$\sigma\|_0$	C_1 [MPa]	γ_1	C_2 [MPa]	γ_2
200470	0.3	179	323959	5000	65654	1000
C_3 [MPa]	γ_3	C_4 [MPa]	γ_4	Q_∞ [MPa]	b	
64904	333	9938	1	0	0	

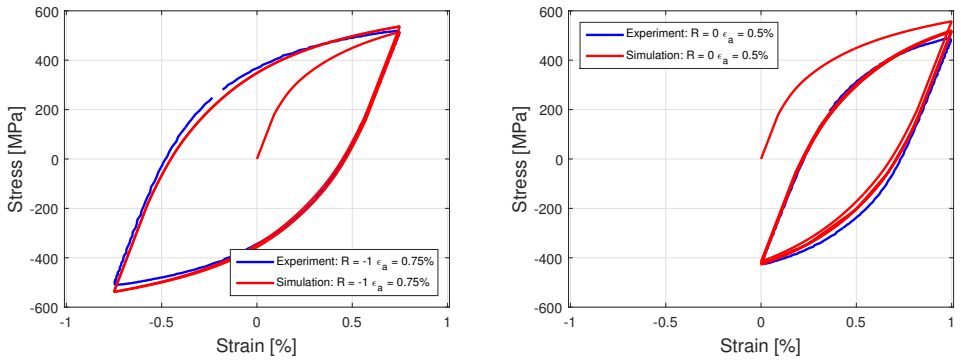

(a) (b)

Figure 6.18: *validation of the parameters of Tab. 6.4 in comparison with experimental LCF stabilized cycles for: (a) ϵ_a = 0.75% at R = -1 and (b) ϵ_a = 0.5% at R = 0.*

Fig. 6.18 shows the results of the parameters identification with simulations of the stabilized cycles for two loading conditions (ϵ_a = 0.75% at R = -1 and ϵ_a = 0.5% at R = 0) considering the model as a cubic RVE of 1000 hexahedral linear elements, the load was applied as a cyclic displacement. To simulate crack propagation the same geometry was adopted of the previous models (see Fig. 6.15) under the same loading and constraint conditions. In Fig. 6.19 the opening levels are registered obtained for the three loadings and the map of the residual strains at the end of the propagation for the $\Delta\sigma$ = 140 MPa and R = 0.1 case. The opening values (in terms of U) predicted by ABAQUS are higher if compared with the crystal plasticity ones. This can be attributed to the residual strain localizations which for the grains occur on critical planes while in the other model is homogeneously distributed along the crack flank.

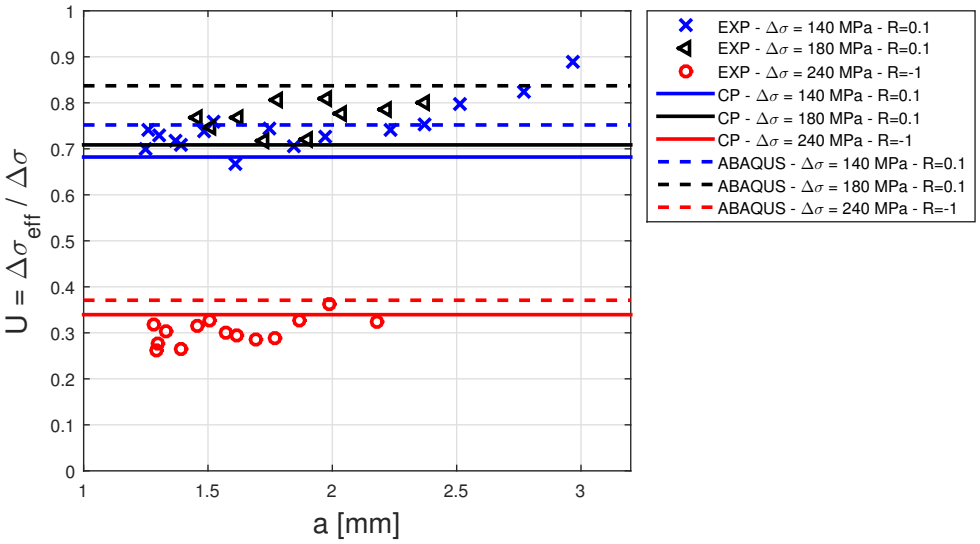

(a)

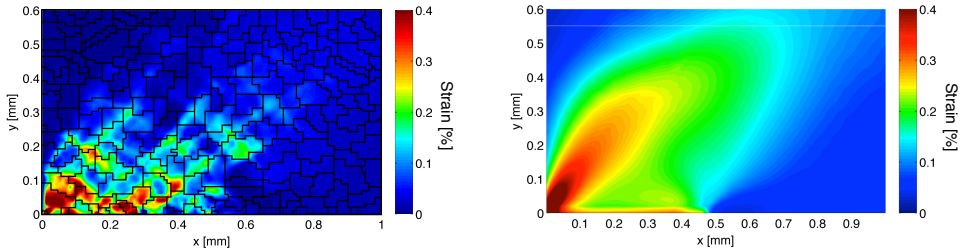

(b) (c)

Figure 6.19: *Comparison between the CP estimated values and the ABAQUS model ones: (a) Crack opening prediction; (b-c) comparison between the residual strain fields, (b) CP and (c) ABAQUS.*

6.4 Conclusions

This chapter applied crystal plasticity code at first to predict the extension of the residual plastic zone in presence of a non-propagating crack and then to estimate the crack opening levels with a fatigue crack growth simulation. The results of the quasi-static simulation showed a good agreement with the experiment proving that the crystal plasticity code is able to describe the strain localization across a wide number of grains in presence of a singularity like a crack. It also pointed out that some of the assumptions in constructing the model are acceptable: the definition of a crystal plasticity volume

embedded in an elastic matrix; the extension of the grains as columnar in the thickness. The same assumptions were considered for the crack growth model.

The construction of the crack propagation model required at first the identification of new parameters. The adoption of random generated structures allowed the identification of crystal plasticity model parameters. In addition the hypothesis of modeling the grains with squared boundaries was proven to be acceptable. For the crack growth simulations the comparison with the experiments was possible only in terms of crack opening levels, since the adopted crystals structures were randomly generated. The results showed an excellent agreement with the tests, being able to predict the opening under various loading conditions.

The last comparison is between the predicted opening levels for single crystal and polycrystal. The single crystal results, under loading condition of $\Delta\sigma$ = 133 MPa and R = 0.05, predicted a stress reduction factor U = 0.85. The polycrystal results, for the closest loading condition ($\Delta\sigma$ = 140 MPa and R = 0.1), predicted a stress reduction factor U = 0.68. These results implies that in polycrystals the crack stays closed for an higher portion of the loading cycle.

CHAPTER 7

Concluding Remarks

The continuous need to improve the knowledge on material behaviour and provide more reliable models to correctly predict stresses and deformations inside a component, requires the adoption of numerical models along experimental procedures. This work presented the adoption of an open source crystal plasticity finite element code (Warp3D) to the study of a Ni-based super-alloy, Haynes 230. Its predictions were compared with the results coming from DIC in the study of phenomena at different length scales.

Chapter 3 described the first procedure adopted in estimating CP model parameters, starting from single crystal tests and then applying them to a polycrystalline simulation. The results obtained by the simulation of a 700^{o}C tensile test revealed an excellent agreement between the overall behaviour of 3 polycrystalline models and the experiment. As for the description of the strain field, the primary analyses had proven a good agreement which was improved by the introduction of carbides inclusion in the polycrystalline matrix.

Chapter 4 described the construction of a model to predict ratcheting in a polycrystalline medium. In this chapter a second procedure adopted in estimating the crystal plasticity parameters was also illustrated, which relies in the analysis of a polycrystalline tensile test conducted at room temperature. Then, with the new set of parame-

ters, the attention moved to the study of the material behaviour under repeated loads. The prediction of the localization of strains for a 10 cycles ratcheting test revealed a good agreement both in the identification of grains activation and in accumulation of local deformations with increasing number of cycles.

Chapter 5 introduced the topic of fatigue crack growth simulations focusing on single crystals specimens. The results were able to accurately describe the strain localization and the displacement field at the crack tip. In addition the evaluation of the crack opening provided an excellent agreement with experimental measurements. Finally, the application of the results to a model for crack propagation based on the effective stress intensity factor range showed that fatigue crack growth in single crystal may be derived starting from polycrystalline data.

Chapter 6 provided a first assessment on the description of the strain field deriving from a quasi-static crack in a polycrystalline medium. This simulation provided good results in identifying the extension of the plastic zone. It also pointed out that for a most accurate description of the local behaviour a correct knowledge of the crack shape is needed. Then numerical simulations of fatigue crack growth in polycrystalline specimens were done considering random generated structures. At first the third approach to identify crystal plasticity material parameters was investigated: the fitting of the experimental tensile curve was done by means of simulations of random generated grains structures. Following, a model for crack growth in a polycrystalline media was implemented. The comparison between the crack opening levels measured experimentally and the numerical solution showed excellent prediction capabilities.

Further developments, starting from the obtained results, could be in the application of the crystal plasticity simulations to crack nucleation models based on energetic approach. Then, once a crack is detected, the crack propagation can be studied deriving its driving forces from the simulations (the models had proven high capabilities in predicting opening levels).

Other improvements can be related to the modeling features, most of the presented models rely on the definition of columnar grains along the thickness. The definition of real grain shapes in the thickness may provide improvements in the identification of strain localization. If the real grains shape can't be modeled, statistical definition of the grains, starting from the superficial EBSD, may be implemented, such modeling has already proven good capabilities in [113].

Bibliography

[1] RC Reed. *The superalloys: fundamentals and applications*. Cambridge university press, 2008.

[2] D Furrer and H Fecht. Ni-based superalloys for turbine discs. *JOM*, 51(1):14–17, 1999.

[3] P Caron and T Khan. Evolution of ni-based superalloys for single crystal gas turbine blade applications. *Aerospace Science and Technology*, 3(8):513–523, 1999.

[4] A Musienko, A Tatschl, K Schmidegg, O Kolednik, R Pippan, and G Cailletaud. Three-dimensional finite element simulation of a polycrystalline copper specimen. *Acta materialia*, 55(12):4121–4136, 2007.

[5] MA Sutton, JJ Orteu, and H Schreier. *Image correlation for shape, motion and deformation measurements: basic concepts, theory and applications*. Springer Science & Business Media, 2009.

[6] W Abuzaid, H Sehitoglu, and J Lambros. Plastic strain localization and fatigue micro-crack formation in hastelloy x. *Materials Science and Engineering: A*, 561:507–519, 2013.

[7] JD Carroll, W Abuzaid, J Lambros, and H Sehitoglu. High resolution digital image correlation measurements of strain accumulation in fatigue crack growth. *International Journal of Fatigue*, 57:140–150, 2013.

[8] B Healy, A Gullerud, K Koppenhoefer, A Roy, S RoyChowdhury, J Petti, et al. Warp3d: 3-d nonlinear finite element analysis of solids for fracture and fatigue processes. Technical report, Tech rep. University of Illinois at Urbana-Champaign, 2014.

[9] Haynes online literature - haynes 230 alloy brochure. `http://www.haynesintl.com`. Accessed: 2015-09-30.

[10] DW Gross, K Nygren, GJ Pataky, J Kacher, H Sehitoglu, and IM Robertson. The evolved microstructure ahead of an arrested fatigue crack in haynes 230. *Acta Materialia*, 61(15):5768–5778, 2013.

[11] GJ Pataky, H Sehitoglu, and HJ Maier. High temperature fatigue crack growth of haynes 230. *Materials Characterization*, 75:69–78, 2013.

[12] PK Liaw, TR Leax, RS Williams, and MG Peck. Influence of oxide-induced crack closure on near-threshold fatigue crack growth behavior. *Acta Metallurgica*, 30(12):2071–2078, 1982.

[13] S Rabbolini, GJ Pataky, H Sehitoglu, and S Beretta. Fatigue crack growth in haynes 230 single crystals: an analysis with digital image correlation. *Fatigue & Fracture of Engineering Materials & Structures*, 38(5):583–596, 2015.

[14] S Beretta, S Rabbolini, and A Di Bello. Multi-scale crack closure measurements with digital image correlation on haynes 230. *Frattura ed Integrita' Strutturale*, (33):174, 2015.

[15] K Mo, G Lovicu, H Tung, X Chen, and JF Stubbins. High temperature aging and corrosion study on alloy 617 and alloy 230. *Journal of Engineering for Gas Turbines and Power*, 133(5):052908, 2011.

[16] A Thakur, KS Vecchio, and S Nemat-Nasser. Bauschinger effect in haynes 230 alloy: Influence of strain rate and temperature. *Metallurgical and Materials Transactions A*, 27(7):1739–1748, 1996.

[17] GJ Pataky, H Sehitoglu, and HJ Maier. Creep deformation and mechanisms in haynes 230 at 800 c and 900 c. *Journal of Nuclear Materials*, 443(1):484–490, 2013.

[18] GJ Pataky and H Sehitoglu. Experimental methodology for studying strain heterogeneity with microstructural data from high temperature deformation. *Experimental Mechanics*, 55(1):53–63, 2015.

[19] HJ Bunge. Texture analysis in materials science'; 1982. *London, Butterwoths*.

[20] AJ Schwartz, M Kumar, BL Adams, and DP Field. *Electron backscatter diffraction in materials science*, volume 2. Springer, 2009.

[21] RJ Asaro. Micromechanics of crystals and polycrystals. *Advances in applied mechanics*, 23:1–115, 1983.

[22] CA Bronkhorst, SR Kalidindi, and L Anand. Polycrystalline plasticity and the evolution of crystallographic texture in fcc metals. *Philosophical Transactions of the Royal Society of London A: Mathematical, Physical and Engineering Sciences*, 341(1662):443–477, 1992.

[23] F Roters, P Eisenlohr, L Hantcherli, DD Tjahjanto, TR Bieler, and D Raabe. Overview of constitutive laws, kinematics, homogenization and multiscale methods in crystal plasticity finite-element modeling: Theory, experiments, applications. *Acta Materialia*, 58(4):1152–1211, 2010.

[24] G Cailletaud, S Forest, D Jeulin, F Feyel, I Galliet, V Mounoury, and S Quilici. Some elements of microstructural mechanics. *Computational Materials Science*, 27(3):351–374, 2003.

[25] D Peirce, RJ Asaro, and A Needleman. An analysis of nonuniform and localized deformation in ductile single crystals. *Acta metallurgica*, 30(6):1087–1119, 1982.

[26] R Becker, JF Butler, H Hu, and LA Lalli. Analysis of an aluminum single crystal with unstable initial orientation (001)[110] in channel die compression. *Metallurgical Transactions A*, 22(1):45–58, 1991.

[27] B Peeters, SR Kalidindi, P Van Houtte, and E Aernoudt. A crystal plasticity based work-hardening/softening model for bcc metals under changing strain paths. *Acta materialia*, 48(9):2123–2133, 2000.

[28] FPE Dunne, D Rugg, and A Walker. Lengthscale-dependent, elastically anisotropic, physically-based hcp crystal plasticity: application to cold-dwell fatigue in ti alloys. *International Journal of Plasticity*, 23(6):1061–1083, 2007.

[29] O Diard, S Leclercq, G Rousselier, and G Cailletaud. Evaluation of finite element based analysis of 3d multicrystalline aggregates plasticity: Application to crystal plasticity model identification and the study of stress and strain fields near grain boundaries. *International Journal of Plasticity*, 21(4):691–722, 2005.

[30] P Thamburaja and L Anand. Polycrystalline shape-memory materials: effect of crystallographic texture. *Journal of the Mechanics and Physics of Solids*, 49(4):709–737, 2001.

[31] Surya R Kalidindi. Incorporation of deformation twinning in crystal plasticity models. *Journal of the Mechanics and Physics of Solids*, 46(2):267–290, 1998.

[32] L St-Pierre, E Héripré, M Dexet, J Crépin, G Bertolino, and N Bilger. 3d simulations of microstructure and comparison with experimental microstructure coming from oim analysis. *International Journal of Plasticity*, 24(9):1516–1532, 2008.

[33] F Barbe, L Decker, D Jeulin, and G Cailletaud. Intergranular and intragranular behavior of polycrystalline aggregates. part 1: Fe model. *International journal of plasticity*, 17(4):513–536, 2001.

[34] F Barbe, S Forest, and G Cailletaud. Intergranular and intragranular behavior of polycrystalline aggregates. part 2: Results. *International Journal of Plasticity*, 17(4):537–563, 2001.

[35] M Messner. *Micromechanical models of delamination in aluminum-lithium alloys*. PhD thesis, University of Illinois at Urbana-Champaign, 2014.

[36] K Zhang, JW Ju, Z Li, Y Bai, and W Brocks. Micromechanics based fatigue life prediction of a polycrystalline metal applying crystal plasticity. *Mechanics of Materials*, 85:16–37, 2015.

[37] N Zaafarani, D Raabe, RN Singh, F Roters, and S Zaefferer. Three-dimensional investigation of the texture and microstructure below a nanoindent in a cu single crystal using 3d ebsd and crystal plasticity finite element simulations. *Acta Materialia*, 54(7):1863–1876, 2006.

[38] EH Lee. Elastic-plastic deformation at finite strains. *Journal of Applied Mechanics*, 36(1):1–6, 1969.

[39] H Mecking and UF Kocks. Kinetics of flow and strain-hardening. *Acta Metallurgica*, 29(11):1865–1875, 1981.

[40] A Arsenlis, DM Parks, R Becker, and VV Bulatov. On the evolution of crystallographic dislocation density in non-homogeneously deforming crystals. *Journal of the Mechanics and Physics of Solids*, 52(6):1213–1246, 2004.

[41] Y Estrin. Dislocation-density-related constitutive modeling. *Unified constitutive laws of plastic deformation*, 1:69–106, 1996.

[42] UF Kocks and H Mecking. Physics and phenomenology of strain hardening: the fcc case. *Progress in materials science*, 48(3):171–273, 2003.

[43] PS Follansbee and UF Kocks. A constitutive description of the deformation of copper based on the use of the mechanical threshold stress as an internal state variable. *Acta Metallurgica*, 36(1):81–93, 1988.

[44] PC Paris and F Erdogan. A critical analysis of crack propagation laws. *Journal of basic engineering*, 85(4):528–533, 1963.

[45] AJ McEvily and RG Boettner. On fatigue crack propagation in fcc metals. *Acta Metallurgica*, 11(7):725–743, 1963.

[46] Elber Wolf. Fatigue crack closure under cyclic tension. *Engineering Fracture Mechanics*, 2(1):37–45, 1970.

[47] AJ McEvily. On crack closure in fatigue crack growth. In *Mechanics of Fatigue Crack Closure*. ASTM International, 1988.

[48] K Gall, H Sehitoglu, and Y Kadioglu. Plastic zones and fatigue-crack closure under plane-strain double slip. *Metallurgical and materials transactions A*, 27(11):3491–3502, 1996.

[49] JD Dougherty, J Padovan, and TS Srivatsan. Fatigue crack propagation and closure behavior of modified 1070 steel: finite element study. *Engineering Fracture Mechanics*, 56(2):189–212, 1997.

[50] K Solanki, SR Daniewicz, and JC Newman. Finite element analysis of plasticity-induced fatigue crack closure: an overview. *Engineering Fracture Mechanics*, 71(2):149–171, 2004.

[51] RC McClung and H Sehitoglu. On the finite element analysis of fatigue crack closure: 1. basic modeling issues. *Engineering Fracture Mechanics*, 33(2):237–252, 1989.

[52] RC McClung and H Sehitoglu. On the finite element analysis of fatigue crack closure: 2. numerical results. *Engineering Fracture Mechanics*, 33(2):253–272, 1989.

[53] RC McClung and DL Davidson. Near-tip and remote characterization of plasticity-induced fatigue crack closure. In *Advances in Fatigue Crack Closure Measurement and Analysis: Second Volume*. ASTM International, 1999.

[54] JC Newman. A finite-element analysis of fatigue crack closure. In *Mechanics of Crack Growth*. ASTM International, 1976.

[55] JD Skinner and SR Daniewicz. Simulation of plasticity-induced fatigue crack closure in part-through cracked geometries using finite element analysis. *Engineering Fracture Mechanics*, 69(1):1–11, 2002.

[56] T Nicholas, AN Palazotto, and E Bednarz. An analytical investigation of plasticity induced closure involving short cracks. In *Mechanics of Fatigue Crack Closure*. ASTM International, 1988.

[57] K Ogura, K Ohji, and K Honda. Influence of mechanical factors on fatigue crack closure. In *ICF4, Waterloo (Canada) 1977*, 2013.

[58] PL Lalor and H Sehitoglu. Fatigue crack closure outside a small-scale yielding regime. In *Mechanics of Fatigue Crack Closure*. ASTM International, 1988.

[59] S Roychowdhury and RH Dodds. A numerical investigation of 3-d small-scale yielding fatigue crack growth. *Engineering Fracture Mechanics*, 70(17):2363–2383, 2003.

[60] GP Potirniche, SR Daniewicz, and JC Newman. Simulating small crack growth behaviour using crystal plasticity theory and finite element analysis. *Fatigue & Fracture of Engineering Materials & Structures*, 27(1):59–71, 2004.

[61] H Proudhon, J Li, F Wang, A Roos, V Chiaruttini, and S Forest. 3d simulation of short fatigue crack propagation by finite element crystal plasticity and remeshing. *International Journal of Fatigue*, 82:238–246, 2016.

[62] RG Chermahini and AF Blom. Variation of crack-opening stresses in three-dimensions: finite thickness plate. *Theoretical and applied fracture mechanics*, 15(3):267–276, 1991.

[63] AG Carlyle and RH Dodds. Three-dimensional effects on fatigue crack closure under fully-reversed loading. *Engineering fracture mechanics*, 74(3):457–466, 2007.

[64] JC Sobotka and RH Dodds. Steady crack growth in a thin, ductile plate under small-scale yielding conditions: Three-dimensional modeling. *Engineering Fracture Mechanics*, 78(2):343–363, 2011.

[65] DL McDowell and FPE Dunne. Microstructure-sensitive computational modeling of fatigue crack formation. *International journal of fatigue*, 32(9):1521–1542, 2010.

[66] R Hill. Generalized constitutive relations for incremental deformation of metal crystals by multislip. *Journal of the Mechanics and Physics of Solids*, 14(2):95–102, 1966.

[67] R Hill and JR Rice. Constitutive analysis of elastic-plastic crystals at arbitrary strain. *Journal of the Mechanics and Physics of Solids*, 20(6):401–413, 1972.

[68] A Needleman, RJ Asaro, J Lemonds, and D Peirce. Finite element analysis of crystalline solids. *Computer Methods in Applied Mechanics and Engineering*, 52(1-3):689–708, 1985.

[69] JR Rice. Inelastic constitutive relations for solids: an internal-variable theory and its application to metal plasticity. *Journal of the Mechanics and Physics of Solids*, 19(6):433–455, 1971.

[70] JR Rice, DE Hawk, and RJ Asaro. Crack tip fields in ductile crystals. In *Non-Linear Fracture*, pages 301–321. Springer, 1990.

[71] S Flouriot, S Forest, G Cailletaud, A Köster, L Rémy, B Burgardt, V Gros, S Mosset, and J Delautre. Strain localization at the crack tip in single crystal ct specimens under monotonous loading: 3d finite element analyses and application to nickel-base superalloys. *International journal of fracture*, 124(1-2):43–77, 2003.

[72] GP Potirniche and SR Daniewicz. Analysis of crack tip plasticity for microstructurally small cracks using crystal plasticity theory. *Engineering Fracture Mechanics*, 70(13):1623–1643, 2003.

[73] K Gall, H Sehitoglu, and Y Kadioglu. Fem study of fatigue crack closure under double slip. *Acta materialia*, 44(10):3955–3965, 1996.

[74] JL Bouvard, JL Chaboche, F Feyel, and F Gallerneau. A cohesive zone model for fatigue and creep–fatigue crack growth in single crystal superalloys. *International Journal of Fatigue*, 31(5):868–879, 2009.

[75] RJ Asaro. Crystal plasticity. *Journal of applied mechanics*, 50(4b):921–934, 1983.

[76] AF Bower. *Applied mechanics of solids*. CRC press, 2009.

[77] AE Green and PM Naghdi. A general theory of an elastic-plastic continuum. *Archive for rational mechanics and analysis*, 18(4):251–281, 1965.

[78] S Kok, AJ Beaudoin, and DA Tortorelli. A polycrystal plasticity model based on the mechanical threshold. *International Journal of Plasticity*, 18(5):715–741, 2002.

[79] B Banerjee. The mechanical threshold stress model for various tempers of aisi 4340 steel. *International Journal of Solids and Structures*, 44(3):834–859, 2007.

[80] GT Gray III, SR Chen, and KS Vecchio. Influence of grain size on the constitutive response and substructure evolution of monel 400. *Metallurgical and Materials Transactions A*, 30(5):1235–1247, 1999.

[81] PS Follansbee. Fundamentals of strength, 2014.

[82] DM Goto, RK Garrett Jr, JF Bingert, S-R Chen, and GT Gray III. The mechanical threshold stress constitutive-strength model description of hy-100 steel. *Metallurgical and Materials Transactions A*, 31(8):1985–1996, 2000.

[83] N Tsuchida, Y Tomota, H Moriya, O Umezawa, and K Nagai. Application of the kocks–mecking model to tensile deformation of an austenitic 25cr–19ni steel. *Acta materialia*, 49(15):3029–3038, 2001.

[84] UF Kocks. As argon and mf ashby. *Thermodynamics and kinetics of slip. Ist*, 1975.

[85] W Yang and WB Lee. *Mesoplasticity and its Applications*. Springer Science & Business Media, 2013.

[86] HJ Frost and MF Ashby. Deformation mechanism maps: the plasticity and creep of metals and ceramics. 1982.

[87] E Nes. Modelling of work hardening and stress saturation in fcc metals. *Progress in Materials Science*, 41(3):129–193, 1997.

[88] JE Bailey. The dislocation density, flow stress and stored energy in deformed polycrystalline copper. *Philosophical magazine*, 8(86):223–236, 1963.

[89] A Acharya, JL Bassani, and A Beaudoin. Geometrically necessary dislocations, hardening, and a simple gradient theory of crystal plasticity. *Scripta Materialia*, 48(2):167–172, 2003.

[90] A Acharya and JL Bassani. Lattice incompatibility and a gradient theory of crystal plasticity. *Journal of the Mechanics and Physics of Solids*, 48(8):1565–1595, 2000.

[91] JF Nye. Some geometrical relations in dislocated crystals. *Acta metallurgica*, 1(2):153–162, 1953.

[92] S Kok, AJ Beaudoin, and DA Tortorelli. On the development of stage iv hardening using a model based on the mechanical threshold. *Acta Materialia*, 50(7):1653–1667, 2002.

[93] PG Luccarelli, GJ Pataky, H Sehitoglu, and S Foletti. Finite element simulation of single crystal and polycrystalline haynes 230 specimens. *International Journal of Solids and Structures*, IJSS-D-16-00834, Under Review.

[94] RA Brown. Theory of transport processes in single crystal growth from the melt. *AIChE Journal*, 34(6):881–911, 1988.

[95] P Reu. Virtual strain gage size study. *Experimental Techniques*, 39(5):1–3, 2015.

[96] MP Groover. *Fundamentals of modern manufacturing: materials processes, and systems*. John Wiley & Sons, 2007.

[97] K Gall, H Sehitoglu, YI Chumlyakov, IV Kireeva, and HJ Maier. The influence of aging on critical transformation stress levels and martensite start temperatures in niti: part i - aged microstructure and micro-mechanical modeling. *Journal of engineering materials and technology*, 121(1):19–27, 1999.

[98] K Gall, H Sehitoglu, YI Chumlyakov, IV Kireeva, and HJ Maier. The influence of aging on critical transformation stress levels and martensite start temperatures in niti: part ii - discussion of experimental results. *Journal of engineering materials and technology*, 121(1):28–37, 1999.

[99] V Randle and O Engler. *Introduction to texture analysis: macrotexture, microtexture and orientation mapping*. CRC press, 2000.

[100] WZ Abuzaid, MD Sangid, JD Carroll, H Sehitoglu, and J Lambros. Slip transfer and plastic strain accumulation across grain boundaries in hastelloy x. *Journal of the Mechanics and Physics of Solids*, 60(6):1201–1220, 2012.

[101] E Schmid and W Boas. Plasticity of crystals. 1950.

[102] MD Sangid, HJ Maier, and H Sehitoglu. The role of grain boundaries on fatigue crack initiation–an energy approach. *International Journal of Plasticity*, 27(5):801–821, 2011.

[103] PJ Armstrong and CO Frederick. *A mathematical representation of the multiaxial Bauschinger effect*. Central Electricity Generating Board [and] Berkeley Nuclear Laboratories, Research & Development Department, 1966.

[104] G Kang. Ratchetting: recent progresses in phenomenon observation, constitutive modeling and application. *International Journal of Fatigue*, 30(8):1448–1472, 2008.

[105] S Sinha and S Ghosh. Modeling cyclic ratcheting based fatigue life of hsla steels using crystal plasticity fem simulations and experiments. *International journal of fatigue*, 28(12):1690–1704, 2006.

[106] R Dingreville, CC Battaile, LN Brewer, EA Holm, and BL Boyce. The effect of microstructural representation on simulations of microplastic ratcheting. *International Journal of Plasticity*, 26(5):617–633, 2010.

[107] S Rabbolini, PG Luccarelli, S Beretta, S Foletti, and H Sehitoglu. Near-tip closure and cyclic plasticity in ni-based single crystals. *International Journal of Fatigue*, 89:53–65, 2016.

[108] RA Smith and KJ Miller. Fatigue cracks at notches. *International Journal of Mechanical Sciences*, 19(1):11–22, 1977.

[109] S Pommier and PH Bompard. Bauschinger effect of alloys and plasticity-induced crack closure: a finite element analysis. *Fatigue and Fracture of Engineering Materials and Structures*, 23(2):129–140, 2000.

[110] S Pommier. Plane strain crack closure and cyclic hardening. *Engineering Fracture Mechanics*, 69(1):25–44, 2002.

[111] H Tada, PC Paris, and GR Irwin. The analysis of cracks handbook. *New York: ASME Press*, 2:1, 2000.

[112] Hibbett, Karlsson, and Sorensen. *ABAQUS/standard: User's Manual*, volume 1. Hibbitt, Karlsson & Sorensen, 1998.

[113] A Zeghadi, S Forest, A-F Gourgues, and O Bouaziz. Ensemble averaging stress–strain fields in polycrystalline aggregates with a constrained surface microstructure–part 2: Crystal plasticity. *Philosophical Magazine*, 87(8-9):1425–1446, 2007.